Lightwave-driven scanning tunneling microscopy and spectroscopy: atomic motion meets electronic dynamics

Dissertation
zur Erlangung des Doktorgrades der Naturwissenschaften
(Dr. rer. nat.)
der Fakultät für Physik der Universität Regensburg

vorgelegt von
Carmen Roelcke
aus Regensburg
im Jahr 2024

Das Promotionsgesuch wurde eingereicht am: 03.07.2024

Die Arbeit wurde angeleitet von: Prof. Dr. Rupert Huber & Prof. Dr. Jascha Repp

Prüfungsausschuss:	Vorsitzender:	Prof. Dr. Jaroslav Fabian
	1. Gutachter:	Prof. Dr. Rupert Huber
	2. Gutachter:	Prof. Dr. Jascha Repp
	weiterer Prüfer:	Prof. Dr. Jörg Wunderlich

Und alles zusammen, alle Stimmen, alle Ziele, alles Sehnen, alle Leiden, alle Lust,
alles Gute und Böse, alles zusammen war die Welt.
Alles zusammen war der Fluss des Geschehens, war die Musik des Lebens.
— Siddhartha, Hermann Hesse [Hes16]

Contents

Chapter 1

Introduction

“If the whole is ever to gladden thee, that whole in the smallest thing thou must see” [Goe98]. With these verses as a part of the poem ”Gott, Gemüt und Welt”, Johann Wolfgang von Goethe mused that to understand our world, the key is the observation of its elementary building blocks. Following the incentive to understand the world in its very precious details, numerous scientists have been working on methods, which make the nanocosmos accessible to the human eye.

This progress is driven by numerous questions. What do chemical reactions look like? In which way do nuclei and electrons “move” or “react”? And can we change these properties or influence the motion of particles on small scales? Besides satisfying our curiosity, insights into the nanocosmos could feed applied research advancing technology: to establish more efficient catalysts – or qubits with long coherence times as a sensible basis for quantum computing. There is an enormous variety of phenomena in the nanoworld to be discovered. It ranges from electron to lattice dynamics and from single quanta to many-particle systems. Their precise interplay and competition is particularly interesting.

The motion of minute entities intrinsically takes place on very short time scales. For instance, molecular motion on an atomic level – such as isomerization [Sch91] or single-molecule adsorption dynamics [Coc16, Pel20] – takes place on picosecond time scales and faster. Also bound electron-hole pairs in transition metal dichalcogenides with a spatial extension on the nanometer scale are known to decay on these time scales [Poe15, Mer19]. To probe such phenomena simultaneously in space and time, i.e., to record a movie, the techniques applied need to exhibit a high spatial and at the same time a high temporal precision. Even more, processes such as chemical reactions, catalysis and dephasing of qubits can be governed by atomically confined energy levels and reversely, structural motion can shift energy levels. This is why additional energy resolution is highly desired to paint a more comprehensive picture of the nanocosmos. In essence, we are requesting a technique ideally with atom-scale spatial, ultrafast temporal (smaller than one picosecond, $1\text{ ps} = 10^{-12}\text{ s}$) and millielectronvolt (meV) energy resolution.

Simultaneously meeting these requirements in a single technique has proven extremely challenging. Several techniques combine two of the three demands allowing for the exemplary seminal experiments mentioned in the following.
Time-resolved angle-resolved photoemission spectroscopy and momentum microscopy feature superior time and energy resolution, enough to monitor the formation and evolution of Floquet bands [Ito23], to measure the occupation of select molecular orbitals [Wal21a] and to resolve phonon-induced changes in the band structure [Bal23]. However, even in momentum microscopy, one averages over larger areas of periodically structured samples, obscuring details in real space.
The demanded spatial and energy resolution have been achieved by confinement of light [Lee19] to atomically sharp metallic tips, which has enabled mapping of molecular levels and vibrational states by combining scanning tunneling microscopy (STM) with photoluminescence [Yan20] or Raman scattering [Xu21], but no ultrafast time resolution has been demonstrated so far.
Importantly, ultrafast temporal and atom-scale spatial precision are required to be able to take videos of the nanoworld. To fulfill these two requirements, the most prolific approach is the combination of ultrafast techniques with high-resolution microscopy such as atomic force microscopy [Jah15], electron transmission microscopy [Gri06, Fei17] or scanning tunneling microscopy (STM) [Coc13, Coc16, Dhi17, Lei23, Bor23]. Only lately, the field of ultrafast microscopy has started to access the realm of atom-scale femtosecond dynamics enabling single-molecule movies directly in space via lightwave-driven scanning tunneling microscopy (LW-STM) [Coc16, Pel20]. LW-STM combines the sub-ångström ($1\text{ Å} = 10^{-10}\text{ m}$) spatial resolution of STM with a temporal precision of about 100 femtoseconds ($1\text{ fs} = 10^{-15}\text{ s}$). The latter is

set by free-space sub-cycle terahertz (1 THz = 10^{12} Hz) pulses coupled to the STM tip [Coc16, Pel20].
Energy resolution is intrinsic to conventional STM that images the local density of states – the convolution of the sample density of states with the local overlap of tip and sample wavefunctions (chapter 2). However, the temporal evolution of the local density of states has never been demonstrated, whereas highly desired [LH21, Amm22].

In this work, I will introduce how we combine the requirements of atomic spatial, ultrafast temporal and millielectron energy resolution in a single setup. First, I give an overview of scanning tunneling microscopy and spectroscopy (chapter 2) for a better understanding of LW-STM. In chapter 3, the technical cornerstones used within this thesis to implement control over structural and electronic dynamics are summarized. Based on these techniques, I will introduce a novel mechanism to control molecular structural dynamics on atomic length scales in the most direct way, namely by applying ultrafast atom-scale forces (chapter 4). Moreover, I will present the first-ever quantitative measurement of atom-scale near-field waveforms (chapter 5), allowing us to perform experiments calibrated in units of electron volts. Finally, I will demonstrate the novel technique of time-resolved lightwave-driven scanning tunneling spectroscopy (LW-STS) to map out electronic dynamics by watching the temporal evolution of the local density of states in a defected transition metal dichalcogenide monolayer with 10 meV-scale energy resolution (chapter 6). Thereby, we open the door to the uncharted and emphatically proposed [Amm22, Lei23] realm of spectral evolution of spatially confined energy levels with simultaneous ultrafast temporal and atom-scale spatial precision. This recent milestone establishes a new field of research of spectroscopy on atomic length scales – directly in real space. To further explore the realm of the nanocosmos governed by quantum rules, I will finally give an outlook on experiments, which access yet another degree of freedom, namely the electronic spin (chapter 7). For this purpose, a magnetic field has been included in an ultrafast STM based on intense instrumentation development. The experiments demonstrated throughout this thesis show that LW-STM together with LW-STS solves a number of challenges of modern nanoscience and paves the way for a thorough understanding of processes like transiently driven phase transitions, high-temperature superconductors and other exotic states of matter on microscopic length scales.

Chapter 2

Scanning tunneling microscopy and spectroscopy

This chapter reports on the work of other scientists founding the field of scanning tunneling microscopy and its theoretical description. In large parts, the text recapitulates discussions in [Che07].

Nowadays, the nanocosmos can be directly imaged with highest-resolution scanning probe, super-resolution optical and electron microscopes. The impact of these techniques has been honored with the Nobel Prizes in physics 1986 (E. Ruska: electron microscope, G. Binnig and H. Rohrer: STM) as well as in chemistry 2014 (E. Betzig, S. W.Hell and W.E. Moerner: superresolution microscopy techniques) and 2017 (J. Dubochet, J. Frank and R. Henderson: development of cryo-electron microscopy).

Whereas conventional optical microscopes are generally limited in their spatial resolution by diffraction, the mentioned microscopes enable the observation of minuscule objects like single molecules and even individual atoms. In particular, STM is able to resolve changes of the electronic structure of a specific sample on atomic length scales. Its invention [Bin82, Bin83] has revolutionized many fields of research. Once considered a dream (e.g. Feynman's famous speech "There's plenty of room at the bottom"), nowadays, we can routinely map out the electronic structure of individual molecules in space via STM and additionally in energy using

scanning tunneling spectroscopy (STS) [Rep05b]. One of Feynman's related visions was to rearrange single atoms deliberately one-by-one directly in space, which can be achieved via atomic manipulation in STM.
STM and STS will be summarized in this chapter.

Working principle of STM. The STM was invented by Gerd Binnig and coworkers [Bin82, Bin83]. Fundamentally, it consists of an atomically sharp metal tip, which is scanned across a conductive sample (Fig. 2.1a,b). STM is based on the quantum mechanical effect of tunneling electrons through a potential barrier between the two electrodes. When the tip is brought close enough to the sample (typical distance of a few ångströms), their electronic wavefunctions overlap. In this scenario, the quantum mechanical probability of electrons to tunnel through a potential barrier is non-zero. In order to understand the basic principle behind the tunneling processes, it is sufficient to treat a one-dimensional STM-like system. For a one-dimensional cut along the apex of the tip perpendicular to the surface, the tunneling barrier can be approximated by the schematic shown in Fig. 2.1c. Both sample and tip can be modeled as a free electron gas with potentially different work functions Φ_s and Φ_t. For simplicity, we assume $\Phi = \Phi_\mathrm{s} = \Phi_\mathrm{t}$. In general, electrons can tunnel from occupied to unoccupied states. Their transmission probability exponentially depends on the height of the potential barrier and the distance between the two electrodes. For a bias voltage $V \neq 0$ between sample and tip, the potential landscape of the tunnel junction is tilted (Fig. 2.1c). In this situation, an imbalanced transmission of tunneling electrons from tip to sample and vice versa occurs such that a current can be detected (Fig. 2.1d), which is sensitive to the geometry and energy levels of electronic states down to the atomic scale.
By scanning the tip across the sample and measuring the tunneling current, the electronic structure of a sample can be mapped in space with atomic resolution. For a better understanding, we recapitulate the nature of the tunneling current in an STM junction and its contributions.

Tunneling current. When the two electrodes are far apart, the tip-sample system can be described as two separate systems, the one of the tip, and the one of the sample. In this situation, the wavefunctions of sample ψ and tip χ satisfy the

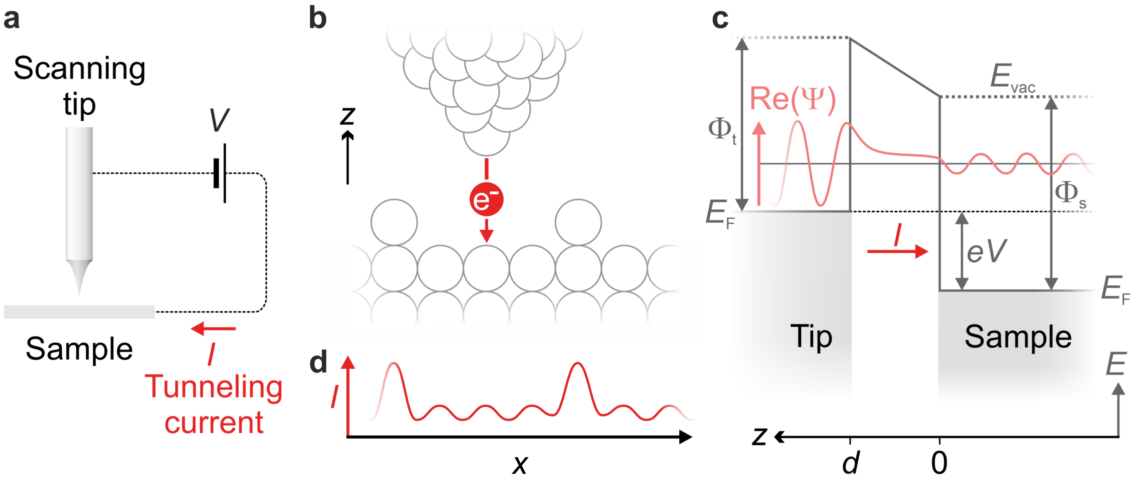

Figure 2.1 | Scanning tunneling microscopy. **a**, A metallic tip is scanned across a conductive sample. When a voltage (V) is applied between tip and sample, a current (I) can be detected, which is caused by electrons tunneling from tip to sample or vice versa across the atomic-scale junction (**b**, atoms: circles). **c**, A schematic energy landscape along a cut in z-direction through the tunnel junction reveals the vacuum barrier between tip apex atom and sample. The vacuum barrier is dominated by the work functions Φ_{t}, Φ_{s} and the shift of the Fermi level E_{F} by eV, where e is the elementary charge, due to an applied voltage. In the following, we will assume $\Phi = \Phi_{\mathrm{t}} = \Phi_{\mathrm{s}}$. The wavefunction ($\Psi$) amplitude of an electron in the tip decays into the vacuum barrier. The amplitude drop from one electrode to the other depends on the distance between tip and sample. At a non-zero voltage, electrons can tunnel from occupied to unoccupied states causing a measurable current. **d**, Depending on the distance of atomic features between tip and sample, the transmission probability of the electron and hence the tunneling current, I, differ.

respective Schrödinger equation. Inside the tunnel junction, the wavefunctions of both electrodes decay exponentially into the vacuum with a decay constant κ. When brought together, the individual Schrödinger equations need to be merged to describe the combined system. In principle, the tip and sample wavefunctions are eigenfunctions of the different Hamiltonians. In Bardeen's tunneling theory [Bar61] published even before STM was invented, the influence of the tip system on the sample's wavefunction and vice versa is assumed to be negligible. This is very well fulfilled as long as the tunneling coupling is weak. Then, the total tunneling current between tip and sample with an applied bias V can be deduced to be

$$I(V) = \frac{4\pi e}{\hbar} \int_{-\infty}^{\infty} [f(E_F - eV + \epsilon) - f(E_F + \epsilon)] \times \rho_{\mathrm{t}}(E_F - eV + \epsilon)\rho_{\mathrm{s}}(E_F + \epsilon)|M(\epsilon)|^2 \mathrm{d}\epsilon \tag{2.1}$$

where $f(E) = (1 + \exp[(E - E_F)/k_B T])^{-1}$ is the Fermi distribution function and ρ_{t} and ρ_{s} describe the density of states (DOS) of tip and sample, respectively. Here, k_B represents the Boltzman constant and T is the temperature. In general, $k_B T$ leads to a finite energy resolution in STM measurements. At low temperatures, the Fermi distribution function can be approximated by a step function. Thereby, the expression describing the tunneling current (equation 2.1) simplifies to

$$I(V) = \frac{4\pi e}{\hbar} \int_{0}^{eV} \rho_{\mathrm{t}}(E_F - eV + \epsilon)\rho_{\mathrm{s}}(E_F + \epsilon)|M(\epsilon)|^2 \mathrm{d}\epsilon \ . \tag{2.2}$$

The tunnel matrix element M describes the transition rate from one wavefunction to the other. In the gap region ($0 < z_0 < d$), M can be written as a surface integral of the wavefunctions of the tip and the sample on a separation surface Σ, which is located somewhere between the electrodes inside the barrier [Bar61, Che07]:

$$\begin{aligned} M &= \frac{\hbar^2}{2m} \int_{\Sigma} (\psi \nabla \chi^* - \chi^* \nabla \psi) \cdot \mathrm{d}\mathbf{S} \\ &= \frac{\hbar^2}{2m} \int_{z=z_0} \left[\psi \frac{\partial \chi^*}{\partial z} - \chi^* \frac{\partial \psi}{\partial z} \right] \mathrm{d}x \mathrm{d}y \ . \end{aligned} \tag{2.3}$$

To understand the dependence of M on the tip-sample distance, we can describe an effective one-dimensional system, which is homogeneous in x and y direction with the tunnel barrier in z direction. Then, the wavefunctions in the gap region can be written as $\psi(x,y,z) = \psi(x,y,0)\cdot\exp(-\kappa z)$ and $\chi(x,y,z) = \chi(x,y,d)\cdot\exp(-\kappa(d-z))$. The energy-dependent decay constant of the wavefunctions in the case of elastic tunneling and identical work functions Φ for sample and tip is $\kappa = \frac{\sqrt{2m(\Phi-\epsilon)}}{\hbar}$ [Che07]. m describes the electron mass. In the quasi one-dimensional scenario, the tunnel matrix elements reads as

$$M = \frac{\hbar^2}{2m}\int_{z=z_0} 2\kappa\cdot\psi(x,y,0)\chi^*(x,y,d)\ \mathrm{d}x\mathrm{d}y\cdot\exp(-\kappa d)\ \text{[Che07]}. \tag{2.4}$$

Three components determine M: the energy of the tunneling electron ϵ, the tip-sample distance d and the spatial structure of tip and sample wavefunctions. In the following, we will treat their impact, individually.

Distance dependence. As a consequence of equations 2.2 and 2.4, the tunneling current through the tunnel junction drops exponentially with tip-sample distance since $I \propto |M|^2 \propto \exp(-2\kappa d)$. When scanning the tip across local protrusions of the sample (Fig. 2.1d) while keeping the tip at a fixed height (constant-height measurement), the smaller tip-sample distance leads to a higher absolute current. For typical work functions of about $\Phi \approx 5$ eV ([Che07], chapter 1.2.1) and $eV \ll \Phi$, κ amounts to $\sim$1.14 Å^{-1} such that the tunneling current drops by an order of magnitude when d increases by 1 Å. Hence, by mapping the tunneling current as a function of the tip position, atomic protrusions in the sample can be detected.
Instead of keeping the tip height fixed and measuring the change in tunneling current, one can utilize a feedback loop, which adjusts the tip height d to keep the tunneling current constant (Fig. 2.2). In this mode of operation (constant-current measurements), calibrated piezo actuators steer the tip height. The change in d is read out, which is linked to the topography of the sample. Irrespective of the exact operation mode, the detected tunneling current or apparent topography depends on the local tip-sample distance.

Wavefunction overlap and density of states. As mentioned, M does not only depend on the tip-sample distance, but it is also determined by the electron energy and the spatial structure of tip and sample wavefunctions.

Figure 2.2 | Constant-current STM. The tip height d (black line) is adapted such that the tunneling current (red line) stays constant. Thereby, the tip follows a trajectory closely linked to the topography of the electronic surface structure.

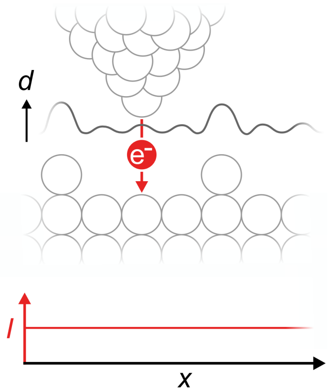

Only when the wavefunctions of tip and sample overlap at a specific position of the tip, the tunneling matrix is non-zero such that electrons can tunnel (equations 2.3 and 2.4). At certain positions in space, the electronic features of the substrate are protruding less or more prominently into the vacuum such that the overlap of the wavefunction of the tip apex and the electronic wavefunction of the scanned surface differs at varying positions of the tip (Fig. 2.3a). Hence, M changes and therefore also the tunneling current.

The fact that the spatial map of the tunneling current is governed by a convolution of the tip electronic states and the sample electronic states is an essential finding. Yet, the interpretation of an image gathered by scanning across a surface is not straightforward for an unknown tip wavefunction. In contrast, if the tip is assumed to be a geometrical point, the STM image is shaped by properties of the sample alone. This approximation, the Tersoff-Hamann model [Ter83, Ter85, Han87], can be modeled by a spherically symmetric tip wavefunction. In general, the tip wavefunction can be expanded into the spherical-harmonic components [Che07]. The part of the tunnel matrix element, which is induced by the spherically symmetric s-wave contribution reads as $M_s = A\psi(\vec{r_0})$ with a constant A, where $\vec{r_0}$ is the center of the tip apex atom [Ter83, Ter85, Han87]. This implies that for s-wave-like tips the tunneling current is proportional to the square of the sample wavefunction $|\psi(\vec{r_0})|^2$. Hence, whenever the s-state component dominates the overall tip wavefunction, a scan of the sample leads to a spatially resolved image where the contrast is purely governed by the electronic structure of the sample surface - with a single atom at the apex, even atomic resolution is possible. The s-wave approximation is valid for plain metal tips [Che07].

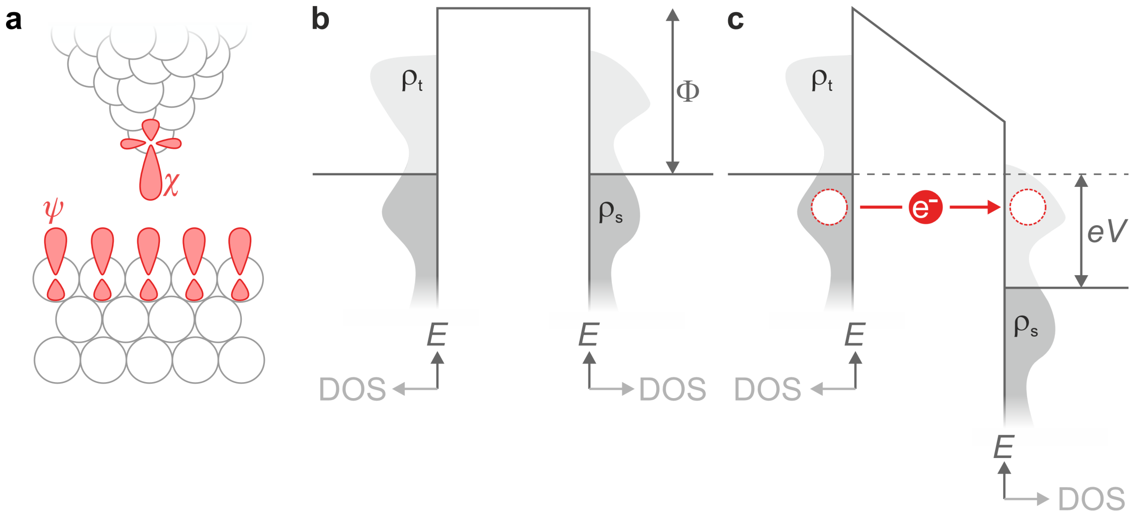

Figure 2.3 | Spatial and energy overlap of occupied and unoccupied states. **a**, For different tip positions, the overlap of tip (χ) and sample (ψ) wavefunctions varies. Electrons can only tunnel from one electrode to the other, when the wavefunctions overlap. As a result, the spatial structure of the wavefunctions determines the tunneling current. Moreover, the fermionic electrons can tunnel only from occupied to unoccupied states. In both sample and tip, the electronic states are filled up to the respective Fermi level. **b**, Schematic energy landscape at zero bias voltage: all states in tip and sample are occupied up to the same energy for equal work functions Φ of tip and sample. **c**, At non-zero bias voltage, electrons can tunnel from occupied states in the tip to unoccupied states in the sample or vice versa for a flipped polarity of the bias voltage. Depending on the tip position, tunneling between different states is possible. The number of occupied and unoccupied states in specific energy intervals in tip and sample is described by the DOS ρ_t and ρ_s.

Apart from the spatial dependence of the tunneling current, the applied bias voltage shapes the composition of the STM image due to the fact that the measured current and thus image contrast is created by electrons tunneling from occupied to unoccupied states at a specific energy (Fig. 2.3b,c). Hence, the tunneling current is determined by the number of occupied and unoccupied states in the energy interval from zero voltage to the applied bias voltage eV: the larger the DOS of occupied states on one electrode and the larger the DOS of unoccupied states on the other electrode at the same energies, the higher the tunneling current (equation 2.2).

In summary, we can understand STM in the following simplified manner: exploiting the quantum mechanical tunneling phenomenon and using an atomically sharp tip as a probe, one can measure a distance-dependent tunneling current which is determined by the DOS of the two electrodes and the bias voltage applied between tip and sample. Scanning across the surface, it is possible to map the electronic structure of a sample with atomic resolution.

Scanning tunneling microscopy of individual molecular orbitals. With a suitable sample design, one can even resolve the electronic structure of individual conjugated molecules in real space using STM. To this end, molecules are deposited onto a suitable substrate. Since the detection signal in STM is an electronic current, a conductive substrate is necessary to measure tunneling through the barrier. Hence, to map individual molecules, they can be deposited onto a metallic substrate like copper or gold crystals. In the study of single molecules, scientists are often interested in the unperturbed electronic structure in vacuum. When molecules adsorb on metal, however, their electronic structure is strongly perturbed by the interaction with substrate electrons. In order to study the unperturbed molecular orbital, one can decouple the molecular orbitals from the electronic structure of the metal substrate by depositing an insulating salt layer onto the metal surface as described in [Rep05b]. Such a salt layer needs to be thin enough for electrons to tunnel through. Here, a trade-off must be made: a thicker layer would allow for more efficient decoupling, but reduces the tunneling probability from the molecule to the substrate and thus the measured tunneling current. Usually, a few atomic layers of NaCl are deposited for single-molecule measurements in STM. In Fig. 2.4a, an exemplary sample with a

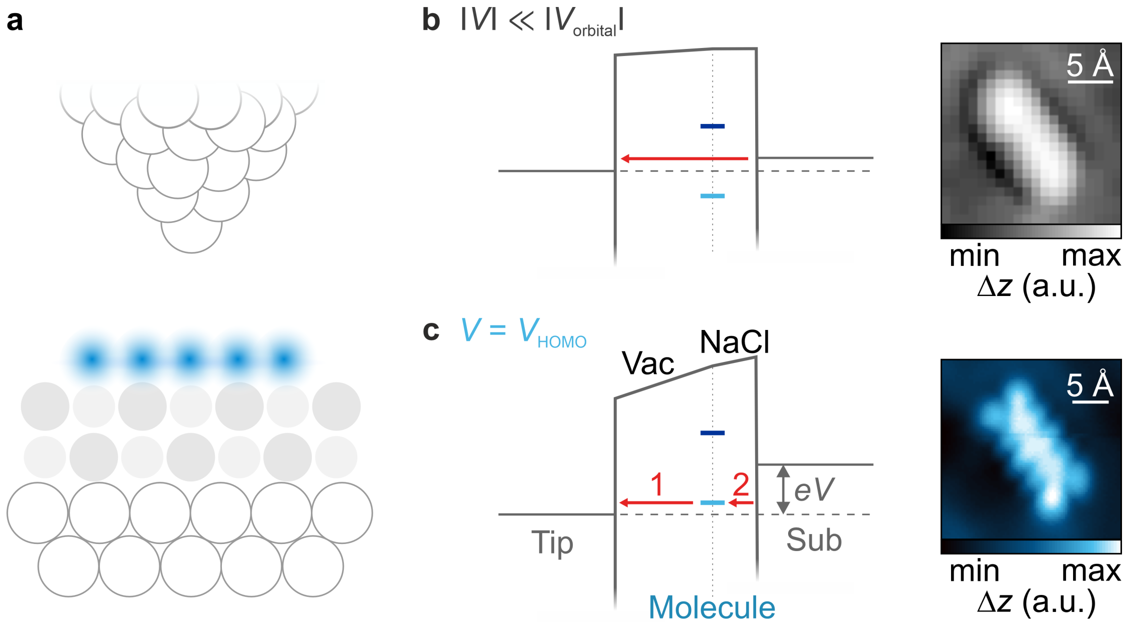

Figure 2.4 | Scanning tunneling microscopy of a single molecule. **a**, Schematic setup from bottom to top: metal substrate, salt layer, molecule, vacuum, tip. The metal tip and the metallic substrate (hollow grey circles) form the two electrodes of the STM junction. An individual molecule (blue) is decoupled electronically from the metallic substrate by a salt layer, here NaCl (filled circles), to hinder hybridization of the substrate electronic states and the molecular orbitals. **b**, Co-tunneling. When the bias voltage is too small to open a tunneling channel through a molecular orbital, electrons tunnel directly from the substrate to the tip (left). In an STM image, the molecule (here: pentacene) appears as a featureless rod (right panel). **c**, Resonant tunneling. When eV exceeds the energy difference between $E_\mathrm{F} - E_\mathrm{orbital}$, electrons can tunnel sequentially through the molecular level. Here, an electron tunnels from the highest occupied molecular level (HOMO) into the tip (1). In a second step, the HOMO is refilled with an electron from the metallic substrate (2). By scanning the tip across the molecule, the HOMO can be imaged in real space (right panel).

bilayer sodium chloride (NaCl) and an individual pentacene molecule is sketched. In a schematic potential landscape of the tunnel junction, the molecular frontier orbitals, the highest occupied (HOMO) and the lowest unoccupied (LUMO) molecular orbital, can be visualized as discrete energy levels (Fig. 2.4b,c, energy schemes). To map these orbitals in space, we need to understand the different tunneling paths for varying voltages. When no bias voltage is applied between tip and substrate, electrons cannot tunnel from the tip into the molecular orbital and from there into the surface or vice versa. When a voltage $V \neq 0$ is applied between substrate and tip, the Fermi edges of tip and substrate differ by eV. A part of the voltage drops in the salt layer and the other part in the vacuum gap between molecule and tip. For any bias voltage, direct tunneling from the substrate to the tip or vice versa is possible (Fig. 2.4b, left panel) since the metallic tip and substrate have a continuous DOS. Here, electrons tunnel through the combined thick tunnel barrier. This direct tunnel process is called "in-gap", "non-resonant" tunneling or "co-tunneling". For small bias voltages with $|eV| < |E_{\mathrm{orbital}} - E_{\mathrm{F}}|$, only co-tunneling can take place such that an STM scan images the substrate and the molecule appears as an additional protrusion since it modifies the tunnel barrier (Fig. 2.4b, right panel). When eV exceeds the energy difference between a molecular level and the tip or sample Fermi energy (Fig. 2.4c, left panel), additionally, tunneling through a molecular orbital can take place. For instance, when the tip Fermi level falls below the HOMO energy, an electron can tunnel from the occupied molecular orbital into the tip in a first step. In a second step, the molecular orbital is refilled with an electron from the substrate causing a net tunneling current from the substrate to the tip. In case of the LUMO, an electron can sequentially tunnel from an occupied state in the tip into the selected molecular orbital and then from the molecular orbital into the metal substrate. This two-step tunneling process is referred to as "sequential tunneling". Since the tunneling distance between tip/substrate and molecule is much smaller than the distance between tip and substrate, sequential tunneling through the molecular orbitals dominates the tunneling current. As a consequence, the orbital density of the unperturbed molecular orbitals can be resolved directly in space [Rep05b] (Fig. 2.4c, right panel). Since STM is sensitive to the absolute square of the sample wavefunction (see paragraph "Wavefunction overlap and density of states") rather than the actual wavefunction, phase information of the orbital is lost. Hence, we do not map the actual orbital, but orbital densities. For simplicity, however, I will refer to molecular orbitals rather than orbital densities throughout this thesis.

Scanning tunneling spectroscopy. Whereas STM maps out the spatial structure of electronic sample properties at specific energies, STS measures the energy structure of the sample at specific tip positions. Indeed, rather than resolving atomic spatial features, doing spectroscopy on areas smaller than 10 nm was the original idea of Binnig and Rohrer [Bin87]. Tunneling spectroscopy is implemented by sweeping the bias voltage, and thereby accessing states at different energies, and simultaneously measuring the differential conductance. As we will see, the latter can be linked to the local density of states.

The spatial resolution of energetically localized molecular orbitals shows in a very illustrative fashion that STM is intrinsically energy resolving on atomic scales. In formulas, this is directly intelligible: We simplify equations 2.2 and 2.3 using the Tersoff-Hamann approach (valid for s-wave like tip orbitals as discussed earlier) [Ter83, Ter85, Han87]. At a fixed tip position, it can be assumed that the tunneling matrix element M does not change appreciably in the energy interval of interest. If the tip DOS is a constant over the energy interval of interest and the sample DOS varies unnoticeably in an energy interval corresponding to thermal smearing $k_B T$, the tunneling current is dominated by the sample density of states. Using the Tersoff-Hamann approach for the tunnel matrix element $M \propto \psi(\vec{r_0})$, where $\vec{r_0}$ is the center of curvature of the tip, equation 2.2 simplifies to

$$I(V) \approx \frac{4\pi e}{\hbar} \rho_\mathrm{t} |M|^2 \int_0^{eV} \rho_\mathrm{s}(E_\mathrm{F} + \epsilon) \propto \int_0^{eV} \rho_\mathrm{s}(E_\mathrm{F} + \epsilon, \vec{r_0}) \tag{2.5}$$

such that the differential conductance

$$\left(\frac{\mathrm{d}I}{\mathrm{d}U} \right)_{U=V} \propto \rho_\mathrm{s}(E_\mathrm{F} + eV, \vec{r_0}) \tag{2.6}$$

is directly proportional to the local density of states (LDOS) of the sample at the energy $E_\mathrm{F} + eV$, which is defined as $\rho_s(E_\mathrm{F} + eV, \vec{r_0}) = |\psi(\vec{r_0})|^2 \rho_\mathrm{s}(E_\mathrm{F} + eV)$.

Hence, for a metallic tip with a flat DOS and a sample, whose DOS does not vary much in the energy interval $k_B T$, one can obtain the LDOS by recording the tunneling

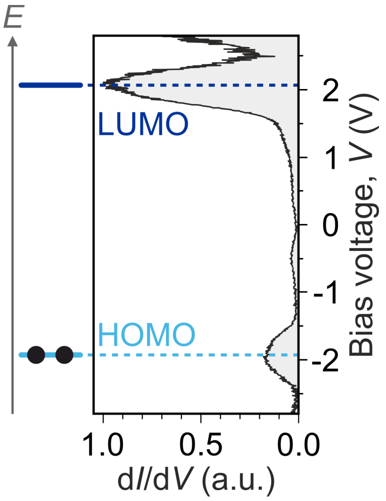

Figure 2.5 | Scanning tunneling spectrum of pentacene on NaCl on Au(111). The discrete energy levels of the molecular frontier orbitals, HOMO (black dots: electrons) and LUMO, appear as peaks in the differential conductance $\mathrm{d}I/\mathrm{d}V$ due to the enhanced overlap of occupied states on one side and unoccupied states on the other side. The spectrum reflects the LDOS of the sample. This figure was adapted from [Coc16] with permission.

current as a function of applied bias voltage. Its derivative $\mathrm{d}I/\mathrm{d}V$ directly yields the sample LDOS. From now on, $\left(\frac{\mathrm{d}I}{\mathrm{d}U}\right)_{U=V}$ will be abbreviated as $\frac{\mathrm{d}I}{\mathrm{d}V}$. The first successful scanning tunneling spectra were shown in 1986 [Ham86, Str86, Ham87, Str87]. An exemplary scanning tunneling spectrum on pentacene is shown in Fig. 2.5. The frontier orbitals appear as peaks in $\mathrm{d}I/\mathrm{d}V$. Hence, select energy levels can be accessed in tunneling spectra. Clearly, the LUMO $\mathrm{d}I/\mathrm{d}V$ peak is much larger than the HOMO peak. When taking a closer look at the formulas describing the tunneling current, it becomes clear that STS is most sensitive to states of highest energy in the bias voltage window (chapter 2.2.4 in [Che07]). This is why, in general, STS probes unoccupied states more efficiently than occupied ones. Nevertheless, both molecular frontier orbitals can be accessed via STS and even their broadening mechanisms can be investigated. In Fig. 2.5, the broadening of the energy levels can be attributed to coupling of the strongly localized electronic states to phonons in the NaCl layer [Rep05a, Rep05b, Rep10].

In conclusion, with STM and STS, the scientific community has established techniques to measure the electronic structure of a surface in both space and energy. The spatial distribution of quantum objects such as electronic wavefunctions can be mapped in real space via STM and discrete energy levels of atoms or molecules can be detected via STS.

Chapter 3

Probing individual molecular energy levels on ultrafast time and atomic length scales

Microscopic videography and control of quantum objects such as an individual molecular orbital has been a major dream of modern sciences as well as nano-, quantum- and bio-technologies. For this goal, major efforts have been invested in order to enhance the temporal resolution of atomically precise microscopes and in particular STM. In this chapter, I discuss ultrafast scanning tunneling microscopy, which allows for ultrafast microscopic videography and forms the basis of all experiments presented throughout this thesis. As discussed in chapter 2, conventional scanning tunneling microscopes can access electronic wavefunctions in space via STM and distinct energy levels in the LDOS by means of STS. Notably, it has been possible to observe select molecular orbitals in STM and STS [Rep05b]. Yet, the dynamics in the nanocosmos, which are responsible for nuclear motion, charge or spin transport take place on femtosecond to picosecond time scales. This is the major driving force behind the immense efforts that have been put into enhancing the time resolution of STM. The innovative technique LW-STM is capable of resolving ultrafast dynamics on atomic length scales by coupling lightwaves into the STM junction. When ultrashort light pulses are focused to metallic tips [Krü11, Her12, Pig13, Wim14, Cia17], the principle of lightwave electronics [Gou07, Bor23] can be exploited such that electrons are steered by the electric field of the light pulse. Coupling terahertz pulses to the junction of an STM in ambient conditions has resulted in ∼500 fs and ∼2 nm precision [Coc13]. Atomic spatial and simultaneous ∼100 fs temporal precision have been achieved by operating in an ultrahigh-vacuum low-temperature STM [Coc16]. Here, single-electron tunneling through select energy levels has even enabled atomic-scale ultrafast movies of individual molecular orbitals [Coc16, Pel20]. This thesis is based on the latter approach, which has started a whole new research field while also setting the bar for other techniques. LW-STM will be explained and put into historical scientific context in section 3.1. Whilst the goal of microscopic videography, to observe individual molecules, has been achieved [Coc16], a method to locally evaluate individual reaction events, which take place on ultrashort time and atomic length scales in a shot-to-shot method remained yet to be demonstrated until ultrafast action spectroscopy was developed [Pel20]. This single-shot detection able to decipher the outcome of statistically governed quantum events will be discussed in section 3.2.

3.1 Lightwave-driven scanning tunneling microscopy

While STM and STS enable the investigation of single atoms and molecules directly in real space, tracking their motion on the intrinsic time and length scales has been a major challenge until recently. In this section, I will introduce LW-STM, which benefits from the best out of two worlds: atomic spatial resolution of STM and temporal precision from ultrafast optics. Only recently, resolving ultrafast dynamics on atomic length scales was achieved employing LW-STM [Coc16]. Before that, many pioneering works aimed at improving the temporal resolution of scanning tunneling microscopy.

Historical overview. To shorten the time window, in which a tunnel current can flow, in several approaches the bias voltage applied to the junction was modulated electronically and optically. Purely electronic tunneling microscopes [Kem07, Lot10, Mou11] allowed for the measurement of spin relaxation times [Lot10] and a fast analogue of STS [Mou11]. However, they have been limited to a 0.3 ns temporal precision due to their finite bandwidth.

Meanwhile, the toolbox of ultrafast photonics offers opportunities to time scales even below picoseconds. The first experiment coupling ultrafast pulses to an STM was shown in [Ham90]. Here, optical pulses have induced a surface photovoltage transiently increasing the tunneling current. In a different approach, the STM was gated using a photoconductive switch [Wei93]. In these experiments, ultrashort laser pulses transiently closed the tunneling circuitry, allowing for 2 ps and 50 Å resolution. However, the time-resolved signal measured in such setups has been found to be dominated by capacitive coupling rather than a time-resolved tunneling current a few years later [Gro96]. In a different scheme, "junction mixing STM" [Nun93], photoconductive switches generated voltage pulses, which propagated onto the sample via transmission lines. Such setups have allowed for combined nanometer and picosecond resolution. Meanwhile, the temporal resolution of all approaches where voltage pulses propagate into the tunnel gap via transmission elements is limited by electronic bandwidths.

A radically different approach is the direct coupling of optical pulses into the STM junction like the pioneering experiment mentioned above [Ham90]. In such experiments, periodically driven tip expansion upon heating by optical pulses [Hub98] can induce artifacts, which can easily lead to interpretation of spurious signals. Whereas technical tricks have been played to extract non-thermal transient signals [Ter10, Dol11], generally, well thought-through rigorous sanity checks need to be implemented, when laser pulses at optical frequencies are coupled to the STM junction. Instead of coupling optical pulses into the STM, terahertz carrier waves can be used to transiently bias the tunneling junction. This idea was first implemented in [Coc13] in ambient conditions allowing for $\sim$500 fs temporal and $\sim$2 nm spatial precision. In the latter publication, rectified currents induced by a terahertz pulse were measured averaging a large number of tunnel events originating from a broad range of electronic states. Actual videography of well-defined quantum states on their intrinsic femtosecond temporal and atomic length scales has been established by introducing state-selective tunneling of single electrons [Coc16] which is available only at stable cryogenic and ultrahigh-vacuum conditions. By sequentially tunneling single electrons through specific molecular energy levels, atomic spatial with simultaneous $\sim$100 fs temporal precision has been achieved [Coc16]. This pioneering work in LW-STM has finally enabled atomic-scale single-molecule ultrafast movies [Coc16, Pel20] and was followed by many other works on LW-STM in ultrahigh vacuum at room temperature [Yos19, Mü20, MS22] and at cryogenic temperatures [Jel17, Pel20, Pel21, Amm21, Abd21, Yos21, She22, Wan22, She24, Roe24, Jel24, Bob24a]. The basis, which LW-STM is built on, lightwave electronics, will be discussed in the next paragraph with all its delicate details to be considered when coupling lightwaves into the microscopic tunnel junction.

Lightwave electronics. In the last decades, techniques have progressed exploiting the sub-cycle variation of the carrier wave of an intense laser pulse to control the motion of electrons in and around atoms. This method has resulted in a significant extension of the frontiers of nonlinear optics and high-field physics [Bra00]. Moreover, it lays the foundation of lightwave-driven charge transport in the sense of microscopic electric currents, so-called lightwave electronics [Gou07].

Historically, this expression was shaped by strong-field experiments in the regime of nonlinear optics [McP87, Fer88]. Here, high-harmonic radiation was generated in gaseous media, based on sub-cycle strong-field light–matter interaction of intense laser pulses with an atom or molecule: one employs such strong fields that they compete with the internal fields in matter tilting the potential barrier of an electron around an atomic core following the transient electric-field profile of the lightwave (Fig. 3.1b). While further studies on high-harmonic generation in gases have shown its potential for generating extremely broadband radiation [Mid11] usable for sub-femtosecond light pulses [Pau01, Hen01], the concept of high-order-harmonic generation has also been adapted to solid state systems [Bor23] pioneering the creation, acceleration and recombination of excitons [Zak12, Lan16] and even allowing for attosecond clocking of electron-hole interactions [Fre22].

For employing the field control of lightwave electronics, it is crucial to work in a regime of light–matter interaction where the electric field of the lightwave is strong enough to compete with the internal fields in matter. In this scenario, electronic dynamics can be driven on time scales even shorter than one oscillation period of the lightwave. Bringing this concept to atomic scales is the goal of LW-STM. To this end, the different regimes of light–matter interaction (Fig. 3.1) need to be understood. Interaction of laser radiation with atoms can lead to processes ranging from multiphoton ionization (Fig. 3.1a) to tunnel ionization (Fig. 3.1b) [Kel64, Cia17]. In the

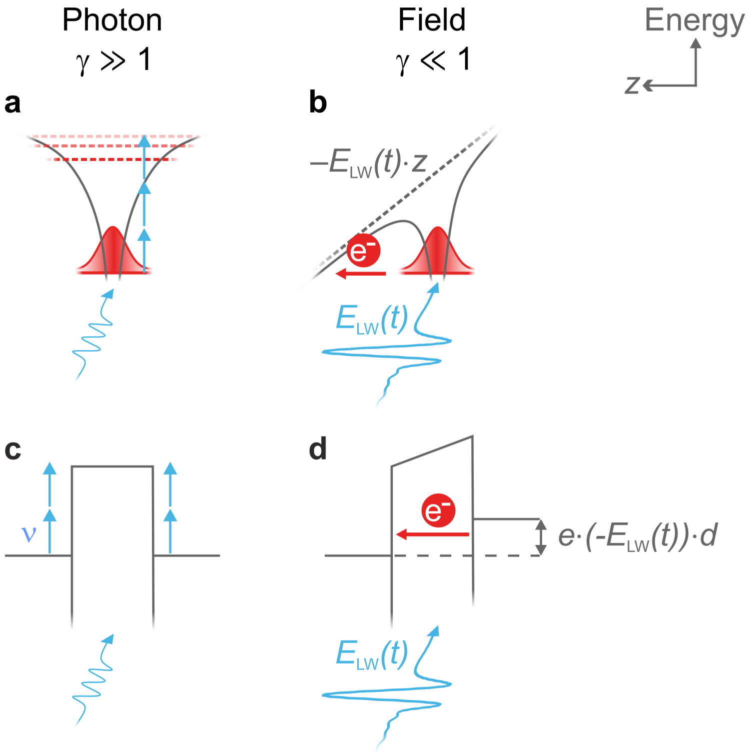

Figure 3.1 | Regimes of light–matter interaction. Two extremal processes of light–matter interaction, light acting as particles (**a**,**c**) or as a wave (**b**,**d**), are depicted for a schematic potential landscape of an atom (**a**,**b**) and the tunnel junction of an STM (**c**,**d**). For an electronic state (red wavepacket) hosted by the atomic potential (**a**) as well as electrons in tip and sample of the STM tunnel barrier (**c**), (multi-)photon excitation (blue arrows) to energetically higher-lying states is more probable in the case of large carrier wave frequencies ν and small electric field strength (Keldysh parameter $\gamma \gg 1$). **b**,**d**, In the strong-field regime ($\gamma \ll 1$), i.e. strong electric fields and low frequencies, the electric field of the lightwave $E_{\mathrm{LW}}(t)$ adiabatically tilts the potential landscape (**b**, dashed line) – yielding the energy difference $e \cdot (-E_{\mathrm{LW}}(t)) \cdot d$ between tip and sample of an STM tunnel junction (**d**). As a result, tunneling out of the atomic potential (**b**) or from one electrode to the other (**d**) can take place.

extreme scenarios, light is either described as a wave or particle (photon). Multi-photon ionization (photon picture) is the ionization of an atom by absorption of several photons, which each have an energy below the ionization threshold. Only the energy of the photons is responsible for the excitation and the shape of the waveform does not play a role. Conversely, in the regime of tunnel ionization, the lightwaves (wave picture) act on electrons like a classical field $E(t)$ leading to a tilt of the potential landscape (Fig. 3.1b). The regime one works in can be characterized by the Keldysh parameter $\gamma = \frac{\sqrt{2m\epsilon}}{eE}\omega_0$ where m is the electron mass, ϵ is the atomic ionization potential, e the elementary charge, E represents the field strength and ω_0 depicts the frequency of the laser radiation [Kel64, Del98]. In the limit of $\gamma \gg 1$, the probability for multi-photon excitations is high. For $\gamma \ll 1$, tunnel ionization is dominating [Kel64, Del98]. For ultrafast lightwave control of electrons, one has to find the right balance between frequency and field strength: by choosing low frequencies and strong fields, the Keldysh parameter decreases. Hence, tunnel ionization is more probable for low frequencies, but the reachable temporal resolution increases with higher carrier wave frequencies at the same field strength. Photon energies of terahertz radiation ($\sim$ meV range) are smaller than typical electron resonances in solids and electronic transitions in molecules of a few electron volts. For such excitations, terahertz pulses act as classical fields and, simultaneously, are fast enough to drive and resolve dynamics on timescales smaller than picoseconds. This is why strong-field radiation in the terahertz spectral range is particularly favorable for driving tunneling processes between molecules and solids by exploiting the method of lightwave electronics.

Lightwave-driven scanning tunneling microscopy. For LW-STM, a lightwave is coupled directly to the STM tip and acts as an ultrafast bias voltage in the junction (Fig. 3.2). The different regimes of light–matter interaction and the transition between them have been characterized for light pulses coupled to metallic tips [Her12, Pig13, Her14]. Starting from localized emission of electrons from sharp metallic tips with 800 nm excitation radiation [Hom06b, Hom06a, Rop07, Bor10, Sch10a, Krü11], local field enhancement of mid-infrared and terahertz radiation at the tip apex [Her12, Wim14] has enabled exploiting the strong-field regime, where field-induced tunneling becomes important. In the extreme limit, field-emitted electrons are semi-classically accelerated in the electric field of the lightwave on

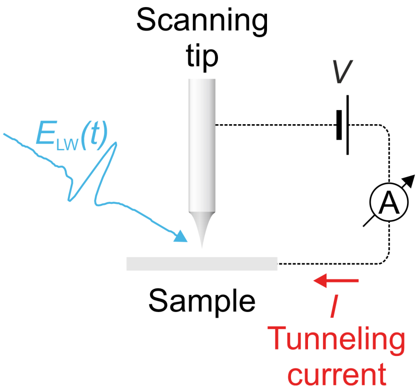

Figure 3.2 | Lightwave as ultrafast bias voltage. A lightwave, $E_{\mathrm{LW}}(t)$, coupled into the STM junction acts as an ultrafast bias voltage and tilts the tunneling barrier. A current driven by the lightwave can be detected when measuring the overall tunneling current I in the STM junction.

sub-cycle time scales [Her14]. Based on this knowledge, the concept of lightwave electronics is exploited in LW-STM in order to drive tunneling processes between tip and sample, solids or molecules. At optical carrier frequencies with $\gamma \gg 1$, multi-photon ionization can excite electrons in the two electrodes, tip and sample, above the vacuum energy without tilting the potential substantially (Fig. 3.1c). Conversely, at $\gamma \ll 1$, the transient tilt of the tunnel barrier by the electric field of the lightwave $E_{\mathrm{LW}}(t)$ dominates the light–matter interaction. Assuming a constant field between tip-apex atom and sample as well as a negligible skin depth in metal, the barrier is tilted by $-e \cdot E_{\mathrm{LW}}(t) \cdot d$. Hence, the lightwave acts as a transient bias voltage $\mathcal{V}_{\mathrm{LW}}(t) = E_{\mathrm{LW}}(t) \cdot d$ such that sub-cycle tunneling currents can be driven (Fig. 3.1d). To work in the latter regime of $\gamma \ll 1$ and to be able to resolve ultrafast dynamics at the same time, we couple terahertz pulses to the tunnel junction, which act as an ultrafast bias voltage applied between tip and sample. The sub-cycle tunneling events driven by the lightwave contribute to the detectable net tunneling current. Depending on an additional steady-state bias voltage V, the measured tunneling current is partly or fully caused by tunneling events driven by ultrashort pulses.

Waveform-averaged rectified currents in LW-STM. In general, the detected current in LW-STM is initiated by both the steady-state bias voltage V and the time-dependent voltage due to the lightwave electric field $\mathcal{V}_{\mathrm{LW}}(t)$. Following the I-V curve of the respective sample, the measured tunneling current consists of a steady-state component I and lightwave-driven components $\mathcal{J}_{\mathrm{LW}}(t)$. As a first approximation, the total tunneling current can be calculated as $I(V + \mathcal{V}_{\mathrm{LW}}(t))$ (Fig. 3.3). This approach is commonly referred to as the “instantaneous tunneling model” and will be discussed

Figure 3.3 | Rectified currents. An ultrafast voltage pulse coupled to the STM junction induces a tunnel current pulse. The instantaneous voltage at any point in time $V + \mathcal{V}_{\mathrm{LW}}(t)$ can be translated to an instantaneous current $I + \mathcal{J}_{\mathrm{LW}}(t)$ based on the I-V curve measured via conventional steady-state STS. The total current detected is the sum of steady-state and lightwave-induced current and averages over charge transfer at all instances in time [Coc13].

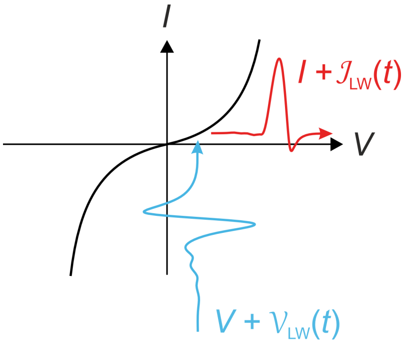

in greater detail in chapter 6. Of today, it is extremely challenging to directly measure the instantaneous tunneling current [Sid24]. Usually, tunneling currents in an STM ranging from picoamperes (pA) to nanoamperes (nA) are amplified before processing by STM control electronics. With a typical bandwidth of one kilohertz (kHz), STM current preamplifiers are far to slow too resolve tunneling on ultrafast time scales. Since the inverse of the bandwidth, namely one millisecond, is orders of magnitude longer than the duration of the entire lightwave as well as the inverse of typical laser repetition rates, the amplified signal always represents an average of the current over the lightwave and often even over many pulse repetition cycles. As a consequence, all tunnel events induced by the steady-state and lightwave-induced voltage, are averaged to the total tunneling current. Via lock-in detection together with an optical chopper, the average total current flowing within one pulse can be extracted [Coc13, Coc16]. This value is the integral over the instantaneous current $\mathcal{J}_{\mathrm{LW}}(t)$ such that the whole transient contributes to the lightwave-driven current. Hence, in first approximation, the temporal precision in measurements of lightwave-driven currents is limited by the duration of the terahertz pulse. Conversely, the picture changes drastically when lightwaves drive tunneling through an individual energy level of an atom or molecule. Such discrete energy levels are exploited in state-selective LW-STM [Coc16] enabling the detection of single-electron tunnel events into specific states on ultrafast time and atomic length scales.

State-selective LW-STM. State-selective LW-STM [Coc16] constitutes one of the main pillars of this thesis and has been employed for all experiments presented in the following chapters. In general, macroscopic rectified currents driven by the

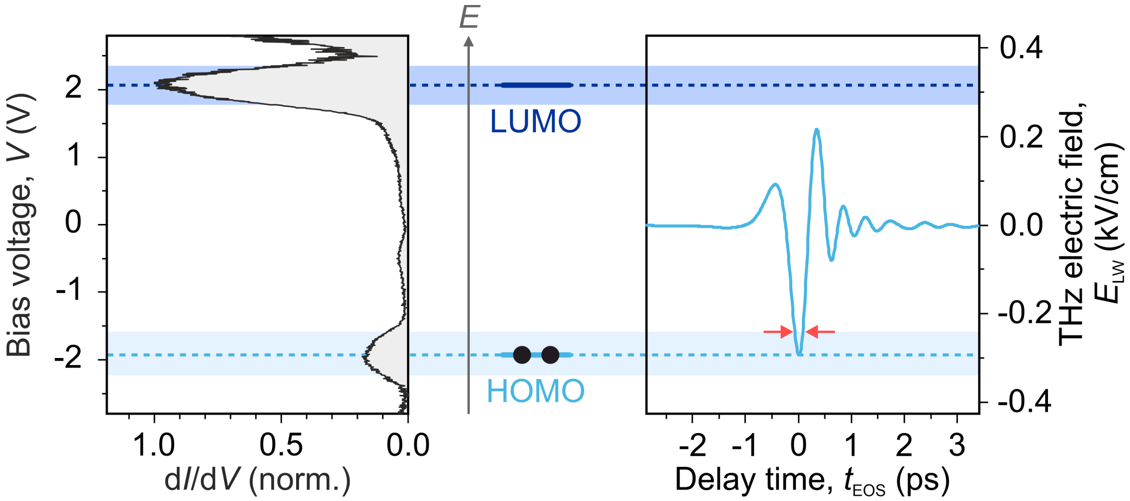

Figure 3.4 | State-selective lightwave-driven STM. In steady-state scanning tunneling spectroscopy, the localized molecular orbitals (center) manifest as peaks in the differential conductance (left). The electric field of the terahertz transient (right) coupled to the STM junction acts as an ultrafast bias voltage. Its peak electric field is tuned such, that only within an ultrashort time window (arrows) at the very field crest, it allows tunneling through a molecular orbital. This figure was adapted from [Coc16] with permission.

whole terahertz transient average over different contributions to the tunneling current stemming from several individual states [Coc13]. In contrast, in state-selective LW-STM, single electrons are sequentially tunneled through specific orbitals within ultrashort time windows (∼100 fs) and simultaneous atomic precision allowing for the investigation of intrinsic dynamics of well-defined quantum states on the atomic scale [Coc16]. This has been achieved by harnessing distinct electronic states of individual molecules or atoms [Coc16, Pel20, Pel21, Roe24, Bob24a] with the aid of ultrahigh-vacuum and low-temperature operation.

The state-selective approach yields several advantages. First, discrete energy levels yield an extremely steeply rising LDOS (chapter 2) such that the temporal precision can be increased: lightwave-driven tunneling currents are dominated by sub-cycle intervals, in which the electric field in the tunnel junction is large enough to induce tunneling through the select levels (Fig. 3.4, red arrows in right panel).

Second, for individual atomic or molecular orbitals, the number of allowed electrons occupying one energy level is limited in contrast to solid materials like metals or semiconductors. Thereby, individual electrons can be tunneled through select quantum states limiting the tunnel currents even more. The detection of quantized tunnel events facilitated by state-selective LW-STM stands in stark contrast to macroscopic currents as known from steady-state tunneling as well as previous ultrafast STM approaches. For a clean interpretation of data, prerequisites of state-selective LW-STM are a single-cycle terahertz transient and access to an individual energy level (Fig. 3.4).

State-selective LW-STM was established in [Coc16] at the University of Regensburg to track the orbital motion of a select molecular level, the HOMO of an individual pentacene molecule. The frontier orbitals (see also chapter 2), HOMO and LUMO, yield peaks in the steady-state $\mathrm{d}I/\mathrm{d}V$ (Fig. 3.4, left and center). To access the HOMO, the electric field of the terahertz transient is attenuated such that only at the field crest, the induced transient voltage in the STM junction can drive sequential tunneling through the molecular level while the steady-state background voltage V is kept close to zero. Thereby, the rectified time-integrated tunnel current $I_{\mathrm{LW}} = \langle \mathcal{J}_{\mathrm{LW}}(t) \rangle$ is strongly dominated by tunneling events of single electrons within a time window much smaller than a single optical cycle of the waveform (arrows). A narrower peak width of the transient, and hence a more asymmetric waveform, yields a higher temporal precision. In the experiments demonstrated by Cocker *et al.* [Coc16], the temporal precision was shown to be about 100 fs. In these experiments, the combination of terahertz waveforms with ultrahigh-vacuum STM at liquid-helium temperature allowed for the atomic spatial resolution of individual molecular orbitals using lightwaves enhancing the spatial precision by more than an order of magnitude as compared to previous work on LW-STM [Coc13].

Both the atomic spatial resolution and the state-selective nature of lightwave-driven tunneling through one select energy level, the HOMO, are evidenced by LW-STM snapshots (Fig. 3.5). In these measurements, the DC background voltage is $V = 15$ mV, which can only induce in-gap tunneling (chapter 2). Meanwhile, the terahertz transient is attenuated such that the field crest induces sequential tunneling through the HOMO as outlined in Fig. 3.4. When scanning the tip across the sample, the purely lightwave-driven current I_{LW} maps out the HOMO in space – here, with $\sim$100 fs temporal precision for every single tunneling event. This ultrashort window of tunneling is much smaller than the inverse of the preamplifier bandwidth such that,

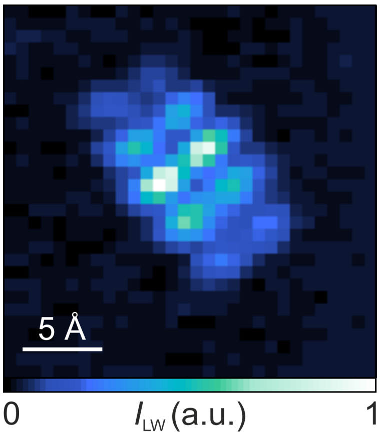

Figure 3.5 | LW-STM snapshot of the pentacene HOMO. A lightwave-driven constant-height scan of pentacene on a NaCl monolayer on Au(110) clearly exhibits the orbital structure of the HOMO. Thirteen LW-STM images were corrected for horizontal drift and averaged. Tip height setpoint: 15 mV, 2 pA and 2.05 Å additional approach.

for the same tip-sample distance, the detected tunneling currents are much smaller than in conventional STM. To counteract the small duty cycle in LW-STM, the tip is moved much closer to the surface for femtosecond snapshots than in conventional STM measurements ensuring a measurable current above the preamplifier detection threshold. With its ultrafast temporal and atomic spatial precision, state-selective LW-STM allows for resolving ultrafast dynamics directly on atomic length scales.

Dynamics on ultrafast time scales. The ultimate goal of all developed fast STM techniques has been to resolve the temporal evolution of structural or electronic dynamics, which are not accessible with conventional electronics, in real space. For the first time, in the experiments published in [Coc16], the motion of an individual molecular orbital could be recorded directly in space. Single-cycle transients allowed for sequential tunneling through a distinct electronic energy level such that every tunnel event was evoked within ∼100 fs on average. Over many terahertz pulses, the time-averaged current was extracted, which was dominated by tunneling events at the field crest of the transient. By accessing a select molecular energy level and performing pump-probe experiments, the vibration of a pentacene molecule above a NaCl decoupling layer was driven and the subsequent ultrafast dynamics were tracked. With these seminal experiments, a technique has been established to record molecular movies directly in space.

3.2 Single-shot detection to decipher local dynamics

The results presented in this section have been measured and interpreted in close collaboration with Dominik Peller, Lukas Z. Kastner, Thomas Buchner, Florian Albrecht, Nikolaj Moll, Rupert Huber and Jascha Repp, and were published in Nature [Pel20], where the authors' contribution is specified. The presentation of the results closely follows the publication. Most figures are adapted from [Pel20] with permission.

The field of LW-STM on atomic length scales has evolved in manifold directions – from a material perspective, from single molecules [Coc16] via bulk solids [Jel17, She22] to two-dimensional systems [Amm21, She24, Roe24, Bob24a], in terms of optical pump pulses [Yos19, Mü20, Yos21, MS22], and in particular, LW-STM has been driven towards quantum sensing. In lightwave-driven tomography exploiting different tip heights, the vertical wave function decay of individual orbitals of graphene nanoribbons could be measured locally at different tip positions in LW-STM with ångström lateral resolution [Amm21]. The use of H_2 adsorbed on a Cu_2N surface has enabled measurements of the surface chemical environment distribution in LW-STM [Wan22].

In all these pioneering experiments, a large number of individual tunnel events was averaged. Such a procedure allows us to follow classical motion directly in space and time. However, quantum objects are governed by statistical probabilities. To directly observe quantum properties or irreversible chemical reactions with all different reaction paths, a single-shot technique is required rather than an average probing mechanism [Pel20, Pel21]. In this section, I introduce the single-shot technique ultrafast action spectroscopy. For this purpose, we make use of state-selective LW-STM and apply it to a system with binary outcome, a single-molecule switch.

The single-molecule switch MgPc on NaCl. For our single-shot detection, we select a molecular switch, which has been characterized in detail using time-integrated experiments [Pat19a]. From steady-state experiments [Sch13, Zha16, Miw16, Ima16, Dop18, Pat19a], it is known that specific molecules can switch between different adsorption geometries on a surface. For magnesium phthalocyanine (MgPc), this

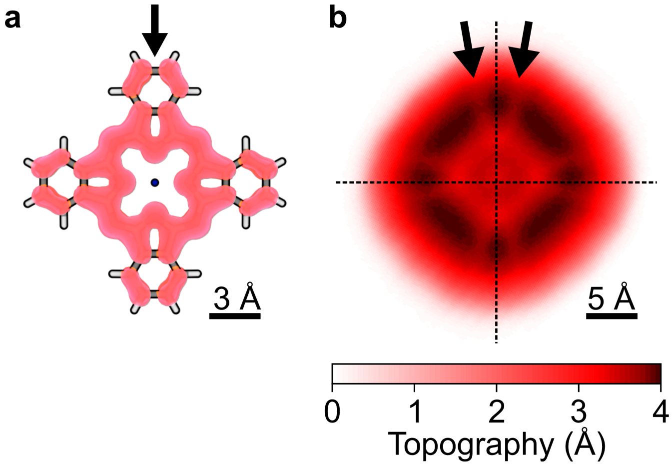

Figure 3.6 | Simulated and measured LUMO densities of MgPc. a, MgPc possesses two degenerate LUMO orbitals. The simulated incoherent sum of the LUMO densities on top of a stick model of the molecule exhibits nodal planes centered on the isoindole units (arrow). **b**, STM constant-current topographic map of the LUMO ($V = 1.1$ V, $I = 2$ pA). Charging events through the LUMO trigger switching of MgPc between two different adsorption geometries on the substrate. This process is happening repeatedly during acquisition of every single pixel of the STM image. As a result, the constant-current map represents a superposition of the electron densities in the two adsorption geometries yielding two nodal planes around the high symmetry directions defined by the NaCl lattice underneath (dashed lines) instead of one (**a**).

is the case, when it adsorbs on a Cl^- site of a NaCl layer [Pat19a, Pel20]. In the simulated LUMO densities of MgPc (Fig. 3.6a), one electronic nodal plane is apparent on each isoindole unit (arrow). Meanwhile, STM images at the LUMO energy exhibit two nodal planes instead of one due to the switching behavior of MgPc (Fig. 3.6b, arrows). On Cl^- sites, MgPc adsorbs in two different geometries rotated by an azimuthal angle of $\phi = \pm 10°$ with respect to the underlying salt layer (Fig. 3.7a,c). The two stable structural configurations of the molecule in its electronic ground state can be described by a double-well potential U as a function of rotation angle ϕ (Fig. 3.7d). The molecule can be switched between the two geometries upon charging, in a process of sequential tunneling through a molecular orbital (chapter 2). Starting from the electronic ground state, the neutral molecule lies in one of the adsorption geometries, rotated to the left, $|l\rangle$, (Fig. 3.7a) or right, $|r\rangle$ (Figs. 3.7c). Upon tunneling an electron into the LUMO (first step of sequential tunneling), MgPc tends

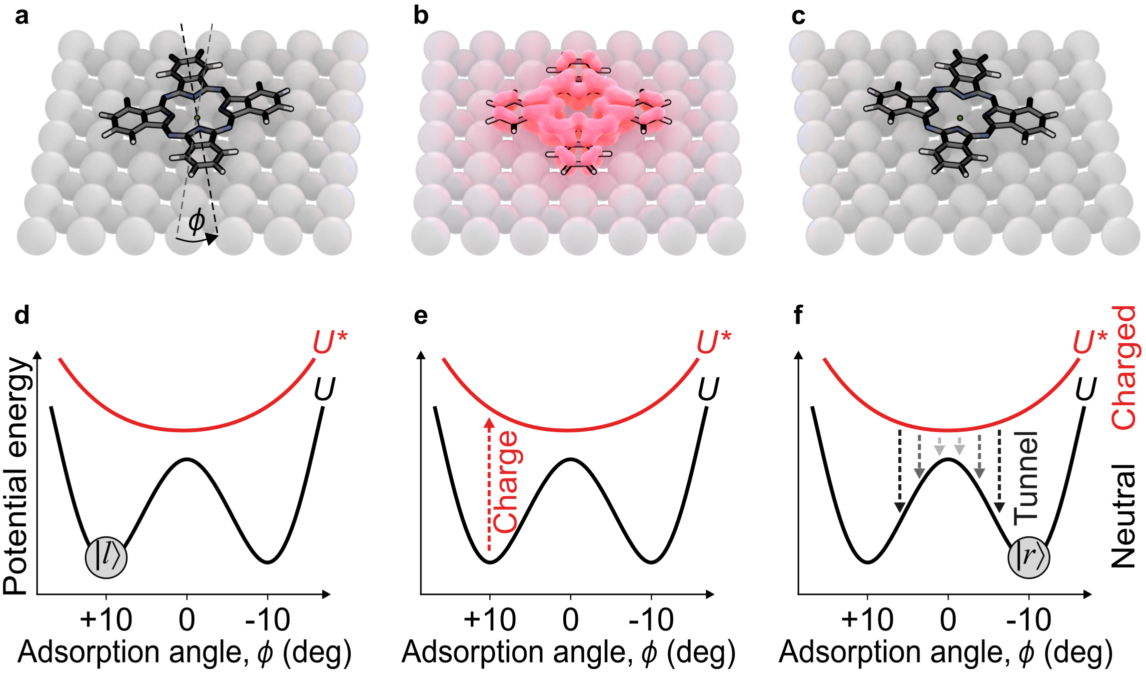

Figure 3.7 | Charge-induced switching of MgPc adsorbed on a Cl atom in NaCl. **a**, In its electronic ground state, the MgPc molecule adsorbs in either of two degenerate, mirror-symmetric ground states, $|l\rangle$ (shown) and $|r\rangle$ (**c**), rotated by $\phi_{l,r} = \pm 10°$ with respect to the underlying NaCl lattice. **b**, When charged, the molecule tends to align with the high-symmetry axis of the NaCl lattice [Pat19a]. These adsorption geometries give rise to two different potentials for the uncharged and the charged scenario (**d-f**). **d**, When adsorbed in $|l\rangle$ (**a**), the molecule lies at $\phi = +10°$ in one of two minima ($\phi = \pm 10°$) of the equilibrium potential U separated by a barrier. The charged molecule, e.g. when filling the LUMO with one electron, feels the potential U^* with a single miminum at $\phi = 0°$ such that a charging event triggers an in-plane rotation of the molecule towards $\phi = 0°$. Depending on the exact position of the molecule in the potential U^* at the time of neutralization by a tunnel event out of the LUMO (dashed arrows), the second step of sequential tunneling through the molecular orbital can result in a switching event to the right-rotated ($\phi = -10°$) adsorption geometry (**c**) – or the molecule can fall back into its initial state (**a**, **c**). As a result, the molecule can be switched between the two adsorption states by charging.

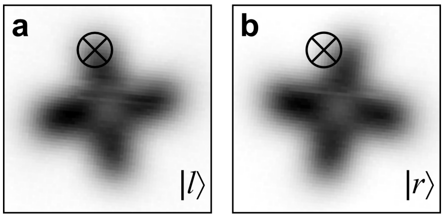

Figure 3.8 | In-gap STM images of the molecular switch. Low-voltage scans enable the detection of the neutral molecule in both adsorption geometries, $|l\rangle$ (**a**) and $|r\rangle$ (**b**), separately (constant-height mode, $V = 6$ mV, image size 20 Å × 20 Å, linear grey scale 0–2 pA). Placing the scanning tip to the cross-hair position, the detection current driven by the small bias voltage V differs considerably for $|l\rangle$ and $|r\rangle$.

to align with the high-symmetry axes of the underlying salt layer [Pat19a, Pel20] (Fig. 3.7b). The charged molecule is subject to a potential with a single minimum at zero degree rotation (Fig. 3.7d). When the electron tunnels out of the LUMO (second step of sequential tunneling), the molecule is neutralized (Fig. 3.7c,f). Depending on the position in the potential of the charged molecule U^*, the molecular switch can fall into one of the minima of the double-well potential of its electronic ground state – back into its initial adsorption geometry ($|l\rangle$, Fig. 3.7a) or into the other stable configuration ($|r\rangle$, Fig. 3.7c). As a consequence, by charging, the molecule can be switched from one adsorption geometry into the other with a certain probability.

In order to image the two adsorption geometries without switching between them, one can record STM images at voltages well below the LUMO in so-called in-gap images (Fig. 3.8). At very low voltages, the molecule modifies the tunnel barrier, which is visible in in-gap images. Yet, no sequential tunneling through molecular orbitals takes place (chapter 2). Since the voltage does not suffice to charge the molecule, the molecular switch does not toggle between the two adsorption geometries while being imaged. It rests in one of the two geometries. Clearly, in such images the left (Fig. 3.8a) and right (Fig. 3.8b) rotated geometry can be identified. However, the two configurations can be discerned even without taking a whole image. At the cross-hair position marked in Fig. 3.8a,b, the measured in-gap detection current differs for the two geometries: it is larger for $|l\rangle$ than for $|r\rangle$. When a single tunneling event switches the molecule, the two adsorption geometries can be distinguished by leaving the tip at this very position and recording the detection current. The principle of discerning different molecular conformations is well established in steady-state experiments [Sti98, Qiu04, Sai05, Lil07] and has even been brought to sub-picosecond

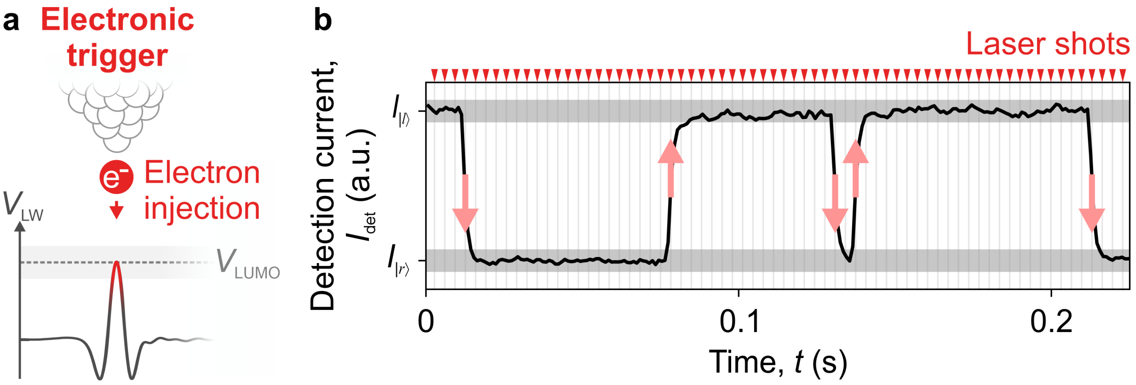

Figure 3.9 | Ultrafast action spectroscopy. **a**, For a time window of about 100 fs (red field crest), a lightwave opens a tunneling channel through the LUMO such that a charge injection can trigger a switching event of the molecular switch. **b**, Positioning the tip at a fixed location (e.g. cross-hair position in Fig. 3.8), the adsorption geometry of the molecule is monitored by an in-gap detection current I_{det} (black curve). Individual lightwaves (laser shots) repeatedly inject electrons into the LUMO enabling switching events between $|l\rangle$ and $|r\rangle$. Every switching event manifests as an abrupt change of the detection current, which is registered for each laser shot, separately for both directions (arrows).

time scales [Li17]. We develop a technique to controllably induce switching of MgPc within a fraction of a single cycle of light and to detect every single switching event, in ultrafast action spectroscopy.

Ultrafast action spectroscopy. Whenever a voltage capable of charging our molecular switch is applied to the STM junction continuously, the molecule toggles between the two adsorption geometries in an uncontrolled fashion. In contrast, with the help of LW-STM we can evoke a single switching event within 100 fs by charging the single-molecule switch MgPc using our terahertz transient. Tuning the field amplitude of the terahertz pulse to the LUMO energy, the molecule can be charged within 100 fs and hence the molecule can switch into the other adsorption geometry (Fig. 3.9a). We do this repeatedly and simultaneously monitor the in-gap detection current continuously while switching the molecule (Fig. 3.9b). For every laser shot, we read out whether the molecule has switched: a step in the detection current corresponds to a switching event of the molecule (arrows). From high current to low current, the molecule switches from the left- to the right-adsorbed configuration and vice versa. To ensure that every switching event can be resolved, the repetition rate of the laser pulse is lowered to ~300 Hz lying within the bandwidth of the current preamplifier, which is about 1 kHz. With lightwave-induced tunneling rates below 0.4 electrons per pulse [Pel20], the probability of two switching events within one laser pulse becomes negligible. Concluding, every single switching event of the molecule can be detected. Based on single-molecule action spectroscopy [Bö19], we label our single-shot technique as ultrafast action spectroscopy since the temporal confinement of tunneling allows for ultrafast temporal precision. Due to its single-event sensitivity, ultrafast action spectroscopy enables us to access the full switching statistics of an individual molecule even for both switching directions separately.

Spatially resolved single-shot detection. Remarkably, the reaction statistics cannot only be extracted in a direction-dependent fashion, but this can also be done spatially. At one specific position of the tip, one can extract the switching statistics of the two different reaction paths from left to right and right to left. Evaluating the detection current (Fig. 3.9) at different tip positions yields spatial maps of the local switching probability for both directions individually, $p_{\text{l-r}}$ (Fig. 3.10a) and $p_{\text{r-l}}$ (Fig. 3.10b). Pixels where switching cannot be detected are shown in white.

The switching maps reveal a rich sub-molecular structure and a clear direction dependence. For both directions, the switching probability is locally enhanced in eight areas (indicated by dashed circles), every other of which is more prominent. The axes of the molecule in its initial state are marked by dashed lines. Interestingly, the switching probability is aligned with these axes.

As discussed earlier, every switching event is triggered by a charging event. Hence, the local switching probability is expected to be intricately linked to the local charging probability of the LUMO. The latter can be calculated from the overlap integral of the tip wave function and the LUMO orbital obtained from DFT calculations [Pel20] (Fig. 3.11). The tip wave function is approximated by an s-like wave function (Tersoff-Hamann approach, chapter 2) with an exponential decay length of 0.6 Å being centered at a distance of 9 Å above the topmost NaCl layer. Figure 3.11 visualizes the efficiency, with which an electron can be injected into the LUMO in the respective adsorption geometry.

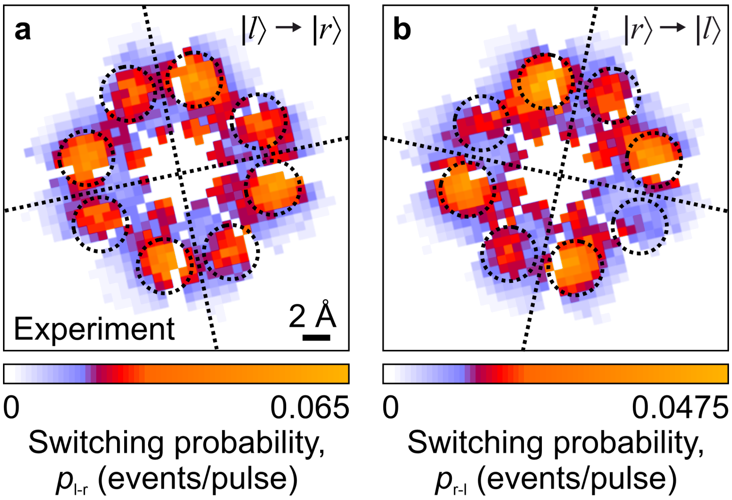

Figure 3.10 | Local maps of switching probability. For different tip positions across the molecule, the switching statistics for both switching directions are detected to extract the local switching probabilities, $p_{\text{l-r}}$ from $|l\rangle$ to $|r\rangle$ (**a**) and $p_{\text{r-l}}$ from $|r\rangle$ to $|l\rangle$ (**b**). The spatial maps reveal sub-molecular features and a clear direction dependence. Pixels where switching cannot be detected are depicted in white. Eight areas of enhanced switching probability stand out (dashed circles), every other of which is more prominent. The symmetry axes of the molecule in the initial state are indicated by dashed lines.

Indeed, the similarities of switching and charging maps cannot be overlooked: the switching maps clearly resemble the local charging probability of the respective initial state. At positions, where an electron can be injected efficiently into the LUMO in a specific adsorption geometry, the switching probability is higher. When an electron has tunneled into the LUMO, the probability for the molecule to switch even seems to be roughly constant such that the switching probability is directly proportional to the local charging probability.

With our novel sampling technique, ultrafast action spectroscopy, we establish a method to locally sample the reaction statistics of a single-molecule switch shot by shot. In the following chapters, I will show how ultrafast action spectroscopy opens the doors for controlling and observing the action of ultrafast force pulses on select atoms within an individual molecule (chapter 4) and to directly measure atomic-scale near-field transients in a tunnel gap of only a few ångströms (chapter 5).

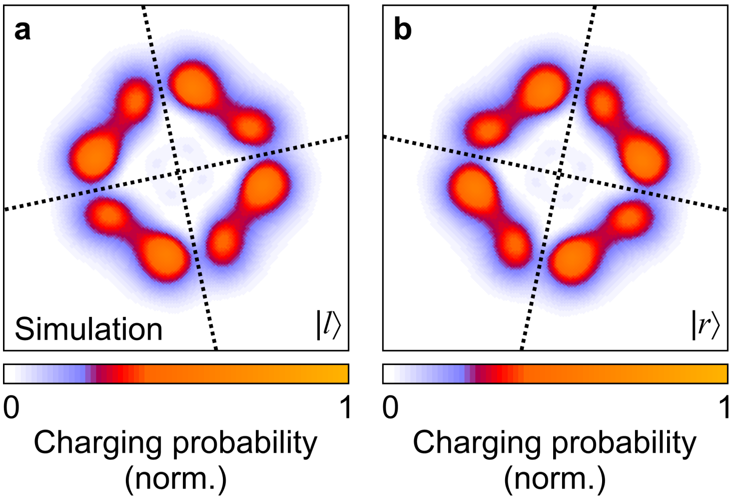

Figure 3.11 | Local maps of simulated charging probability. The local probability to tunnel an electron into a LUMO is calculated as the square of the respective overlap integrals M between tip and orbital electronic wavefunction for both adsorption geometries $|l\rangle$ (**a**) and $|r\rangle$ (**b**). The tip wave function is approximated as an s-wave with a decay length of 0.6 Å and centered 9 Å above the top-most NaCl layer.

Chapter 4

Controlling single-molecule motion

> *What's the use of doing all this work if we don't get some fun out of this?*
>
> — Rosalind Franklin [Klu05]

The results presented in this chapter have been measured and interpreted in close collaboration with Dominik Peller, Lukas Z. Kastner, Thomas Buchner, Florian Albrecht, Nikolaj Moll, Rupert Huber and Jascha Repp, and were published in Nature [Pel20], where the authors' contribution is specified. The presentation of the results closely follows the publication with figures adapted from [Pel20] with permission.

Based on the techniques developed and explained in chapter 3, I will now show how we have established ultrafast forces steering atomic motion in an individual molecule. In real space, atomic manipulation on individual molecules is a well-established method in the realm of scanning probe microscopy. Quasi-static forces have been applied locally to assemble new quantum structures [Esa18] in scanning probe techniques and even chemical reactions have been induced using external stimuli [Hla00, Pav17, Alb22]. While the available forces have been quasi-static, exploiting ultrafast local dynamics would open the doors to tailor chemical reactions or conformational changes of individual molecules giving access to a new era of nanotechnology. With the development of LW-STM (section 3.1), it has become possible to selectively access specific molecular energy levels within a time window of about 100 fs – even in a single-shot fashion [Pel20] (section 3.2) – which can be used to observe ultrafast molecular motion [Coc16]. In this chapter, I demonstrate how we not only sample, but even coherently control the motion of the single-molecule switch introduced in section 3.2. We induce a librational motion of the switch by applying ultrafast force pulses to specific atoms driving the molecule out of its equilibrium position.

To do so, we utilize the electic field of the terahertz transient coupled into the STM junction as an electrostatic force pulse, acting on ultrafast time scales. In contrast, operating the molecular switch between two adsorption geometries is done by charging. By calibrating the peak electric near field in the junction (section 4.1) as a voltage, we can disentangle the action of the near-field waveform as an ultrafast force pulse or a trigger of charging events.

4.1 Energy calibration via a local voltage sensor

We utilize the switching behavior of MgPc on NaCl (see section 3.2) to calibrate the peak electric near field in the junction in units of volts. In a regime, where the peak field of the terahertz transient does not suffice to charge the molecular switch, its electric field can still result in a force acting on the molecule. To disentangle these regimes, it is crucial to calibrate the peak field in the STM junction in units of volts. To this end, we identify the lightwave-induced peak voltage when accessing a select energy level. This is achieved by using the molecular switch (section 3.2) as a local peak-voltage sensor.

We know that the molecular switch can only toggle between its adsorption geometries upon a charging event, for instance by tunneling an electron into the LUMO, as shown in the previous chapter. Moreover, the switching probability seems to be directly proportional to the charging probability (Figs. 3.10 and 3.11). To calibrate the electric field in the STM junction, we sweep the peak electric field of the terahertz transient across the LUMO resonance (Fig. 4.1a). For different peak electric fields and hence lightwave-induced peak voltages (color-coded), one can record the switching probability of the molecular switch (Fig. 4.1b). When the peak electric field suffices to induce a voltage capable of charging the molecule, the switching probability rises steeply (around 0.2 E_0, E_0: maximum electric field). Inversely, the steep

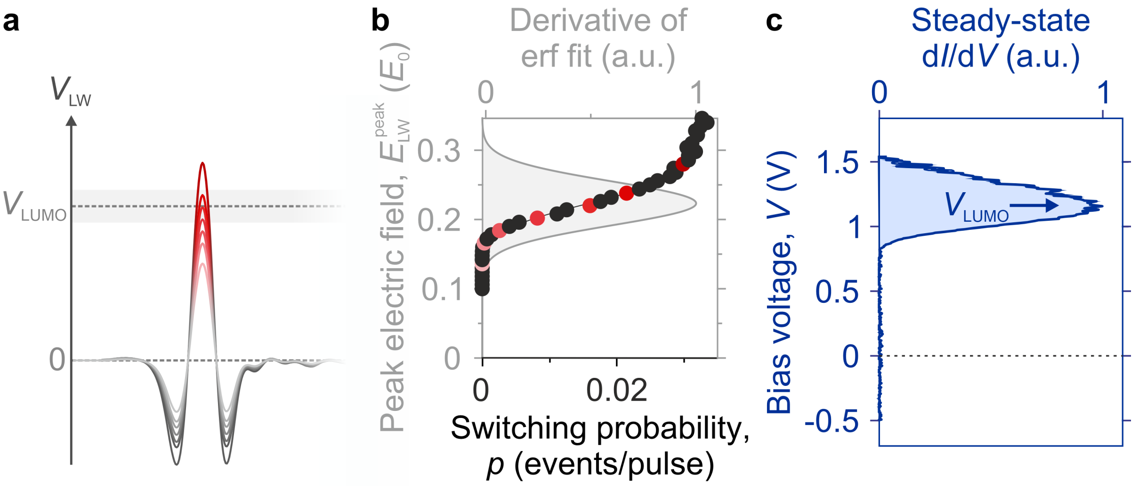

Figure 4.1 | Determining the lightwave-induced peak voltage. a, The peak electric field $E_{\mathrm{LW}}^{\mathrm{peak}}$ of the terahertz transient is attenuated such that the instantaneous peak voltage induced in the STM junction sweeps over the LUMO resonance of the single-molecule switch, MgPc on NaCl, at V_{LUMO}. Charging enables switching of the molecule. **b**, The switching probability p of the single-molecule switch (data points) is recorded as a function of the respective peak electric field and fitted by an error function. Upon enabling tunnel events through the LUMO, the switching probability rises steeply. By attributing the peak in the derivative of the error function (gray curve) to the LUMO peak in the steady-state $\mathrm{d}I/\mathrm{d}V$ (**c**), V_{LUMO}, the peak electric field can be calibrated in units of volts.

rise in the switching probability corresponds to tunneling into the LUMO. As the LUMO resonance is broadened due to its interaction with phonons in the NaCl layer underneath [Rep05a, Rep10] (STS, chapter 2), it is Gaussian-shaped with the integral being an error function. Based on the assumption that the switching probability is directly correlated with the charging probability of the molecule, the switching probability is fitted by an error function, whose derivative (gray) peaks at a specific peak electric field. We attribute the latter to the voltage V_{LUMO} of resonant tunneling through the LUMO, which appears as a peak in the steady-state tunneling spectrum $\mathrm{d}I/\mathrm{d}V$ (Fig. 4.1c) at around 1.2 V.
Assigning the LUMO peak in the steady-state $\mathrm{d}I/\mathrm{d}V$ (Fig. 4.1c) to the maximum derivative of the error function fit (Fig. 4.1b), the peak field in the STM junction can be calibrated in terms of a lightwave-induced peak voltage. For the tip used in this experiment, the unattenuated terahertz waveform E_0 induces a peak voltage of 5.2 V.

4.2 Sub-cycle dynamics of a molecular switch

Knowing the calibration of the peak electric field strength in units of volts (section 4.1), we want to measure and control sub-cycle dynamics of the molecular switch with direct real-space access. Indeed we find that we can coherently steer molecular motion and modulate the switching probability of the single-molecule switch. Here, the key idea is to use the electric field of the near-field waveform confined to the atomically sharp tip as an atom-scale force pulse. To do this, we apply the lightwave-induced ultrafast voltage pulse to the single-molecule switch without charging it.

Concept: coherent control via ultrafast force pulse. For a better understanding of the different aspects of our experiments, the conceptual idea of how to manipulate the single-molecule switch is presented in the following. This is a purely schematic model, which will be corroborated by our results presented in this section and section 4.3. The switching motion of the single-molecule switch itself is an azimuthal rotation. We exploit this in the following manner: exciting a coherent azimuthal oscillation of the molecular switch (Fig. 4.2a) with an ultrafast force pulse might alter the switching probability of the molecule. A rotation of the uncharged

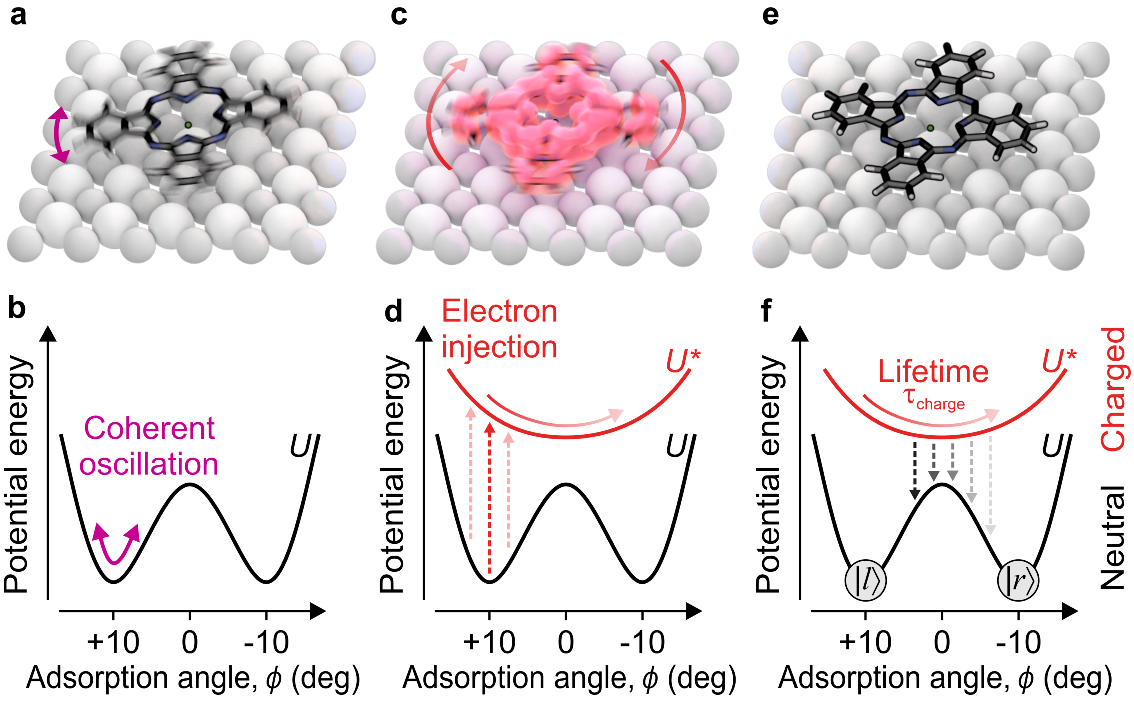

Figure 4.2 | Coherent oscillation modulates switching probability. When the uncharged MgPc molecule oscillates azimuthally around one of the two stable adsorption geometries (**a**), its position in the double-well potential U changes (**b**). Injecting an electron into the LUMO of the rotating molecule (**c**, vertical transitions in **d**) prompts an in-plane rotation of the molecule towards $\phi = 0$, strongly influenced by the previous rotational dynamics. Depending on injection position, lifetime τ_{charge} and hence the specific position in U^* when the molecule is discharged (**f**), the switching probability into the other adsorption geometry (**e**) is altered.

molecule changes the adsorption angle within one of the minima of the double-well potential (Fig. 4.2b). While the molecule is oscillating azimuthally, the overlap of tip and molecule wave functions changes in time, which also modulates the probability to charge the molecule. Hence, the probability to switch the molecule upon inducing a coherent oscillation is expected to change in time. Depending on the instance when the molecule is charged (Fig. 4.2c), it will end up at a different location in the parabolic potential of the charged molecule (Fig. 4.2d). After the lifetime τ_{charge}, the molecule is located at a specific position in the potential U^* (Fig. 4.2f) and neutralizes by tunneling an electron out of the LUMO such that it ends up in one of the uncharged adsorption geometries (Fig. 4.2e). This tunnel neutralization can occur stochastically at different instances in time for every single switching process (Fig. 4.2f, multiple arrows). Hence, the probability to switch into the other geometry might be altered from shot to shot. For many individual shots, however, the average position in U^* after lifetime τ_{charge} and also the time-dependent switching probability are expected to be governed by the molecular motion induced by the ultrafast force pulse even before charging the molecule (Fig. 4.2a,b). As a consequence, by applying a force pulse to the molecular switch, which induces an azimuthal oscillation of the molecule without charging it, we should be able to coherently modify the switching probability in time.

Temporal modulation of the switching probability by force pulses. The idea of the experimental implementation is sketched in Figure 4.3a. To apply an ultrafast force pulse, we couple a terahertz pulse into the STM junction, whose electric field strength is attenuated such that the lightwave-induced peak voltage $V_{\text{LW}}^{\text{pump}}$ is not large enough to charge the molecule. However, the oscillating electric field can excite a coherent librational motion (bottom) – this will be further confirmed in section 4.3. After a delay time τ, a terahertz pulse with larger field strength is able to inject an electron into the LUMO and thereby induce a switching event into the other adsorption geometry. For the setting of one specific delay time τ, the adsorption geometry after every pulse pair can be extracted (Fig. 4.3b) via ultrafast action spectroscopy (section 3.2). Thereby, the switching statistics of the single-molecule switch are accessible for a specific delay time τ. If the force pulse induces an azimuthal rotation of the molecular switch on the substrate, this will be visible in the switching statistics for different delay times between pump pulse and electronic trigger. Hence, depending on the time of charge injection, we expect a modified switching probability of the molecule. For each delay time τ, we extract the switching probability $p(\tau)$ of the single-molecule switch using our single-shot detection (Fig. 4.4). Clearly, the switching probability is modulated as a function of delay time and oscillates with a frequency of about 0.3 THz. This frequency matches the frustrated in-plane rotation frequency calculated by DFT [Pel20]. Flipping the pump transient coherently inverts the phase of the oscillatory signal. Whereas the mean value of the switching probability stays almost constant, the peak-to-peak amplitude of the oscillation is inverted. This observation indicates field-induced

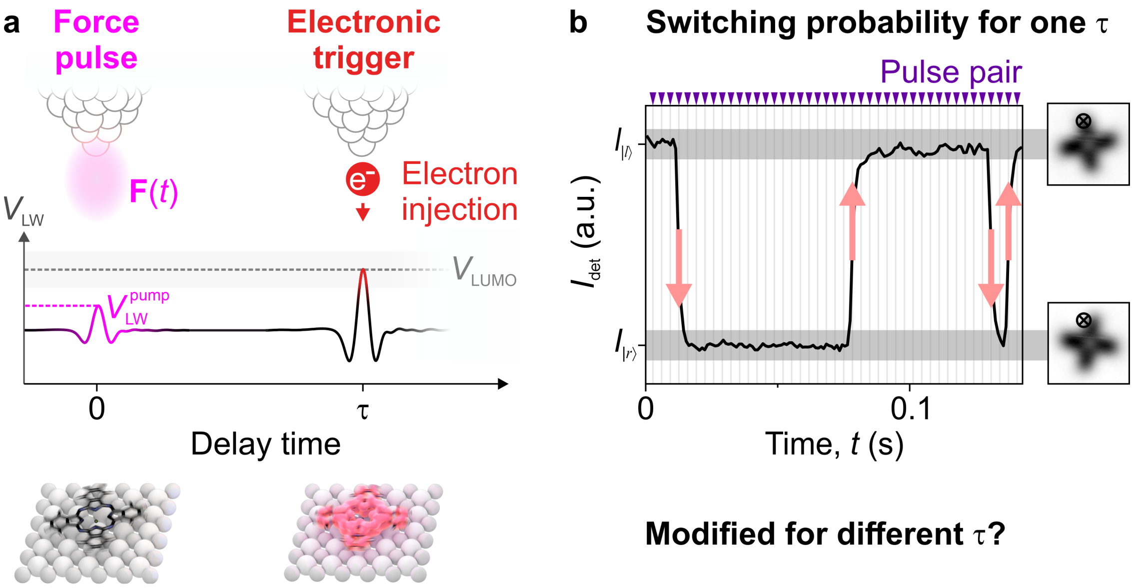

Figure 4.3 | Pump-probe action spectroscopy. **a**, In a pump-probe scheme, pairs of terahertz pulses separated by an adjustable delay time τ trigger switching events. The pump pulses are adjusted below the threshold of electron tunneling ($V_{\mathrm{LW}}^{\mathrm{pump}} < V_{\mathrm{LUMO}}$) acting as an ultrafast force pulse $\mathbf{F}(t)$ to induce molecular dynamics. In contrast, the probe pulses serve to inject single electrons into the LUMO and prompt time-delayed switching events, whose probability is influenced by the molecular motion. **b**, The impact of molecular motion on the switching probability can be interrogated by ultrafast action spectroscopy (section 3.2) for pulse pairs with variable delay time τ. The action of the pump pulse is expected to vary the switching probability of the single-molecule switch as a function of τ.

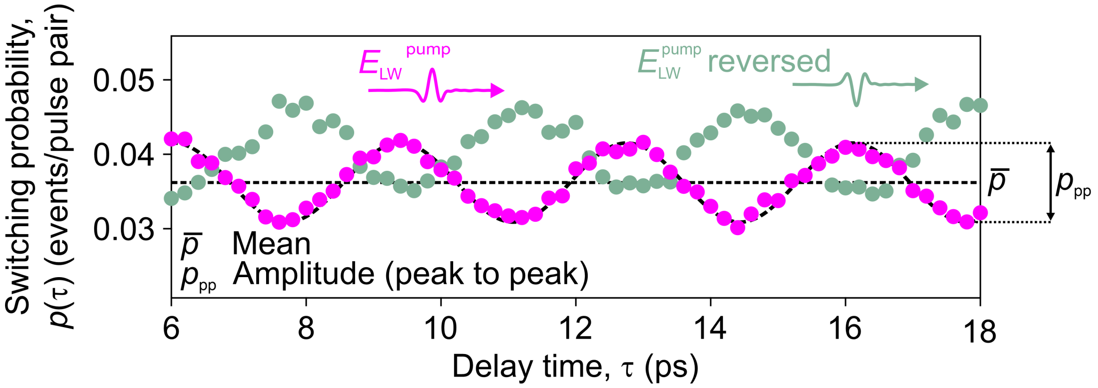

Figure 4.4 | Pump-probe switching probability trace. Upon action of a pump electric field, the switching probability $p(\tau)$ as a function of delay time oscillates with a frequency of 0.3 THz (pink data points, $V_{\mathrm{LW}}^{\mathrm{pump}} = 0.7$ V). Inverting the polarity of the pump pulse coherently reverses the phase of the oscillatory signal (green data points).

dynamics rather than oscillations due to charging (suggested mechanism in [Coc16]) and drives us to analyze the impact of the pump field strength on the transient switching probability.

Field-driven dynamics. To disentangle the impact of the pump electric field and tunnel events driven by the pump pulse, we vary the pump field strength and hence the transient voltage applied across the tunnelling junction, $V_{\mathrm{LW}}^{\mathrm{pump}}$, from below to above the threshold for electron injection into the LUMO, while keeping the amplitude of the probe pulse constant. For each setting, we record one oscillation period of the switching probability as a function of the delay time (Fig. 4.5a). From sine fits to these curves, we can extract the mean switching probability $\bar{p}$ and the peak-to-peak amplitude of the oscillation p_{pp}, as labeled in Fig. 4.4. For low peak voltages, the mean switching probability is constant (Fig. 4.5b). Clearly, only above a certain peak voltage of the pump field, the mean value of the switching probability changes. The reason for this is that below $V_{\mathrm{LW}}^{\mathrm{pump}} = 0.7$ V, solely the probe pulse induces switching events of the molecular switch. At peak voltages $V_{\mathrm{LW}}^{\mathrm{pump}} > 0.7$ V, also the pump pulse itself can induce tunneling events increasing the mean switching probability.

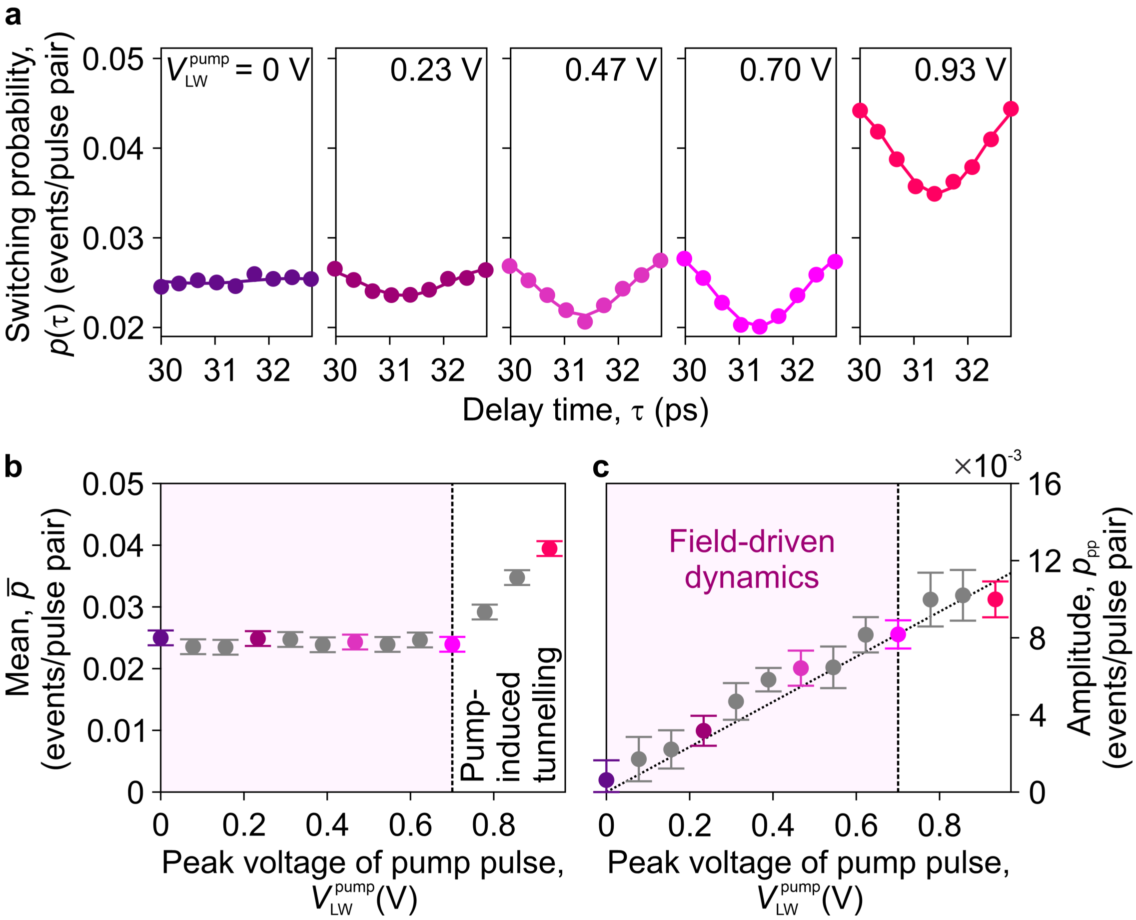

Figure 4.5 | Field stimulus acting on single-molecule switch. a, One oscillation period of the time-resolved switching probability traces, $p(\tau)$, is recorded for several peak voltages $V_{\mathrm{LW}}^{\mathrm{pump}}$ induced by the pump pulse. The probe field strength is kept constant. Each data set is fitted by a sine function (solid lines), from which the time-averaged mean, $\bar{p}$, and the modulation amplitude, p_{pp}, are extracted. **b**, The mean switching probability as a function of pump field strength is constant up to $V_{\mathrm{LW}}^{\mathrm{pump}} = 0.7$ V (shaded area) and increases rapidly at higher peak voltages. Voltages induced by the pump pulse $V_{\mathrm{LW}}^{\mathrm{pump}} < 0.7$ V are too low to inject electrons into the LUMO such that only the probe pulse induces switching events resulting in a constant mean value $\bar{p}$. Above this threshold, the pump pulse triggers additional electron tunneling and contributes to the overall switching probability. **c**, In contrast, the modulation amplitude, p_{pp}, scales linearly with the pump field strength throughout the measured range, indicating that it is the electric field of the pump pulse, which coherently modulates the switching probability.

In stark contrast, we observe a field-strength-dependent amplitude of the oscillation throughout the whole measured range (Fig. 4.5c). In particular, the peak-to-peak amplitude of the oscillation rises linearly with the peak voltage of the pump pulse, modulating the switching probability severely even in the regime where the pump pulse cannot induce tunnel events. This behavior confirms that the dynamics are field-driven and makes us conclude that the pump electric field itself acts on the single-molecule switch.

The presented results evidence that pump pulses below the tunneling threshold can steer a coherent motion owing to an ultrafast electric-field stimulus. Since an electric field can directly interact with polarizable matter like polar atoms or bonds, we expect a local interaction of the field stimulus with the examined sample – in particular, with polarizable bonds parallel to the electric field. These considerations together with the need to understand the motion pattern modulating the switching probability call for a full spatio-temporal analysis, which is presented in the next section.

4.3 Local action of ultrafast force pulses

In the previous section, we found out that the electric field of a terahertz pulse in the STM junction can be used as a force pulse to induce dynamics of an individual molecule even without charging it. To investigate the microscopic mechanism behind this observation, we analyze the induced dynamics at different positions across the molecule in this section. We find that the force pulse acts locally giving direct access to atomic motion.

Local action of ultrafast force. At different tip positions, we record pump-probe traces of the switching probability using ultrafast pump-probe action spectroscopy (Fig. 4.6). In all these experiments, $V_{\mathrm{LW}}^{\mathrm{pump}}$ is kept just below the tunneling threshold. Obviously, both $\bar{p}$ and p_{pp} vary for different tip positions across the molecule. At some positions, where the mean switching probability is rather high, we find that the pump pulse has a minor impact on the switching probability (Fig. 4.6a, positions marked in Fig. 4.6c). At positions only a few ångströms apart, the average switching probability is comparably low. Surprisingly, here, we observe a strong pump-induced

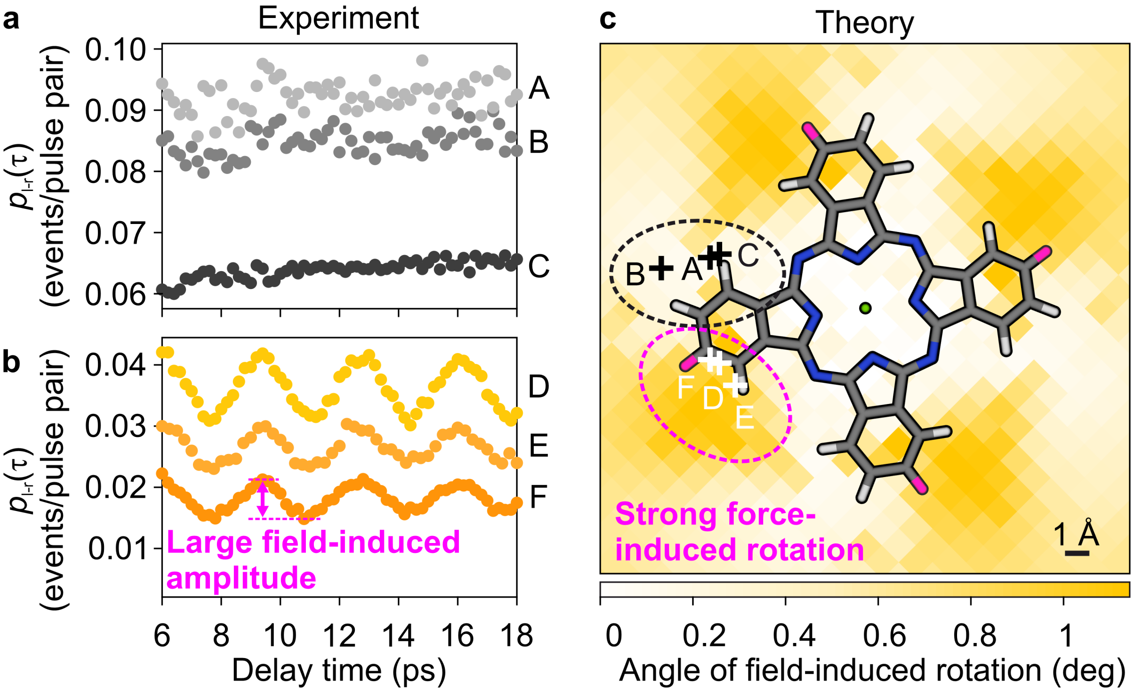

Figure 4.6 | Field-induced azimuthal rotation. a,**b**, Time-resolved traces of the switching probability at different tip positions (marked as crosses labeled A to F in **c**) reveal strong lateral variations in the amplitude of the field-driven modulation. In areas of high mean switching probability (**a**), no pump-induced modulation is observed. Conversely, at a position displaced by only a few ångströms, where the mean switching probability is smaller (**b**), the field-induced modulation is maximized. **c**, Computed by DFT calculations, the color map visualizes the action of a local out-of-plane electric field located at different positions (pixel coordinates) as an atomic-scale force. With strong local variations, the electric field induces an in-plane rotation of the MgPc molecule. It is maximized (pink dashed line) at positions of enhanced switching probability modulation (**b**). A top view of the calculated initial adsorption geometry, the molecule without applied field, is overlaid with specific hydrogen atoms highlighted in pink.

modulation of the switching probability (Fig. 4.6b). This severe lateral variation of pump-induced modulation manifests a local action of the electric pump field on the single-molecule switch, confined to the ångström scale. Moreover, the contrasting patterns of $\bar{p}$ and p_{pp} manifest that the local force stimulus is independent of the local charging probability.

Impact of local vertical fields on molecular rotation. At first glance, the behavior of the molecular switch is surprising. The electric field of the near-field waveform is expected to be oriented predominantly perpendicular to the sample. This raises the question why such an electric field would modulate the switching probability, which is an in-plane rotation. The microscopic mechanism of this can be understood by employing density functional theory (DFT) (Fig. 4.6c). All DFT calculations discussed in this chapter have been performed by Nikolaj Moll. Exactly as in the experiment, the molecule is centered on top of a Cl^- site. To simulate the effect of the pump pulses, atomically strong electric fields are applied locally. This is implemented by a pair of vertically separated point charges (1.6 elementary charges) that enclose the molecule and salt layers. For different lateral positions of the point charges, the effect of the electric field on the molecule rotation is evaluated by relaxing the geometry of the combined system of molecule and NaCl layer. In particular, we observe whether the external local fields cause the molecule to rotate azimuthally. Even though this is a static simulation, the DFT calculations illustrate intuitively the microscopic mechanism of the local action of an applied electric field. The color map (orange) in Figure 4.6c depicts the angle of field-induced azimuthal rotation of the molecular frame for every position of the point charges. Clearly, the molecule rotates upon applying an electric field in specific areas, whereas fields applied elsewhere do not induce an appreciable rotation. The calculated rotations are too small to directly induce switching into the other adsorption geometry, consistent with the experimental observation that without electron injection no switching is observed. However, they are large enough to trigger an in-plane frustrated rotational motion that will modulate the switching probability of a later probe pulse and thereby allow for coherent control. Indeed, the simulated rotation pattern seems to be correlated with the experimentally observed modification of the switching probability by the pump pulse. The region, in which the pump pulses efficiently

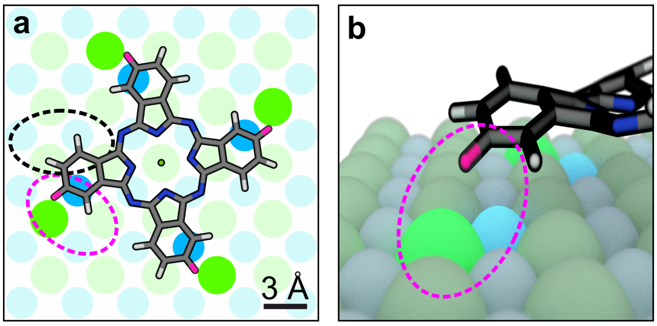

Figure 4.7 | Local molecule-substrate interaction. **a**, Top view of the calculated geometry of MgPC adsorbed on a Cl^- site in the underlying NaCl layer. No electric field is applied. **b**, Schematic side view of the adsorption geometry, where the z excursion of the calculated atomic positions in MgPc is exaggerated by a factor of 6. The calculated geometry indicates that the interaction of specific hydrogen atoms (pink) with the underlying chlorine atoms (intense green) and sodium atoms (intense blue) dominates the adsorption energetics of the molecular switch. Local fields applying forces close to these atoms induce the strongest molecular rotation and coherent dynamics (Fig. 4.6). The areas of strong (pink dashed line) and weak (**a**, black dashed line) modulation are marked corresponding to Fig. 4.6.

modulate the switching probability (Fig. 4.6c, D-F), also the field-induced rotation is locally enhanced (pink dashed line). In contrast, at positions of absent pump-induced modulations (Fig. 4.6c, A-C), the simulated molecular rotation vanishes (black dashed line). The experimental results together with the DFT calculations let us conclude that the switching probability is modulated locally by the electric field of the pump pulses, which induces a rotation of the molecular frame when locally applied to specific positions across the molecule.

Microscopic mechanism. The DFT calculations also suggest that the molecule's peculiar switching behavior comes from the specific arrangement of the NaCl substrate and key atoms within the molecule [Pel20]. The interaction of these specific atoms (highlighted in Fig. 4.7) is expected to dominate the energetics concerning the azimuthal orientation. In particular, specific hydrogen (pink) and chlorine atoms (green) in molecule and salt layer seem to be responsible for the double-well potential with minima at $\phi = \pm 10°$ with respect to the underlying salt lattice due to a polar interaction of these atoms. The isoindole units of the molecule even tilt towards the substrate leading to an inner distortion of the MgPc molecule (Fig. 4.7b). An electric field applied to the molecule is expected to impact the adsorption energetics of the molecule most strongly at these very hotspots of local polar interaction. This is consistent with the observation in theory and experiment that local fields applying forces close to these atoms induce the strongest molecular rotation and coherent dynamics.

Our approach of using the electric field of near-field waveforms as force pulses establishes a technique to locally manipulate select key atoms of polar binding partners on ultrafast time scales. The ultrafast coherent atomic manipulation demonstrated paves the way for path-selective real-space reaction microscopy with sub-cycle and atomic precision. Ultrafast structural transitions of a variety of quantum systems ranging from single molecules to solids can now be controlled on their natural time and length scales.

We found that the atomically confined electric field of terahertz transients act as ultrafast force pulses. The following question naturally arises: what do the atomically confined near-field waveforms look like? In the following chapter, I will elucidate quantitative sampling atom-scale near-field waveforms.

Chapter 5

Sampling atomically confined lightwaves

The results presented in this chapter have been measured and interpreted in close collaboration with Dominik Peller, Lukas Z. Kastner, Thomas Buchner, Alexander Neef, Johannes Hayes, Franco Bonafé, Dominik Sidler, Michael Ruggenthaler, Ángel Rubio, Rupert Huber and Jascha Repp, and were published in Nature Photonics [Pel21], where the authors' contribution is specified. The presentation of the results closely follows the publication with figures adapted from [Pel21] with permission.

In section 3.2, we introduced ultrafast action spectroscopy to explore the switching statistics of a single-molecule switch. Based on this development together with using the electric field of a terahertz pulse as an ultrafast force pulse (chapter 4), we are able to steer select key atoms in the molecular switch and thereby change its switching statistics on ultrafast time scales. In this chapter, we exploit the knowledge about the molecular switching statistics to quantitatively sample atomically confined near-field waveforms.

Confining light with tailored nanostructures has been a driving force of progress in enhanced catalytic activity [Chr12, Geo18], (bio)chemical sensing [Ank08], more efficient light harvesting [Bar03, Sch10b, Atw10] and the development of ultrafast microscopy techniques [Lei23]. When light interacts with nanostructures, a complex interplay of plasmonic propagation, near-field screening, geometrical phase retardation and antenna enhancement is responsible for the exact strength and temporal evolution of the oscillating electric near field. On top, non-classical ultrafast dynamics such as tunneling has been predicted to alter the local fields [Jes19]. All these effects make an a priori prediction of atomically confined waveforms, like in LW-STM (section 3.1), challenging. Whereas far-field transients coupled to the STM junction can be sampled via electro-optic detection [Kei90, Gal99, Hub00], quantitatively measuring ultrafast atomically confined near-field transients remained a key challenge for a long time. Since light–matter interaction in nanostructures depends on both strength and shape of the near-field waveform, a method to directly sample and calibrate the temporal evolution of atomically confined electric fields in a quantitative manner has been highly desirable. Employing photo-assisted tunneling of electrons via irradiation by optical pulses and modulation of the tunneling barrier by terahertz irradiation, the tip-confined waveforms could be mapped out on a microscopic scale [Yos19, Mü20]. However, quantitatively measuring the near-field waveform on atomic scales in a parameter-free fashion, has not been able with photo-assisted measurements. In the following, I will demonstrate, how we use ultrafast action spectroscopy to quantitatively measure the atomically confined near-field waveform in the atomic STM junction with a parameter-free method.

The electric field of a terahertz near-field transient coupled to the tunneling junction of an STM induces a transient bias voltage in the junction. In section 5.1, I explain our novel sampling scheme, which allows us to quantitatively measure the atomically confined near-field waveform of the terahertz transient calibrated in units of volts. With its access to amplitude and phase of the waveform, we can extract a transfer function from the far to near field allowing for future predictive design of nanooptics (section 5.2).

5.1 Quantitative sampling of atom-scale near-field waveforms

To quantitatively sample atomically confined waveforms, we employ LW-STM. The terahertz far-field transient is focused onto the tunnel junction (Fig. 5.1a), while the metallic tip is located only a few ångströms above the conductive sample. This arrangement acts as a terahertz antenna leading to strong field enhancement in the tunnel junction (Fig. 5.1b). The enhanced near-field waveform then acts as a bias

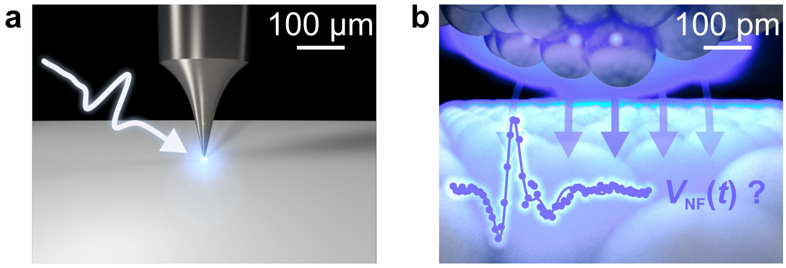

Figure 5.1 | Unknown near-field transient. **a**, A terahertz waveform is focused into the tunnel junction of an STM. Coupling to the strongly sub-wavelength volume in this geometry changes magnitude and shape of the terahertz transient drastically, making quantitative predictions at the atomic scale challenging (**b**).

voltage in the tunnel junction. While the exact atomic shape of the tip is unknown, it can alter the tip-confined fields [Bar15, Ben16] and also quantum effects could shape the near field on top of classical effects.

Sampling scheme. To measure a terahertz waveform on atomic scales, we establish an interference scheme directly on atomic scales. The test waveform to be sampled (Fig. 5.2a) is overlapped with a gate waveform (Fig. 5.2b), in this case another terahertz transient delayed by τ. Both transients individually induce an instantaneous voltage, $V_{\mathrm{NF}}(t)$ and $V_{\mathrm{gate}}(t-\tau)$, respectively. Importantly, the electric field amplitude of the gate pulse is much larger than the one of the sampled test waveform. Indeed, the peak electric field of the gate pulse is tuned such that it reaches a threshold of a strong tunneling onset, in this case through a molecular orbital (grey area). This ensures that the field crest of the gate pulse dominates tunneling in the STM junction. Varying the relative delay time τ, the instantaneous amplitude of the test transient offsets the field crest of the gate $V_{\mathrm{gate}}^{\mathrm{peak}}$ (Fig. 5.2c), such that the peak field of the superposition waveform $V_{\mathrm{sum}}^{\tau}(t)$ traces out the test waveform. Hence, if we can determine the local peak voltage of $V_{\mathrm{sum}}^{\tau}(t)$, we should be able to stroboscopically measure the time evolution of $V_{\mathrm{NF}}(t)$, which is the atomically confined near-field waveform in units of volts. For that, we employ a local voltage gauge.

Local voltage gauge. As discussed in section 4.1, the electric peak field in the junction can be calibrated to a local peak voltage by employing the single-molecule switch MgPc on NaCl introduced in section 3.2 as a local voltage gauge.

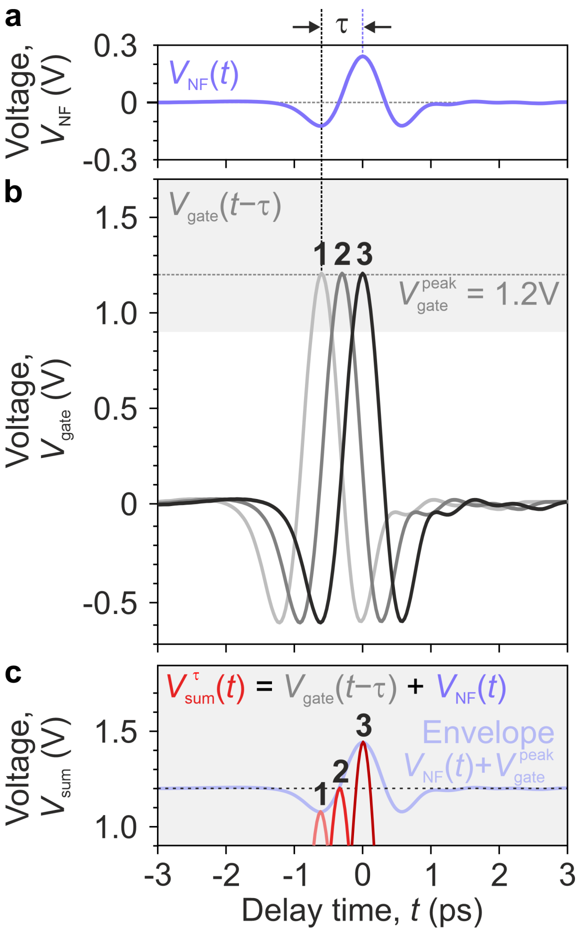

Figure 5.2 | Interference measurement scheme. **a**, A test waveform coupled to the STM junction induces an instantaneous voltage $V_{NF}(t)$. It is overlapped with a delayed probe transient (labeled 1, 2, and 3 for different delay times τ), whose peak electric field is tuned to a molecular resonance (**b**), such that its field crest dominates the action of $V_{gate}(t-\tau)$. **c**, When the two waveforms interfere, temporally separated by the delay time τ, $V_{NF}(t)$ offsets the crest of $V_{gate}(t-\tau)$ (red: superposition waveform $V_{sum}(V)$ for three different delay times labeled 1, 2 and 3). The peak field of the superposition waveform traces out the near-field waveform (envelope).

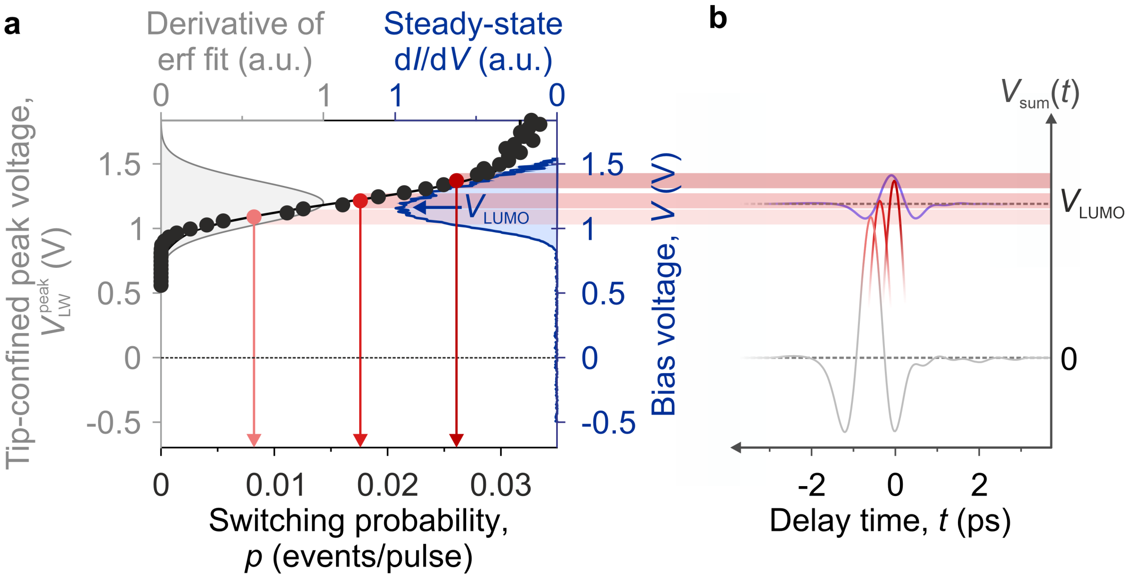

Figure 5.3 | Molecular switch as local voltage gauge. **a**, The switching probability of the molecular switch MgPc on NaCl changes as a function of the tip-confined peak voltage (black data points). The derivative (gray area) of an error function fit (black line) to the data points peaks at the voltage of the LUMO resonance seen in a steady-state spectrum (blue area). Around the LUMO resonance, the switching probability rises steeply allowing for a one-to-one translation between switching probability and tip-confined peak voltage. **b**, The voltage crest (red) of the interference waveform $V_{\mathrm{sum}}(t)$ is shown for three delay times between gate and test waveform (Fig. 5.2). The gate pulse and test waveform are attenuated such, that the peak voltage of the interference waveform (purple) traces out the test waveform and lies in the voltage region, where a switching probability can unambiguously assigned to a specific tip-confined voltage.

We know that the switching probability is directly proportional to the charging probability of the molecular switch and depends on the exact peak field in the junction. Indeed, it changes rapidly with increasing voltage around the LUMO resonance. For different tip-confined peak voltages, we can measure the switching probability p of the molecular switch via ultrafast action spectroscopy (Fig. 5.3a). Around the LUMO resonance, this calibration curve assigns one specific switching probability to a specific tip-confined peak voltage. The peak of the derivative of the calibration curve (gray area) can be assigned to the LUMO peak in conventional STS (blue area) as done in section 4.1, but even more, a range of field strengths

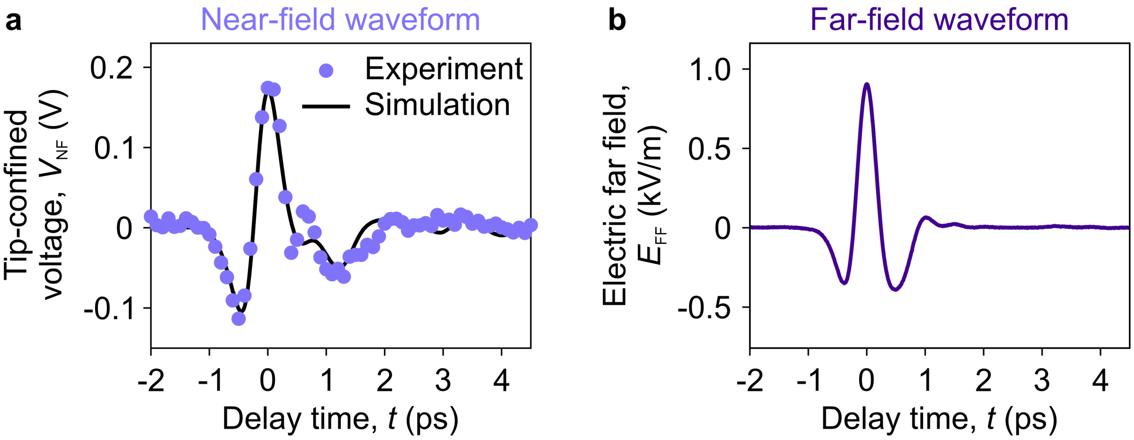

Figure 5.4 | Quantitatively measured near-field and far-field waveform. **a**, The near-field waveform (purple data points) is measured quantitatively in units of volts. Salient sub-cycle features are resolved and allow for a comparison with the far-field transient coupled into the tunnel junction detected using an electro-optic sampling scheme (**b**). The latter exhibits a cosine-like shape at higher frequency differing remarkably from the near-field waveform. Using the far-field waveform, the near-field transient can be simulated classically (**a**, black line) agreeing well with the measured waveform.

around the LUMO can be determined quantitatively in units of volts. By tuning the field crest of the gate waveform to the LUMO and strongly attenuating the test waveform, the peak voltage of the interference waveform (Fig. 5.3b) lies in the region of the calibration curve, where a tip-confined voltage can unequivocally be connected to a specific switching probability and the other way around.

Atomically confined near-field transients. Employing the explained interference measurement scheme (Fig. 5.2) with the single-molecule switch as a local voltage gauge, we can quantitatively determine the atomically confined near-field waveform directly in the tunnel junction in units of volts. Sweeping the delay time τ between test and gate waveform, we measure the switching probability for each delay time. The change in the switching probability as a function of τ is due to the change in the peak voltage of the interference waveform (Fig. 5.3), which traces out the test waveform (Fig. 5.2c). Hence, by measuring the delay-time dependent switching probability $p(\tau)$, we directly determine the tip-confined voltage transient of the test waveform in units of volts (Fig. 5.4a).

Salient features in the near-field waveform are resolved. Indeed, the measured waveform differs considerably from the electro-optically sampled far-field waveform (Fig. 5.4b). The tip-confined transient is longer, seems to possess a different carrier-envelope phase and a lower center frequency. The latter qualities, however, are generally more accessible in a spectral analysis, in the frequency domain.
To better understand the transfer from the far field to the near field, we compare the spectra of the two waveforms.

5.2 Transfer from the far field to the near field

In the last section, we have seen how it is possible to quantitatively measure atomically confined waveforms directly in the junction of an STM. Based on this achievement, we want to determine, whether we can predict the near-field waveform after measuring a far-field transient. For this purpose, we compare the near-field and far-field waveforms in the frequency domain instead of their temporal evolution by calculating their Fourier transform.

Spectral analysis of far-field and near-field waveforms. We obtain the spectrum, $E(f)$, via a Fourier transform $E(f) = \mathcal{F}\{E(t)\}(f)$, where $\mathcal{F}\{f(x)\}(y) \propto \int f(x)e^{-2\pi ixy}\mathrm{d}x$. The amplitude of this quantity and the angle between real and imaginary part correspond to the spectral amplitude and phase, respectively. The far-field transient yields a spectral amplitude centered at 0.9 THz (Fig. 5.5a) and a flat phase of $\sim$0 rad (Fig. 5.5b). In contrast, the near-field spectrum peaks at lower frequencies around 0.5 THz and is slightly structured with subtle oscillations in the spectral amplitude (Fig. 5.5c). Also the spectral phase (Fig. 5.5d) exhibits such an oscillatory structure. Otherwise, the spectral phase is flat at $\sim-\pi/3$. From these curves, the spectral amplitude and phase, which are measured in far and near field, we can extract a transfer function, which translates the spectrum of the waveform coupled to the STM junction to the spectrum of the atomically confined near-field transient.

Transfer function. We identify a transfer function from far to near field for both spectral amplitude and phase. The near-field waveform is measured in units of volts

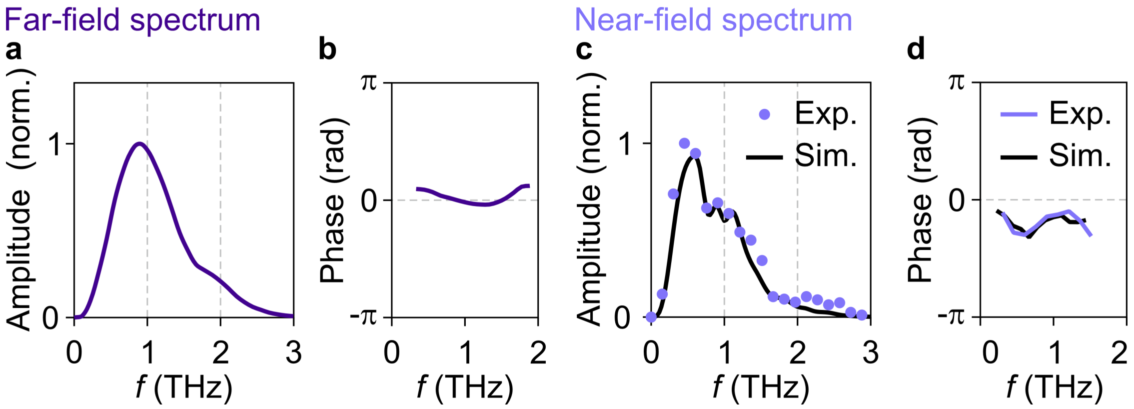

Figure 5.5 | Spectral amplitude and phase of far-field and near-field transient. The spectral amplitudes (**a**,**c**) and phases (**b**,**d**) are extracted from the measurements (Fig. 5.4) in the far field (**a**,**b**) and near field (**c**,**d**). The far-field spectrum is centered around 0.9 THz and possesses a flat phase of ~0 rad. In the near field, the spectral amplitude is shifted towards lower frequencies, peaking at around 0.5 THz. A subtle oscillation modulates spectral amplitude and phase. The baseline of the oscillation in the spectral phase lies at around $-\pi/3$ rad. The near-field spectral entities (**c**,**d**) are overlayed with a classical simulation (black lines), which estimates the near-field spectral response from the far-field data (**a**,**b**).

rather than volts per meter. Classical antenna theory predicts a field enhancement inversely proportional to the tip-sample distance d ($E_{\mathrm{NF}} \propto 1/d$) [Kan09]. In this regime, the voltage dropping across the STM junction is proportional to the electric near field ($V_{\mathrm{NF}} = E_{\mathrm{NF}} \cdot d$) such that the measured voltage does not depend on the absolute tip height. For a direct comparison of near-field and far-field measurements, however, we estimate a tip-sample distance d of about ~10 Å [Pel20], such that the electric field $E_{\mathrm{NF}}(t) = V_{\mathrm{NF}}(t)/d$ and its spectrum can be calculated. To extract a transfer function from the far to the near field from experimental data, we divide near-field and far-field spectral amplitude and subtract the respective phases for each sampled frequency (Fig. 5.6a). The extracted transfer function yields a field enhancement (purple data points) following a $1/f$-behavior. At 1 THz, the electric field amplitude is enhanced by a considerable factor of about 2×10^5 due to the extremely sub-wavelength confinement. The oscillatory behavior seen in the near-field spectral amplitude and phase is reproduced by the transfer function. To understand, which parts of the transfer function can be explained by classical electrodynamics,

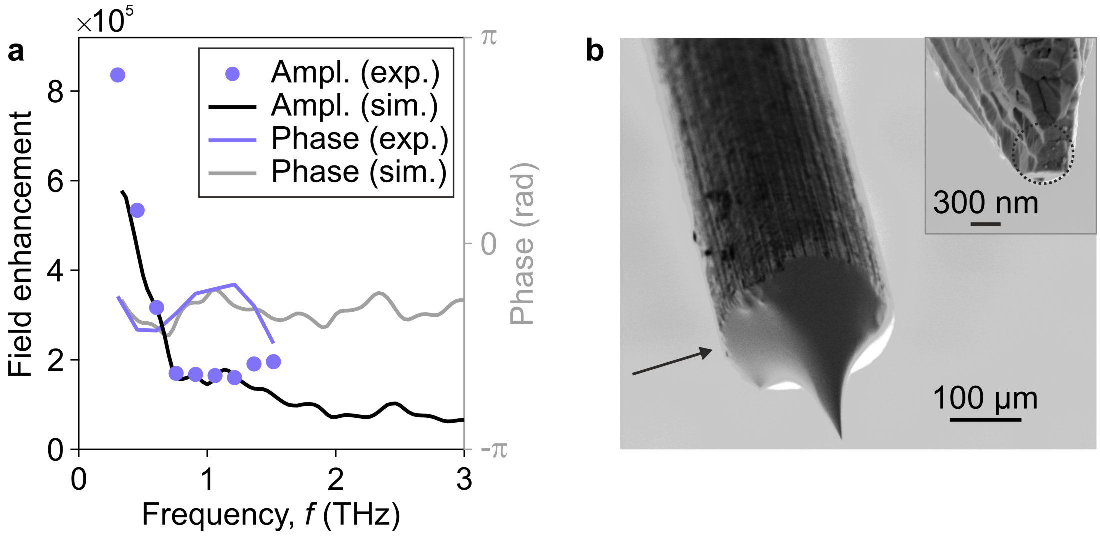

Figure 5.6 | Transfer function from far field to near field. **a**, From the spectral amplitude and phase measured in the far field and near field (Fig. 5.5), a complex valued transfer function can be extracted. Assuming a locally homogeneous electric field across a tip-sample distance of 10 Å yields a field enhancement (purple data points) from far to near field following a $1/f$-like behavior. The carrier envelope phase (purple line) shifts by $\sim -\pi/3$ rad. The transfer function determined experimentally is overlayed with the transfer function calculated in a classical electrodynamic simulation for the tip-sample geometry in place. In the classical simulation, the macroscopic tip geometry is imitated from electron microscope images (**b**). The tip consists of a cylindrical tungsten wire, which is etched on one side, yielding a tapered region with a height of about 200 μm (upper end marked by arrow). A zoom to the tip apex (top right) reveals a 300 nm radius of curvature.

we simulate the field propagation from far field to near field by solving Maxwell's equations utilizing the finite-element method.

Classical simulation of transfer from far to near field. With the frequency-domain finite element solver COMSOL, a transfer function based on classical electrodynamics was calculated [Nee18, Pel21]. Plasmonic coupling to the tip shaft, screening and localization in the tunnel junction are included in the simulation by introducing the respective material properties (gold sample and tungsten tip) and junction geometry used in the experiment. The classical simulation is based on the measured tip geometry (Fig. 5.6b) and the sample is located 10 Å below the tip. For a range of frequencies, the propagation into the near field is calculated for the described tip-sample geometry as well as for bare vacuum. Comparing the complex electric field of both simulations allows for extracting the complex-valued transfer function shown in Fig. 5.6a (black and gray lines). Applying this transfer function to the measured far-field spectral amplitude and phase yields the simulated spectral amplitude and phase shown in Fig. 5.5c,d (black lines). With the help of an inverse Fourier transform, the classically expected near-field waveform can be obtained (Fig. 5.4a, black line). Indeed, the calculated transfer function reproduces the experimental data quite accurately. Even the oscillatory structure in the spectrum is matched and can be identified as standing waves caused by an edge on the tip, which stems from the etching process used to fabricate the tip (Fig. 5.6b, arrow). Our measurements together with the classical simulation open the door to predict and even design nano-optics in the near-field regime.

In the previous two sections, we have developed a way to quantitatively measure atomically confined waveforms. An extracted transfer function from the far field to the near field prepares the ground for predictive design of nano-optics. With our technique to measure atomically confined near-field waveforms, we do not only calibrate the peak voltage induced within the junction, but we establish a method to quantitatively measure the whole voltage transient induced in the ångström-scale tunnel junction. In particular, we detect a range of voltages paving the way for measurements of the ultrafast LDOS on atomic length scales. Indeed, it has been a long-standing desire to capture the instantaneous LDOS on ultrafast timescales to follow the evolution of electronic energy levels upon excitation. The developments of LW-STM presented in the former chapters lay the ground for this next big milestone by providing access to both structural motion and select electronic energy levels. Yet, energy resolution is needed additionally to temporal and spatial precision. In the next chapter, I will present ultrafast scanning tunneling spectroscopy on atomic scales allowing for simultaneous sub-picosecond, atomic and millielectronvolt resolution.

Chapter 6

Measuring and manipulating the ultrafast local density of states of an atomic defect

> *When opportunity presents itself grab it.*
> *Hold on tight and don't let go.*
>
> — Rie y Llora, Celia Cruz

The results presented in this chapter have been measured and interpreted in close collaboration with Lukas Z. Kastner, Maximilian Graml, Andreas Biereder, Jan Wilhelm, Jascha Repp, Rupert Huber and Yaroslav A. Gerasimenko. The main part of the topics covered in this chapter was published in Nature Photonics [Roe24], where the authors' contribution is specified. The presentation of the results is adapted from the publication with permission. Section 6.1 covers steps of sample development not included in [Roe24]. The sample development was inspired by input from Tobias Preis and Marlene Liebich. TP provided valuable input on Au(111)/mica samples as well as suitable STM sample-holder designs. CR, ML and YAG promoted the progress of TMDC monolayer stamping on Au(111) and on hBN/Au(111). CR and YAG worked on STM-suitable hBN/Au(111) coverage for WSe_2 *stamping.*

Defects in atomically thin semiconductors and their moiré heterostructures have emerged as a unique testbed for quantum science. Strong light–matter coupling, large spin–orbit interaction and enhanced Coulomb correlations facilitate a spin–photon interface for future qubit operations and efficient single-photon quantum emitters. Yet, directly observing the interplay of the electronic structure of a single defect with other microscopic elementary excitations on their intrinsic length, time and energy scales remained a long-held dream.

In this chapter, I explain how we investigate the evolution of the electronic structure of an isolated atomic defect in a monolayer transition metal dichalcogenide (TMDC) under controlled excitation of a phonon. To achieve this goal, atomic spatial, ultrafast temporal and ∼meV energy resolution need to be combined simultaneously, which has remained an ambitious vision until now. LW-STM allows for ultrafast temporal and spatial resolution together with control over structural motion (chapters 3-5). By establishing ultrafast lightwave-driven scanning tunneling spectroscopy (LW-STS), we can additionally access a part of the transient LDOS (sections 6.2-6.4) and observe its temporal evolution upon excitation of structural motion (sections 6.5-6.6). This breakthrough enables us to directly resolve how a select energy level of an atomic vacancy in tungsten diselenide (WSe_2) transiently shifts under controlled excitation of structural motion. We observe a transient shift of up to 40 meV calling for a thorough investigation of interacting electronic energy levels with structural motion in the defected monolayer (section 6.7). In the following section, I will introduce TMDCs and a fabrication method of atomically flat and clean WSe_2 monolayers suitable for STM investigation of isolated vacancies with atomic resolution (section 6.1).

6.1 Transition metal dichalcogenide monolayers with atomic defects

Layered semiconducting TMDCs have revolutionized solid state physics due to their unusual excitonic properties [Wan18, Nai22], strong spin-orbit coupling [Man15] and the possibility to tailor band structures. A bulk TMDC crystal consists of many atomically thin layers weakly bound to each other by van der Waals interaction (Fig. 6.1a), whereas whithin the monolayers, the atoms are covalently bound (Fig. 6.1a,b). In each monolayer, a layer of transition metal atoms is sandwiched between two close-packed layers of hexagonally arranged chalcogen atoms. The transition metal atoms are covalently bound to the closest chalcogen atoms above and below (Fig. 6.1a).

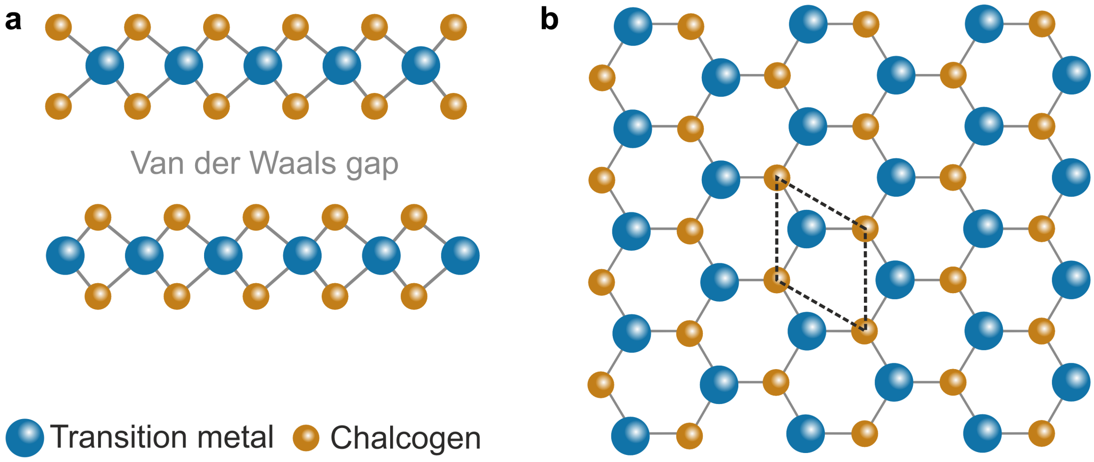

Figure 6.1 | Atomic structure of TMDCs. **a**, TMDC crystals consist of monolayers weakly bound to each other by van der Waals interaction (side view of two layers in the orthorombic polymorph (2H) structure). Within a monolayer, transition metal and chalcogen atoms are covalently bound to each other. **b**, Top view onto an individual monolayer: the atoms in the monolayer crystal form a hexagonal structure (unit cell: dashed line).

TMDC monolayers and their heterostructures. Due to the relatively weak van der Waals interaction between the different layers, individual monolayers can be peeled off a bulk crystal, e.g. by cleaving the crystal with scotch tape. When a bulk semiconductor TMDC crystal is thinned down to the monolayer limit, the band structure typically transitions from an indirect to a direct band gap semiconductor. This property together with large spin-orbit coupling and strong light-matter interaction renders these materials interesting candidates for optoelectronics and valleytronics [Xu14]. The term “valley” is used to describe the extrema in the band structure in momentum space. Due to the presence of large spin-orbit coupling [Man15], both valence and conduction band are spin-split. In particular, the order of spin-split bands is inverted at the edges of the Brillouin zone K and K’, where the direct band gap is located in momentum space. This allows for valley-specific manipulation and readout, which has been proposed for information storage [Xu14]. When an electron is promoted from the valence band maximum to the conduction band minimum at K/K’ with a photon, only transitions between bands with the same spin are allowed yielding valley-specific optical selection rules.

The elementary excitation playing a key role in the optoelectronic phenomena in TMDC monolayers is the generation of excitons. Strong attractive Coulomb interaction in TMDC monolayers gives rise to excitons, hydrogen-like bound electron-hole pairs, with typical binding energies of several hundred millielectronvolts [Poe15, Wan18].

Concluding, the unusual excitonic properties, valley selectivity and strong spin-orbit coupling render TMDC monolayers highly interesting. Meanwhile, the toolbox to tailor properties gets even larger when combining different monolayers and stacking them at will.

Exploiting the attractive interaction between individual layers of van der Waals materials, monolayers can be stacked on top of each other [Gei13]. Thereby, monolayer crystals with incommensurate lattices can be coupled with arbitrary mutual rotation. Additional tuning knobs are gating and straining of the heterostructures. As a result, band structures can be custom-tailored allowing for the observation of a variety of novel states of matter [And21] like correlated and topologically non-trivial states [Mak22] and heterostructures hosting moiré excitons [Kar22, Sch22]. Correlated insulating states could be observed at fractional fillings of WSe_2/WS_2 moiré superlattices [Xu20]. When the charge carrier density in TMDC heterostructures is tuned accordingly, electrons can localize in a periodic lattice forming a Wigner crystal [Zho21, Li24]. Moreover, moiré heterostructures have been proposed as condensed-matter quantum simulator [Ken21]. For all these emergent phenomena and perspectives, specific states or the band structure are tuned. In TMDC heterostructures, excitons and other optical excitations play a crucial role for their opto-electronic properties building corner stones of opto-electronic devices. Meanwhile, their lifetimes are limited to ultrashort timescales [Mer19]. To understand the mechanisms underlying the astonishing phenomena arising in van der Waals heterostructures, it is beneficial to investigate the band structure of these materials, ideally directly in time to follow their evolution.

Accessing the band structure of TMDCs. Angle-resolved photoemission spectroscopy (ARPES) and momentum microscopy allow for direct mapping of the band structure of surfaces, i.e. also surface states and 2D materials, in momentum space. In particular, their development towards capturing the band structure in a time-resolved fashion has helped to understand fundamental principles such as intraband currents [Rei18], the build-up of Floquet bands [Ito23] and materials like TMDCs [Wal21b, Kar22, Sch22]. Similar to Bloch electrons in crystals featuring a periodic band structure in momentum space, a periodic potential in time, i.e. light as an oscillating wave with frequency Ω, generates replica of the band structure shifted in energy by $\hbar\Omega$, called Floquet-Bloch bands. The build up and dephasing of Floquet-Bloch bands on sub-cycle timescales has been observed for topological surface states in Bi_2Te_3 [Ito23]. From a material perspective, the understanding of TMDC heterostructures [Kar22, Sch22] and monolayers [Wal21b, Par24] has been enhanced immensely with the help of time-resolved ARPES and momentum microscopy. Localized features such as moiré excitons with electron and hole located in different layers [Kar22, Sch22] and even molecular orbitals [Wal21a] have been observed in momentum space with ultrafast temporal resolution via time-resolved μ-ARPES [Kar22] and photoemission momentum microscopy [Wal21a, Sch22]. However, even in momentum microscopy, which allows for the investigation of atom-scale features, the real-space charge localization and distribution can only be reconstructed as a spatial average from momentum-resolved maps of periodic samples. Meanwhile, atomic defects in TMDCs offer exciting perspectives.

Atomic defects. Atomic defects in TMDC monolayers [Hon15] and heterostructures [Guo21] are not only ubiquitous, but have also sparked enormous interest due to the opportunities they offer. In particular, chalcogen vacancies (Fig. 6.2) in TMDC monolayers are known as exciton traps [RA18] and single-photon emitters [He15, Sri15, Ton15, Cha15, Kle19] – building blocks for future quantum information devices [O'B09] – and as catalysts for hydrogen extraction [Li15]. They feature localized in-gap defect states [Sch19, Bob24b], which can strongly influence the optical and electronic properties of the monolayer. Combining defected TMDC monolayers with a substrate hosting spin qubits, where a chalcogen vacancy is placed on top of the qubit, could build a spin-photon interface allowing for optical read-out of the nuclear-spin qubit in the underlying solid [Ata18, Wol21]. The coherence of such quantum emitters and quantum bit complexes is limited by the interaction with their environment [Bec15, Sto16]. For instance, atomic vibrations can shift energy levels of these quantum systems. Understanding the key microscopic mechanisms

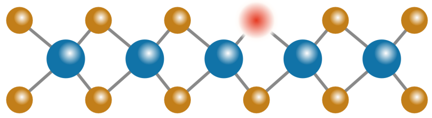

Figure 6.2 | Chalcogen vacancy. Among other defects in TMDC monolayers, chalcogen vacancies can occur, e.g. in the upper layer of chalcogen atoms (red dot).

of these interactions and decoherence requires a fundamentally new technique with exceptional spatial, temporal and energy resolution to follow the evolution of specific energy levels directly in time. In sections 6.2-6.7, I will present ultrafast LW-STS, which complements techniques like time-resolved momentum microscopy with actual atomic precision in real space allowing for the investigation of select atomic defects, isolated chalcogen vacancies, in a TMDC monolayer. Our technique is based on LW-STM and poses specific challenges on the sample quality.

Sample requirements. For LW-STM and LW-STS, we need atomically flat samples, which are compatible with ultrahigh-vacuum measurements. In particular, the TMDC monolayers should be clean on the atomic scale and chalcogen vacancies should be present. Working with semiconductors in low-temperature STM presents a significant challenge, since we detect the tunnel current between tip and sample electrode and hence, a conductive sample is necessary for LW-STM experiments. Few-layer samples on top of a metallic substrate fulfill this requirement. Furthermore, a limited view into the STM chamber renders finding ~(10 µm)^2-sized few-layer TMDC samples with the tip demanding. Capacitive techniques have been suggested to address this issue [Li11], but they require a special substrate design, which is often challenging for sensitive materials like TMDC monolayers. This is why TMDC samples, which are uniform over a large area are desired, ideally on the order of ~mm^2. Moreover, a purely metallic area to shape the tip is beneficial. Usually, to form a sharp tip apex, the tip is dipped into a crystalline metal surface with a tip approach on the order of nanometers while applying a voltage pulse. Concluding, we aim at extremely large, uniform, atomically clean and flat monolayer or few-layer TMDC samples on a conductive substrate with additional sufficiently thick crystalline metal areas for tip shaping. Due to all these specific demands, an adapted fabrication method is required.

Gold-assisted exfoliation. Conventionally, relatively large-area TMDC few-layer samples are acquired via visco-elastic PDMS exfoliation [CG14]. With scotch tape, TMDC is stamped onto the polymer film and then thinned down to the thickness of choice. Afterwards, this sample is stamped onto a substrate for measurement. We found that such samples are not suitable for STM, since insulating residues of PDMS hinder measuring tunnel currents even after annealing procedures. In contrast, without any polymer treatment, large-area monolayers can be obtained via gold-assisted exfoliation. From [Vel18], it is known that TMDC monolayers can peel off a TMDC crystal when stamped directly onto gold due to the strong van der Waals interaction between TMDC monolayer and gold. This procedure works only for atomically flat, uncontaminated gold surfaces. In the work by Velicky *et al.* [Vel18], this precondition is met by depositing a very thin layer of gold onto a SiO_2/Si wafer and stamping TMDC onto the surface directly after gold deposition. We adapt this method to our specific demands in STM.

To provide an atomically flat gold area usable for regular tip preparation, we deposit a thicker gold layer of about 300 nm onto a clean and flat mica crystal. Whereas gold tends to form a crystalline (111)-oriented film on mica [DeR91], deposition onto unheated mica leads to grained surfaces rather than atomically flat areas. This is why we sputter and anneal the gold surface in ultrahigh vacuum like usually done for single-crystal metal samples yielding an atomically flat Au(111) surface with a herringbone reconstruction. With this procedure we ensure a conductive atomically flat substrate with the opportunity to shape the tip. Directly after several sputter and anneal cycles, we stamp freshly cleaved WSe_2 onto the Au(111) surface in nitrogen atmosphere to prevent contamination in air, especially by water and oxygen [Qiu12]. With this polymer-free procedure, we obtain very clean large-area monolayer TMDC as evidenced by optical-microscope images (Fig. 6.3a).

In the future, we would like to decouple the monolayer electronically from the gold substrate to enhance the lifetime of charge carriers. This might facilitate the observation of excitons and their decay. To preserve the advantages of gold exfoliation, we try to implement decoupling layers between the gold surface and the WSe_2 monolayer. When employing gold-assisted monolayer exfoliation, we found that small protrusions or impurities on the gold surface do not break the uniform WSe_2 layer. In contrast, higher or spatially extended protrusions lead to a hole in the monolayer. This is

Figure 6.3 | Gold-assisted exfoliation of WSe_2 monolayer. Optical-microscope images evidence successful stamping of WSe_2 monolayers with $\sim mm^2$ expansion. **a**, WSe_2 is exfoliated directly onto Au(111) [Vel18]. **b**, When hBN flakes are spread on Au(111) [Col11] and a monolayer WSe_2 is stamped on top, the monolayer partly covers the hBN flakes on Au(111) and is decoupled electronically (circles).

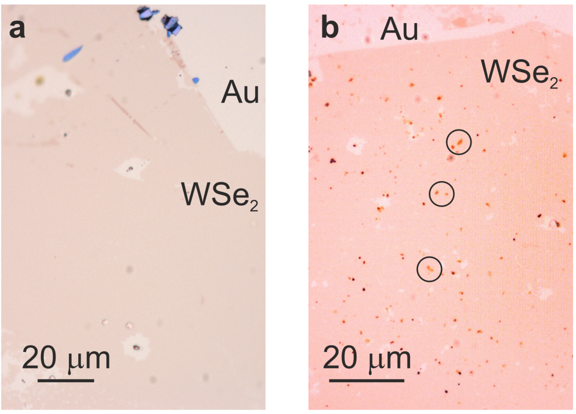

why we pursue the idea to insert thin and small decoupling layers of hexagonal boron nitride (hBN) between gold and WSe_2 with a coverage small enough such that stamping TMDC is still successful. At the same time, as discussed above, the limited view into the STM chamber hinders finding individual <10 µm flakes. Hence, the coverage of hBN on gold should be large enough such that the probability to position the STM tip on TMDC monolayer on top of hBN is appreciable.

To this end, we make use of liquid exfoliation [Col11]. BN powder (Sigma-Aldrich, 1 µm particle size, 98% purity) was dissolved in isopropanol and sonicated. To separate individual flakes by mass, the dispersion was centrifuged. More specifically, the powder (10 ml cylindrical vial with a starting concentration of 1 mg/ml) was sonicated for one hour. At 500 rotations per minute, the dispersion was centrifuged for 90 minutes (see supplementary material in [Col11]). In contrast to Coleman *et al.* [Col11], we collect lower parts of the supernatant with a pipette to obtain a higher concentration of hBN flakes. This suspension is distributed on the sputtered and annealed gold surface with a spin coater.

Subsequently, TMDC is exfoliated on the Au(111)/hBN substrate. However, TMDC monolayers do not stick to the gold surface, with or without hBN deposition, after extended exposure to air [Vel18]. To facilitate TMDC exfoliation, we flame anneal the sample. Alternatively, the sample can also be annealed in ultrahigh vacuum. Afterwards, WSe_2 is stamped directly onto the substrate. Indeed, this procedure yields monolayer WSe_2 decoupled from the gold substrate by hBN flakes (Fig. 6.3b). Clearly, hBN flakes of different thickness (color) and sizes are present on the sample. At some locations, high protrusions of hBN flakes hinder efficient WSe_2 stamping,

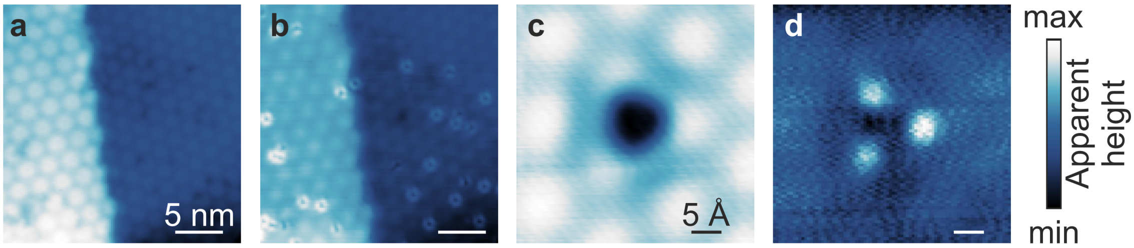

Figure 6.4 | Exfoliated WSe$_2$ monolayer in STM. Constant-current topography images of a home-stamped monolayer WSe$_2$ on Au(111) at $V = 1.2$ V (**a**, $I = 5.2$ pA) and $V = 0.5$ V (**b**, $I = 2.6$ pA) reveal a moiré pattern with defects in the pristine monolayer (scale bar: 5 nm). Different moiré orientation and periods occur in the left and right parts of the images (**a**,**b**) separated by an atomic step of gold. Zooming to one specific defect, it appears as a void when the voltage is tuned to the conduction band (**c**, $V = 1$ V, $I = 10$ pA) and exhibits a three-fold symmetric orbital density at lower voltages (**d**, $V = 0.5$ V, $I = 1$ pA, scale bar: 5 Å).

however in most areas, thin layers electronically decouple WSe$_2$ from the substrate (circles).

After stamping TMDC onto Au or hBN/Au, we anneal the sample at ~350 °C for several hours in ultrahigh vacuum in the preparation chamber of the microscope to get rid of remaining contamination on the sample and for defect generation [Ton13]. This procedure is continued until the pressure in the chamber stays on the order of 10^{-9} mbar. An alternative technique to generate defects, in a controlled fashion, is helium-ion bombardment [Kle19]. After the final sample fabrication step of defect generation, the sample is transferred into the cryogenic STM chamber.

We found that the WSe$_2$ on hBN/Au samples are in principle compatible with STM and electronically decoupled TMDC monolayers can be found on the sample. However, due to the varying thickness and area of individual hBN flakes, the local sample structure at the position of the tip is unknown. This constraint is not ideal for the interpretation of time-resolved data since the properties of tunnel barrier thickness and also lateral charge transport within the monolayer can shape the dynamical response of the sample while being unidentified. This is why we choose single-layer WSe$_2$ directly stamped on Au(111) as our sample for lightwave-driven STM and STS measurements.

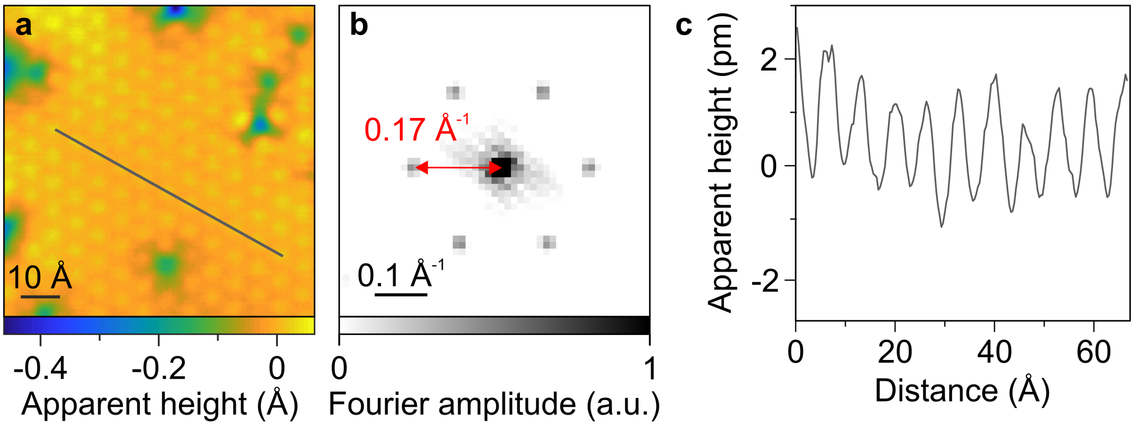

Figure 6.5 | Moiré pattern of home-fabricated monolayer WSe$_2$ on Au(111). **a**, A constant current image ($V = 1.12$ V, $I = 47.5$ pA) and its Fourier transform (**b**) yield a moiré period of ~6 Å. **c**, The induced modulation of the apparent height (profile along line marked in **a**) amounts to only a few picometers.

Atom-scale access to exfoliated monolayers. The home-stamped samples are flat and clean enough for STM measurements on the ångström scale. Examining the WSe$_2$/Au(111) sample structure in STM (Fig. 6.4), we find a moiré pattern arising from rotation and lattice mismatch between TMDC monolayer and Au(111) surface. On a large scale, irregularities in the gold structure on top of mica can lead to different twisting angles between the two crystal structures. These yield moiré patterns of different periodicity (Fig. 6.4a,b). More prominently, however, the appearance of the monolayer changes drastically with the applied bias voltage. Whereas at voltages reaching the conduction band of the monolayer, the moiré pattern is most obvious in the STM image (Fig. 6.4a), defects dominate the appearance of the surface at lower bias (Fig. 6.4b). Zooming to one defect, it emerges as a void at 1 V bias (Fig. 6.4c). Meanwhile, at 0.5 V, the STM image exhibits a three-fold symmetric structure (Fig. 6.4d). This kind of defect can be identified as an atomic chalcogen vacancy, in this case in the bottom layer of selenium (Se) atoms, with spin-orbit-split energy levels within the band gap featuring a characteristic three-fold symmetry of the orbital density [Sch19]. The in-gap states of the Se vacancy are dominated by the d states of the surrounding transition metal atoms. Due to the large spin-orbit coupling, also the defect states are split into a $J = 3/2$ and a $J = 5/2$ state, where J labels the total angular momentum of the electronic wavefunctions

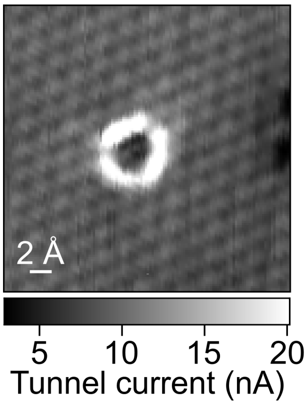

Figure 6.6 | Atomic resolution of defect state. In an atomically resolving constant-height image of a chalcogen vacancy in a monolayer WSe_2 stamped onto Au(111) (V =600 mV, height setpoint: I = 49 pA, V = 0.36 V), the orbital density of the lower-energy state of the missing Se atom is visible only in a locally confined area around the vacancy.

dominantly contributing to the orbitals of the missing atom [Sch19]. For simplicity, the orbital density in STM scans will be referred to as orbital of the chalcogen vacancy in the following.
In LW-STS, we want to resolve the transient electronic structure of these chalcogen vacancies in the WSe_2 monolayer and their evolution upon excitation of structural motion. The sample used for that yields a moiré periodicity of about 6 Å (Fig. 6.5a,b) with a height modulation apparent in STM images of only a few picometers (Fig. 6.5c). On this very sample, we can atomically resolve the lower-energy in-gap orbital of the Se vacancy demonstrating the localization of the defect orbitals on the atoms around the vacancy (Fig. 6.6). Since the resolution of LW-STM is expected to be at least as good as in time-averaged STM [Coc16, Amm21], the measurement shown in Fig. 6.6 sets the stage for time-resolved experiments of chalcogen vacancies on atomic scales.

Concluding, we found a way to fabricate large-area monolayer TMDC on Au(111) suitable for low-temperature STM measurements in ultrahigh vacuum. The home-fabricated samples host chalcogen vacancies within a moiré pattern and allow for atomic-scale resolution of locally confined orbitals in STM. With that, we have set the stage for LW-STM investigation. In the following sections, we develop a method to detect the transient LDOS in time, which complements techniques like time-resolved momentum microscopy with direct real-space instead of momentum-space access.

6.2 Lightwave-driven scanning tunneling spectroscopy

Defects in few-layer TMDC have been shown to shape optical and electronic properties (section 6.1). In particular, they were suggested as exciton traps [RA18] or spin-photon interfaces for qubits [Ata18]. The large susceptibility to external stimuli results in a strong variability in the defects' properties within a monolayer, thus local probes are required to study them individually.

Hitherto, steady-state experiments have resolved distinct energy [Hon15], spin [Coc21] and orbital [Sch19] structures of individual defects. However, an in-situ understanding of their dynamical interaction with the environment has been out of reach. The direct measurement of how atomic motion with a given amplitude changes the energy levels in a single defect would not only allow disentangling the complex interactions but also open possibilities for ultrafast dynamical control of quantum properties by driving specific phonons. Inducing, observing and understanding such dynamics requires a counterpart of time-resolved ARPES such that electronic energy levels can be probed on ultrafast timescales, yet with direct atomic spatial instead of momentum resolution. On the nanoscale, ultrafast near-field microscopy [Pla21] and nanoscale coherent phonon spectroscopy [Liu22] have enabled tracking ultrafast charge and lattice dynamics. Mapping molecular levels and vibrational states with ångström precision has been achieved by combining STM with photoluminescence [Yan20] or Raman scattering [Lee19], where light is strongly confined to atomically sharp metallic tips, in time-integrated studies. LW-STM (chapter 3.1) has combined both femtosecond temporal resolution and atomic spatial precision. However, meeting simultaneously the requirements of spatial, temporal and energy resolution in a single technique has proven extremely challenging [Lei23].

In this section, I will introduce LW-STS. With its atomic spatial resolution (section 6.1), energy resolution (section 6.3) and ultrafast temporal precision (section 6.4), we are able to excite structural motion (section 6.5) and to simultaneously follow the dynamical evolution of the LDOS of a chalcogen vacancy in a semiconducting monolayer WSe_2 (section 6.6). To establish LW-STS on a Se vacancy, we first investigate the vacancy in steady-state STS.

Steady-state STS of a chalcogen vacancy. Within the 6 Å-periodic moiré pattern formed by monolayer WSe_2 on Au(111), a Se vacancy in the top chalcogen layer can be found (Fig. 6.7a). On an orbital lobe (green cross) and pristine monolayer (gray cross), conventional tunneling spectra (green and gray curves in Fig. 6.7b) confirm the semiconducting nature of the monolayer and reveal the spin-orbit-split defect levels within the band gap (dashed lines). Conduction and valence band edges are positioned at around 1.1 V and −1.5 V. The absolute conduction band minimum is commonly associated with a tail around 800 mV [Zha15, Fee20], whereas the finite density of states in the gap relates to coupling between the semiconducting monolayer and the gold surface [Sø14]. The two defect levels, D_1 and D_2, within the band gap appear at 270 mV and 500 mV, well separated from the band edges (inset: schematic band diagram), and exhibit the characteristic three-fold (C_3-symmetric) orbital structure [Sch19] (Fig. 6.7a).

State-selective LW-STS. We would like to measure an ultrafast analogue of conventional tunneling spectra to retrieve ultrafast time-resolved snapshots of the LDOS. To this end, we couple terahertz pulses into the junction (Fig. 6.7c). Their near-field waveform acts as an ultrafast bias voltage (Fig. 6.7b, purple traces) and replaces the static voltage used in conventional STS. In LW-STM, the peak amplitude, $E_{\mathrm{LW}}^{\mathrm{peak}}$, is typically kept constant, while the tip position is scanning the surface and thereby orbital densities can be mapped in real space. In contrast, for ultrafast LW-STS, we systematically sweep $E_{\mathrm{LW}}^{\mathrm{peak}}$ through the band structure (purple traces). The idea is to measure the lightwave-induced current, I_{LW}, for each peak field reaching a different part of the band structure. A similar approach of sweeping the terahertz field and recording the rectified current has been shown to enable numerical reconstruction of the LDOS in graphene nanoribbons [Amm21]. Indeed, measuring a mixture of states in the rectified current requires models to extract ultrafast tunneling spectra and to interpret the data [Amm22]. In our experiments, we build on a solely data-driven extraction of ultrafast tunneling spectra instead by operating in the state-selective regime of LW-STM (section 3.1). In general, the near-field waveform acts as an ultrafast voltage pulse $\mathcal{V}_{\mathrm{LW}}(t)$ as a whole (waveforms in Fig. 6.7b) such that the instantaneous tunneling current $\mathcal{J}_{\mathrm{LW}}(t)$ is generated by a broad range of voltages up to $V_{\mathrm{LW}}^{\mathrm{peak}}$, the voltage generated by the peak electric

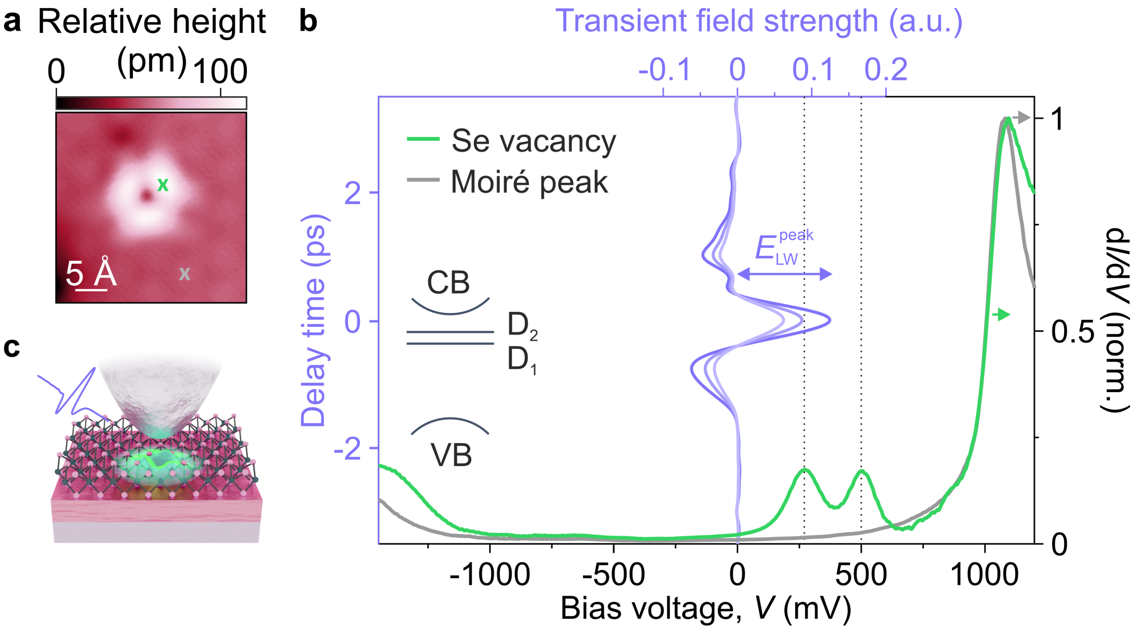

Figure 6.7 | Concept of lightwave-driven scanning tunneling spectroscopy. **a**, A constant-current STM image (V = 380 mV, I = 49 pA) of a Se vacancy in a monolayer WSe_2 on Au(111) exhibits the three-fold symmetric orbital of the vacancy on top of a 6 Å moiré pattern of monolayer WSe_2 on Au(111) (Fig. 6.5). **b**, Steady-state scanning tunneling spectrum on the two positions marked in **a** (green and gray cross), Se vacancy (green line) and moiré peak (gray curve), reveal two spin-orbit-split defect states (D_1 and D_2, dashed lines) at 270 mV and 500 mV within the band gap (inset: schematic of the unfolded Brillouin zone). For LW-STS, a terahertz pulse is coupled to the junction acting as an ultrafast bias voltage (**c**). As the peak electric field of the terahertz waveform is swept through the band structure (**b**, purple curves), select tunneling channels are opened sequentially. The shape of the waveform was measured in the tip-sample junction using the photo-assisted tunneling scheme [Yos19, Mü20].

field $E_{\mathrm{LW}}^{\mathrm{peak}}$. The time-integrated net current $I_{\mathrm{LW}} = \langle \mathcal{J}_{\mathrm{LW}}(t) \rangle$ can, hence, contain contributions from electrons tunneling through multiple states. In contrast, the picture changes for state-specific tunneling [Coc16, Pel20, Pel21] (section 3.1). At the tunneling onset into a specific state, the instantaneous current can be strongly confined in time to the field crest of the terahertz transient [Coc16] and I_{LW} is dominated by the contributions of $\mathcal{J}_{\mathrm{LW}}(t)$ at the crest $V_{\mathrm{LW}}^{\mathrm{peak}}$ of the voltage transient, such that it approximates the instantaneous tunneling current. Hence, at the rising edge of an effective single-level system, the lightwave-driven spectrum, $\mathrm{d}I_{\mathrm{LW}}/\mathrm{d}E_{\mathrm{LW}}^{\mathrm{peak}}$, is expected to approximate the LDOS measured by $\mathrm{d}I/\mathrm{d}V$ in conventional tunneling spectroscopy. In our case, this is achieved by accessing select states of the chalcogen vacancy.

Extraction of lightwave-driven tunneling spectra. The conjecture of state-selective tunneling in LW-STS can be tested by taking I_{LW}-$E_{\mathrm{LW}}^{\mathrm{peak}}$ curves at a vacancy lobe and a position, where the defect states are absent. Due to the shape of the waveform and the position-dependent LDOS measured by steady-state $\mathrm{d}I/\mathrm{d}V$ (Fig. 6.7b), the negative half-cycles of the lightwave should not contribute to the net current substantially. In contrast, the positive half-cycle is expected to dominate I_{LW} and to rise steeply once its peak probes the lower defect level or the conduction band on pristine $\mathrm{WSe_2}$. Before each measurement, the tip is stabilized on a defect-free spot on the monolayer without terahertz irradiation in constant-current mode (setpoint: $V = 30$ mV, $I = 50$ pA). After disabling the feedback, the tip is approached by another $\Delta z = -1.7$ Å. At this height, we measure I_{LW} for different peak fields $E_{\mathrm{LW}}^{\mathrm{peak}}$ (Fig. 6.8a). On pristine monolayer, at a peak of the moiré pattern, barely any lightwave-driven current is measurable (Fig. 6.8a). Conversely, I_{LW} clearly rises as a function of $E_{\mathrm{LW}}^{\mathrm{peak}}$ at an orbital lobe of the Se vacancy, even for small peak fields. This behavior indicates selective tunneling through the vacancy states. The amplitude of the near-field transient scales linearly with the peak field of the far-field transient coupled to the STM, where E_0 describes the unattenuated field. Differentiating the smoothed I_{LW}-$E_{\mathrm{LW}}^{\mathrm{peak}}$ curves (Fig. 6.8a) with respect to $E_{\mathrm{LW}}^{\mathrm{peak}}$ yields lightwave-driven scanning tunneling spectra $\mathrm{d}I_{\mathrm{LW}}/\mathrm{d}E_{\mathrm{LW}}^{\mathrm{peak}}$ of Se vacancy and moiré peak (Fig. 6.8b). Such a measurement is conducted N times with the exactly same settings and then I_{LW}-$E_{\mathrm{LW}}^{\mathrm{peak}}$ is differentiated for each measurement. We estimate the error bars for

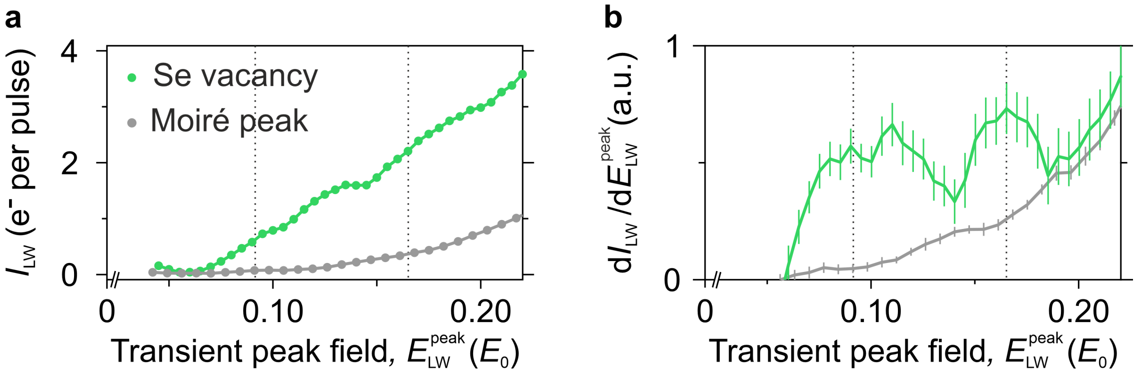

Figure 6.8 | Lightwave-driven scanning tunneling spectra. **a**, The lightwave-driven current I_{LW} as a function of the peak electric near field rises steeply on the Se vacancy, whereas on pristine monolayer (moiré peak) barely any signal is measured. The $I_{\mathrm{LW}} - E_{\mathrm{LW}}^{\mathrm{peak}}$ curve is smoothed with a nine-point Savitzky-Golay filter before numerical differentiation to avoid artifacts caused by noise between neighboring data points. **b**, The resulting lightwave-driven scanning tunneling spectra $\mathrm{d}I_{\mathrm{LW}}/\mathrm{d}E_{\mathrm{LW}}^{\mathrm{peak}}$ disclose position-dependent features with two areas of increasing tunneling probability on the Se vacancy marked by dashed lines in both panels.

$\mathrm{d}I_{\mathrm{LW}}/\mathrm{d}E_{\mathrm{LW}}^{\mathrm{peak}}$ using the bootstrap method [Efr82]. For every parameter set, the N measurement cycles are randomly resampled with replacement $M \times N$ times ($M = 10000$) and averaged individually yielding 10000 mean values. Their standard deviation is shown as error bar in the spectra throughout this thesis.

The two spectra on the vacancy orbital and pristine monolayer (Fig. 6.8b) qualitatively resemble conventional tunneling spectra in the voltage range from 0 V to ~600 mV at the respective positions (Fig. 6.7b). On the vacancy orbital (Fig. 6.8b), two peaks arise in $\mathrm{d}I_{\mathrm{LW}}/\mathrm{d}E_{\mathrm{LW}}^{\mathrm{peak}}$ (dashed lines), which can be attributed to the two spin-orbit-split defect levels (more details in sections 6.3 and 6.4). Using the tunneling onset into the first defect, we calibrate the peak field $E_{\mathrm{LW}}^{\mathrm{peak}}$ in units of volts in the following section.

6.3 Field calibration in lightwave-driven spectra

In this section, we ensure the correct assignment of prominent features in lightwave-driven spectra to actual defect states. To this end, we connect spatial and spectral fingerprints in LW-STM and LW-STS.

State assignment. To link spectral features (Figs. 6.7b and 6.8b) with snapshots of atomic-scale wave functions, we compare spectral and spatial fingerprints in steady-state STM (Fig. 6.9a-c) and LW-STM (Fig. 6.9d-f). Below the onset of a lightwave-driven tunneling current (Fig. 6.8), at $E_{\mathrm{LW}}^{\mathrm{peak}} = 0.07\ E_0$ (Fig. 6.9d), a nearly circular contrast is apparent and matches very well the steady-state STM image at $V = 210$ mV below the first defect level (Fig. 6.9a). For $E_{\mathrm{LW}}^{\mathrm{peak}} > 0.1\ E_0$ (Fig. 6.9e), the lightwave-driven image nicely reproduces the C_3 symmetry of the vacancy orbitals and even slight asymmetries (Fig. 6.9b). Above the conduction band edge ($E_{\mathrm{LW}}^{\mathrm{peak}} = 0.4\ E_0$, Fig. 6.9f), the defect appears as a void of drastically reduced current just as in the DC-STM image (Fig. 6.9c). The excellent agreement of steady-state and lightwave-driven STM images allows us to unambiguously identify the first rising edge in $\mathrm{d}I_{\mathrm{LW}}/\mathrm{d}E_{\mathrm{LW}}^{\mathrm{peak}}$ with the tunneling onset of the D_1 level of the Se vacancy. Knowing this, we can calibrate the electric field coupled into the junction in units of volts between tip and sample using the ratio between V and $E_{\mathrm{LW}}^{\mathrm{peak}}$.

Field calibration. In principle, one could try to match steady-state and lightwave-driven spectra in a one-to-one fashion to calibrate the lightwave-driven data. Using the D_1 and D_2 peak position as two independent markers, we receive the calibration of the unattenuated peak far-field amplitude as $E_0 = (3.0 \pm 0.1)$ V. While lightwave-driven and conventional spectra seem to agree well, they are not expected to unveil the same shapes for several reasons. First, the time window for tunnel events at a specific accessible energy keeps growing with increasing peak electric field. For a select energy level, the best temporal resolution is expected at its tunneling onset (section 3.1). Second, the transient could induce dynamics that are probed within the same waveform. In particular, several electrons tunneling per pulse could alter the shape of lightwave-driven spectra due to a Coulomb blockade. Remarkably, at $E_{\mathrm{LW}}^{\mathrm{peak}} \leq 0.1\ E_0$, on average, less than one electron tunnels per pulse. At these field strengths, a Coulomb blockade dominating lightwave-driven spectra due to a previously tunneled electron can be excluded. These considerations together with a straightforward interpretation of lightwave-driven spectra in the regime of state-selective tunneling motivate us to calibrate the spectra using D_1 only. Indeed, we expect the lightwave-driven spectra to reproduce the steady-state ones only at the tunneling onset into D_1. However, few data points around D_1 do not suffice to

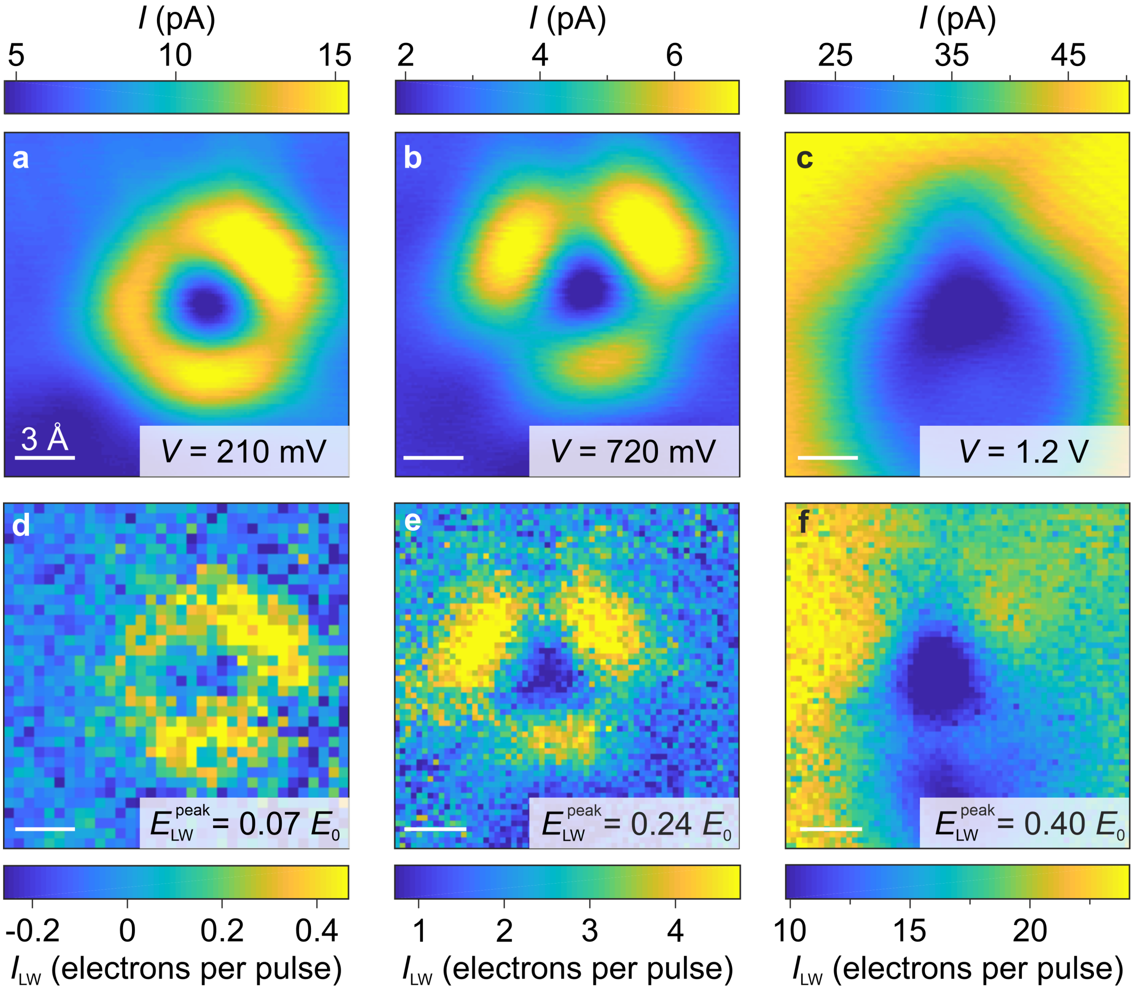

Figure 6.9 | Vacancy-state assignment in LW-STM. Steady-state (**a**-**c**) and lightwave-driven (**d**-**f**) STM images in constant-height mode reveal the bias and peak-field dependent features of the defect states below (**a**,**d**) and above the vacancy states (**b**,**e**) as well as within the conduction band (**c**,**f**). Their perfect correspondence allows for assigning defect states to the peaks seen in lightwave-driven spectra (Fig. 6.8b).

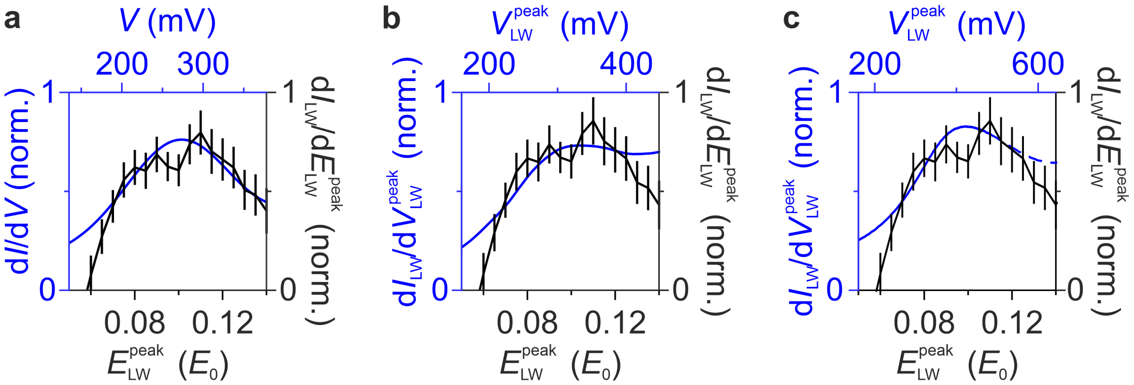

Figure 6.10 | Field calibration in units of volts. The maximum peak field in the STM junction is calibrated by comparing the appearance of D_1 in the lightwave-driven spectrum on the Se vacancy (data, black) with that in the steady-state spectrum (blue) (**a**) to 2.7 V. Comparing the data both to the simulated spectrum based on the instantaneous tunneling model $\mathcal{J}_{\mathrm{LW}}(t) = I(\mathcal{V}_{\mathrm{LW}}(t))$ (**b**) and the simulated spectrum based on a rate equation model assuming a 5 fs lifetime of D_1 (**c**) yields a maximum peak voltage of 3.2 V induced in the junction. On average, we can calibrate E_0 as $V_{\mathrm{LW}}^{\mathrm{peak}} = (3.0 \pm 0.3)$ V.

determine a meaningful calibration factor. Instead, we compare the appearance of D_1 in lightwave-driven spectra with three different curves (Fig. 6.10). A direct comparison of D_1 in the steady-state spectrum and lightwave-driven spectrum suggests that the unattenuated peak field of the far-field probing transient E_0 induces a voltage of 2.7 V (Fig. 6.10a). Alternatively, one can compare the lightwave-driven spectrum to simulations. Based on the relation $V_{\mathrm{LW}}^{\mathrm{peak}} \propto E_{\mathrm{LW}}^{\mathrm{peak}}$ [Pel21], we insert the measured near-field waveform $\mathcal{V}_{\mathrm{LW}}(t) = V_{\mathrm{LW}}^{\mathrm{peak}} \cdot f_{\mathrm{LW}}^{\mathrm{norm}}(t)$ (Fig. 6.7b) with different peak voltages $V_{\mathrm{LW}}^{\mathrm{peak}}$ into $\mathcal{J}_{\mathrm{LW}}(t) = I(\mathcal{V}_{\mathrm{LW}}(t))$ to compute the instantaneous tunneling current (instantaneous tunneling model, see also section 3.1). Here, $f_{\mathrm{LW}}^{\mathrm{norm}}(t) = E_{\mathrm{LW}}(t)/E_{\mathrm{LW}}^{\mathrm{peak}}$ is a unit-less function describing the shape of the electric field $E_{\mathrm{LW}}(t)$ in the tunnel junction. For each peak voltage $V_{\mathrm{LW}}^{\mathrm{peak}}$, the temporal integral over the whole waveform yields

$$\int \mathcal{J}_{\mathrm{LW}}(t)\mathrm{d}t = I_{\mathrm{LW}}$$

such that $I_{\mathrm{LW}}(V_{\mathrm{LW}}^{\mathrm{peak}})$ can be calculated. The derivative of the latter (Fig. 6.10b) indicates a peak voltage of 3.2 V induced by E_0. The same calibration factor is retrieved when the spectrum is simulated including a rate equation model, which mimics the impact of a 5 fs lifetime of electrons tunneling through D_1 on the lightwave-driven spectrum (Fig. 6.10c, see section 6.4 for simulation details). All calibration methods together allow us to calibrate the maximum peak terahertz voltage corresponding to the unattenuated incident field E_0 as $V_{\mathrm{LW}}^{\mathrm{peak}} = (3.0 \pm 0.3)$ V.

In summary, we can measure lightwave-driven spectra and retrieve their derivative in a model-free manner – but even more, by calibrating the peak voltage in the junction and comparing spatial and spectral fingerprints, we can unambiguously assign the first defect level to the first peak in a lightwave-driven tunneling spectrum. In the next section, we will address the temporal resolution of our technique.

6.4 Ultrafast temporal precision in lightwave-driven spectra

In sections 6.2 and 6.3, I have shown that we can measure lightwave-driven tunneling spectra that reproduce the spectral features of an atomic chalcogen vacancy seen in steady-state STS. At the tunneling onset into the lower bound state of the chalcogen vacancy, the lightwave-driven spectrum can even be seen as an ultrafast analogue of conventional tunneling spectroscopy, which is linked to the LDOS. Naturally, the question arises, which temporal precision we achieve for specific peak voltages of our terahertz transient.

Temporal resolution in LW-STS. On a basic level, the temporal resolution in LW-STM can be understood as the time window spanned by the part of the near-field transient which dominates the lightwave-induced tunneling current. It is limited by the LDOS, the pulse shape of the terahertz transient and its peak electric field (section 3.1). Conventionally, the temporal resolution in LW-STM is defined as the full width at half maximum (FWHM) of the instantaneous tunneling current $\mathcal{J}_{\mathrm{LW}}(t)$ induced by a terahertz transient at a given peak field [Coc13, Coc16]. We can apply this definition of temporal resolution to LW-STS, since also here, tunneling currents are driven by terahertz waveforms attenuated to specific peak voltages. In principle, one would like to directly measure the instantaneous tunneling current in the STM junction. Such experiments are extremely demanding and have become accessible only very recently [Sid24]. In our setup, however, the latter measurement cannot be implemented. To determine the temporal precision of lightwave-driven spectra around D_1, we perform an autocorrelation experiment and compare it to a simulation. Based on their agreement, we can simulate the instantaneous tunneling current and extract a peak-voltage dependent temporal resolution of LW-STS on a chalcogen vacancy like done similarly for the pioneering experiments in LW-STM [Coc13, Coc16].

Autocorrelation measurement. In an autocorrelation measurement (Fig. 6.11), two almost identical terahertz pulses are overlapped in the STM junction with variable delay time τ (Fig. 6.11a), such that their interference waveform acts as an ultrafast voltage pulse. Shape and magnitude of the latter are defined by the two terahertz waveforms and their mutual delay. The shape of the individual waveforms was measured using the photo-assisted tunneling scheme [Yos19, Mü20]. In the experiment shown in Fig. 6.11b, the waveforms are attenuated such that the peaks of the individual voltage pulses induce a transient voltage of 150 mV. Hence, the individual pulses do not drive substantial tunneling through D_1. However, their interference waveform can reach D_1 and the lightwave-driven current is expected to be maximal when the waveforms overlap ($\tau = 0$). Indeed, the measured delay-time-dependent change in lightwave-driven tunneling current ΔI_{LW} (Fig. 6.11b, black line) peaks at $\tau = 0$ with a autocorrelation peak width (FWHM) of 650 fs. The shape is asymmetric with respect to τ, which is caused by slightly differing waveforms of the two terahertz pulses and well reproduced by a simulation (blue line). Noteworthily, an experimental temporal autocorrelation measurement does not describe the temporal resolution in LW-STS. The latter is defined as the time window of tunneling, i.e., the FWHM of the instantaneous tunneling current, driven by one pulse only and needs to be simulated.

Autocorrelation simulation. The simulation mimicking the autocorrelation measurement uses the two detected near-field waveform traces shown in Fig. 6.11a. For each delay time, the electric field of the transients is added up to an interference waveform, which induces an ultrafast voltage pulse in the junction. Based on the

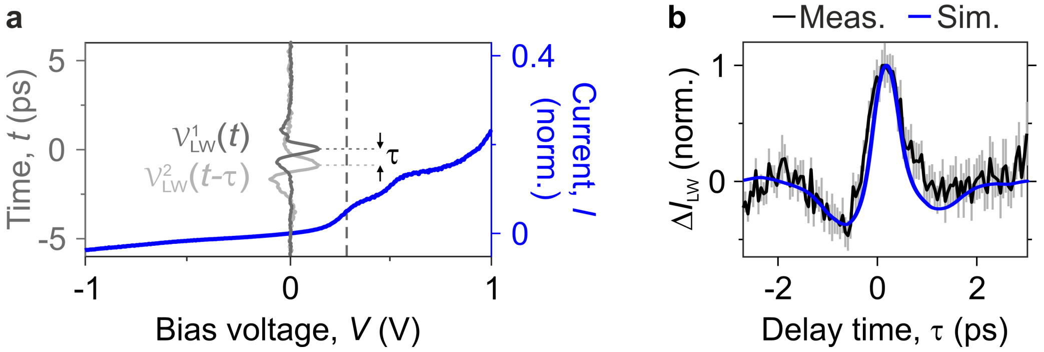

Figure 6.11 | Autocorrelation measurement and simulation. Two almost identical terahertz pulses (measured via photo-assisted tunneling [Yos19, Mü20]) are attenuated such, that the peaks of the individual voltage pulses $\mathcal{V}^1_{\mathrm{LW}}(t)$ and $\mathcal{V}^2_{\mathrm{LW}}(t-\tau)$ are tuned to 150 mV. When the terahertz waveforms are superimposed with a variable delay time τ in an STM junction (**a**), the interference waveform acts as an ultrafast bias voltage and induces an instantaneous tunneling current. Its integral I_{LW} is measured. The peak of their interference waveform reaches D_1, when the maxima of the waveforms overlap ($\tau = 0$). **b**, The delay-time dependent change of I_{LW}, ΔI_{LW}, exhibits an autocorrelation peak width shorter than a picosecond. The measured autocorrelation trace (black) is well reproduced by a simulation (blue).

steady-state I-V-curve, the instantaneous tunneling current driven by the interference waveform is simulated. From the instantaneous tunneling current, we calculate the measured current I_{LW} for a specific delay time. By doing this for every delay time between the two pulses, the measured autocorrelation trace can be simulated.

For average tunneling rates below one electron per pulse, we expect a simple model of instantaneous tunneling to reproduce measured data. For higher average rates, the probability of multiple tunneling events within a single pulse through the defect level increases such that a Coulomb blockade might alter the instantaneous current flow as well as the autocorrelation trace. To account for this, we utilize a rate equation model to treat the transient occupation of D_1. To simulate the instantaneous tunneling current, two contributions are summed up: tunneling through D_1 and the "background" current due to direct tunneling into pristine monolayer and substrate. Tunneling through D_1 is modeled using the rate equation

$$\frac{\mathrm{d}N}{\mathrm{d}t} = -\frac{N}{\tau_{\mathrm{LT}}} + \alpha(t,\tau) \times (1-N) \; .$$

Here, N describes the occupation of D_1, t is time, τ is the autocorrelation delay time as before, τ_{LT} denotes the lifetime of the first defect level and α is the instantaneous tunneling rate from the tip into the first defect level. Interpreting the broadening of D_1 in steady-state tunneling spectra (Fig. 6.7b) as lifetime broadening only, one can estimate the lifetime of an electron in D_1 as $\tau_{\mathrm{LT}} = \frac{\hbar}{\delta V \cdot e} \approx 5$ fs, where $\delta V \approx 125$ mV is the FWHM of D_1 in the steady-state tunneling spectrum. To extract this quantity, the two defect levels are matched by Lorentzian functions L_1 and L_2 with the background of direct tunneling into the gold substrate being fitted using a polynomial $\mathcal{P}$. In principle, there could be other contributions to broadening such that the actual lifetime is longer. Compared to the relevant timescales of terahertz probing in the autocorrelation measurements, which lies in the range of hundreds of femtoseconds (discussed later in this section), $\tau_{\mathrm{LT}} = 5$ fs is short and hence, the exact value of τ_{LT} does not determine the outcome of the simulation. The remaining unknown in the rate equation is $\alpha(t,\tau)$, the instantaneous tunneling rate from the tip to the first defect level, which depends on the instantaneous voltage $\mathcal{V}_{\mathrm{LW}}(t,\tau)$ in the junction. For each τ and t, L_1 is integrated up to $\mathcal{V}_{\mathrm{LW}}(t,\tau)$ to extract the scaling of α. The maximum α at $\tau = 0$ is estimated from currents in the autocorrelation experiment, which were kept slightly below one electron per pulse pair. From a simple model of instantaneous tunneling without the rate equation model, the time window of tunneling can be approximated to about 300 fs around D_1. In the rate equation model, we set the number of electrons tunneling through D_1 to maximally one electron per 300 fs. The maximum tunneling rate can be approximated as $\alpha_{\max} = \int_{-\infty}^{+\infty} \mathrm{d}V L_1(V) = 1/300$ fs since L_1 has low weight at negative voltages. For a specific instantaneous voltage $\mathcal{V}_{\mathrm{LW}}(t,\tau)$, this yields

$$\alpha(t,\tau) = \frac{\int_0^{\mathcal{V}_{\mathrm{LW}}(t,\tau)} \mathrm{d}V L_1(V)}{\int_{-\infty}^{+\infty} \mathrm{d}V L_1(V)} \alpha_{\max} \ .$$

Solving the rate equation model for every τ and t, the instantaneous tunneling current through D_1 can be extracted as

$$\mathcal{J}_{\mathrm{LW}}^{\mathrm{D}_1}(t,\tau) = N(t,\tau) \cdot e \ .$$

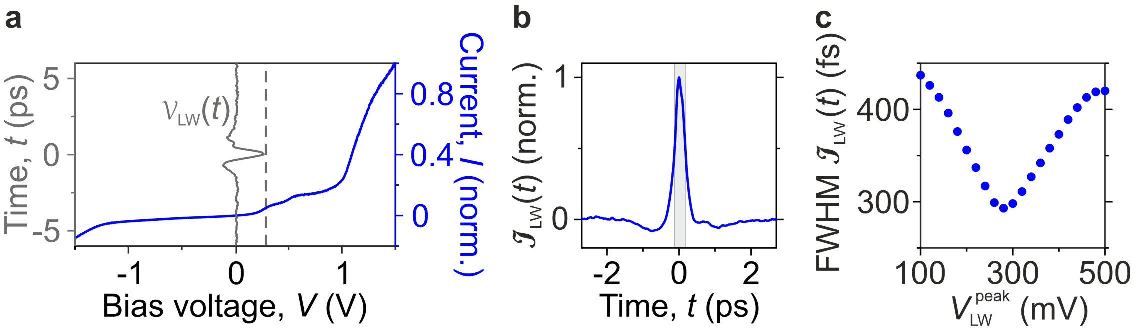

Figure 6.12 | Peak-field dependent temporal resolution. **a**, For a voltage pulse $\mathcal{V}_{\mathrm{LW}}(t)$ tuned to 280 mV (dashed line), the instantaneous tunneling current $\mathcal{J}_{\mathrm{LW}}(t)$ is calculated using the rate equation model (**b**). Its FWHM, the temporal resolution of LW-STS on the Se vacancy at a peak voltage of 280 mV, amounts to 296 fs. **c**, The temporal resolution simulated for different peak voltages yields tunneling windows below 350 fs in the ±100 mV vicinity around D_1.

The other contribution, tunneling directly into the gold substrate, is simulated using the simple instantaneous tunneling model without a rate equation assuming a vanishing lifetime. Here, the instantaneous current is calculated by integrating the background polynomial fit $\mathcal{P}$ from 0 V to $\mathcal{V}_{\mathrm{LW}}(t,\tau)$ as

$$\mathcal{J}_{\mathrm{LW}}^{\mathrm{bg}}(t,\tau) = \frac{\int_0^{\mathcal{V}_{\mathrm{LW}}(t,\tau)} \mathrm{d}V \mathcal{P}(V)}{\int_{-\infty}^{+\infty} \mathrm{d}V L_1(V)} \cdot \frac{e}{300\mathrm{fs}} \,.$$

For each delay time τ between the two terahertz pulses, the sum of $\mathcal{J}_{\mathrm{LW}}^{\mathrm{bg}}(t,\tau)$ and $\mathcal{J}_{\mathrm{LW}}^{\mathrm{D}_1}(t,\tau)$ is integrated to extract the total autocorrelation tunneling current $I_{\mathrm{LW}}(\tau)$. The simulated delay-time dependent change in tunnel current $\Delta I_{\mathrm{LW}}(\tau)$ reproduces the experimentally measured autocorrelation trace. Based on the excellent agreement of simulation and experiment, we can now simulate the instantaneous tunneling current of one pulse to extract the temporal resolution of LW-STS around D_1.

Peak-field dependent temporal resolution. For different peak fields around D_1, we simulate the instantaneous tunneling current induced by one terahertz pulse only, which will later be used as probe pulse (sections 6.5-6.7). When the peak of the waveform is tuned to $V_{\mathrm{LW}}^{\mathrm{peak}} = 280$ mV (Fig. 6.12a, gray dashed line), the FWHM of the instantaneous tunneling current simulated using the rate equation model yields

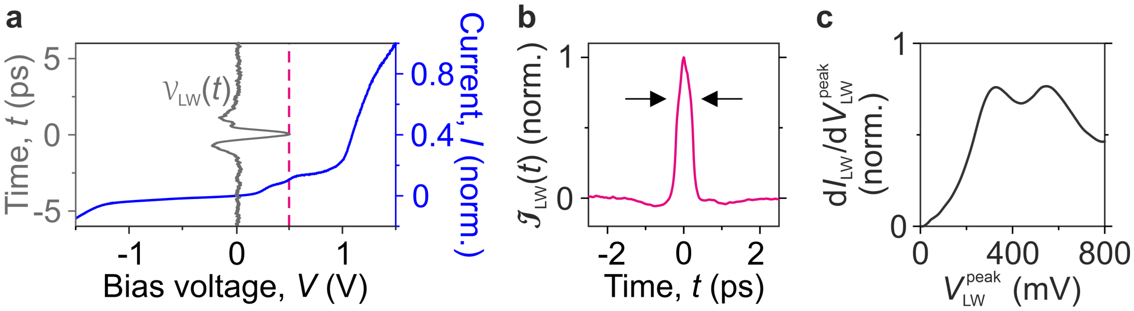

Figure 6.13 | Tunneling into higher-lying states. a, For $\mathcal{V}_{\mathrm{LW}}(t)$ tuned to 500 mV (dashed pink line), the instantaneous tunneling current $\mathcal{J}_{\mathrm{LW}}(t)$ is calculated using the rate equation model for D_1 (**b**). A sharp tunneling onset around $t = 0$ (arrows) on top of a broader shoulder signifies tunneling through D_2. The additional tunnel channel through D_2 causes the second peak in the simulated lightwave-driven tunneling spectrum (**c**). However, contributions from D_1 and D_2 to the lightwave-driven spectra cannot be disentangled at these voltages without further assumptions.

a temporal resolution in LW-STS of 296 fs (Fig. 6.12b). Calculating the FWHM of $\mathcal{J}_{\mathrm{LW}}(t)$ for a range of peak voltages reveals ultrashort tunneling windows of less than 350 fs in the ±100 mV vicinity of the first defect level (Fig. 6.12c). This tells us that we should be able to resolve ultrafast dynamics of D_1, for instance transient level shifts, in lightwave-driven spectra.

Higher-lying states in lightwave-driven spectra. When $V_{\mathrm{LW}}^{\mathrm{peak}}$ is tuned to voltages above D_1, tunneling contributions from the two defect levels mix. This can be understood visually by examining simulated instantaneous currents at such voltages (Fig. 6.13a,b). Tunneling into D_1 starts as soon as $\mathcal{V}_{\mathrm{LW}}(t)$ exceeds the corresponding threshold and does not stop until $\mathcal{V}_{\mathrm{LW}}(t)$ falls below the threshold. The same holds true for D_2, but with a higher threshold voltage. This is why the simulated instantaneous current $\mathcal{J}_{\mathrm{LW}}(t)$ for $V_{\mathrm{LW}}^{\mathrm{peak}} \sim \mathrm{D}_2$ (Fig. 6.13b) exhibits a shorter peak related to D_2 (arrows) on top of a broader shoulder due to tunneling through D_1. Hence, the sharp rise of $\mathcal{J}_{\mathrm{LW}}(t)$ is indeed caused by tunneling through D_2, but the experimentally measured time-integrated current mixes contributions induced by the whole transient, in this case from D_1 and D_2. Meanwhile, the second peak in lightwave-driven spectra (Fig. 6.8b) can be assigned to D_2 due to the additional tunneling channel that opens at higher voltages. Indeed, using the instantaneous tunneling model, the lightwave-driven spectrum can be simulated yielding a second peak at higher voltages caused by tunneling through D_2 (Fig. 6.13c), but the individual contributions of D_1 and D_2 cannot be disentangled from lightwave-driven tunneling spectra without further assumptions [Amm22]. As a consequence, the interpretation of data at higher peak voltages becomes more challenging. This is one reason, why I will focus on the interpretation of tunneling spectra at lower peak voltages around D_1 in the following sections. Additionally, for currents of more than one electron per pulse, Coulomb blocking could alter the shape of tunneling spectra. To prevent misinterpretation, we evaluate tunneling spectra at peak fields, where we drive tunneling currents below one electron per pulse, which is fulfilled at the tunneling onset into D_1 (Fig. 6.8). At these peak voltages, we ensure both state selectivity and single-electron tunneling such that we can expect the unconvoluted lightwave-driven spectrum to reflect the ultrafast LDOS.

So far, we have established lightwave-driven tunneling spectroscopy with calibrated peak voltages and we know that terahertz transients tuned to the tunneling onset into D_1 yield ultrashort tunneling windows of about 300 fs around D_1. Within these time windows, we can drive state-selective tunneling of single electrons enabling an interpretation of lightwave-driven spectra as the ultrafast LDOS. In the following, we want to induce structural motion and sample its impact on the transient ultrafast LDOS.

6.5 Local excitation of WSe_2 monolayer

Having understood our calibrated lightwave-driven spectra and their interpretation, we are prepared to finally excite structural motion in the sample and watch its impact on the instantaneous LDOS.

Excitation of structural motion. To excite and probe ultrafast motion we perform a terahertz-pump–terahertz-probe experiment. To this end, we delay two almost identical terahertz pulses (see Fig. 6.11), couple them into the STM junction and measure the impact of the pump pulse on the probe-driven current for different delay times. On an orbital lobe of a Se vacancy, the pump pulse induces a delay-time-

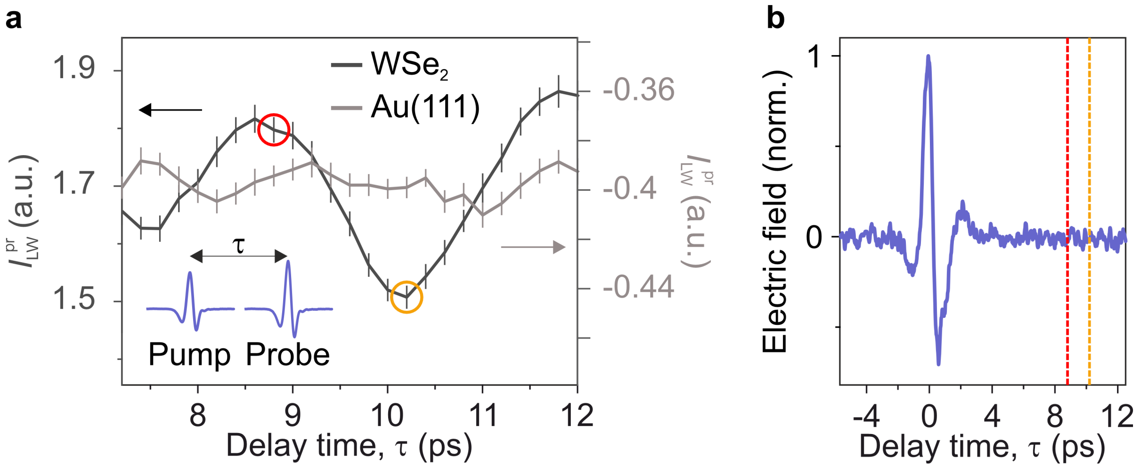

Figure 6.14 | Ultrafast dynamics on WSe_2. **a**, On WSe_2 (black curve), a terahertz pump pulse evokes ultrafast dynamics (schematic experiment: inset). After the delay time τ, a probe pulse samples the monolayer by inducing a lightwave-driven current, I_{LW}^{pr}. Its oscillatory modulation reflects the ultrafast dynamics induced. In the same delay-time window, Au(111) exhibits an almost constant lightwave-driven current (gray curve), measured on the same sample with the same tip. This suggests dynamics unequivocally linked to WSe_2. Moreover, the signal measured on Au(111) indicates that there are no trailing fields of the pump pulse in this time window. This conjecture is confirmed by detecting the electric field of the pump pulse via photo-assisted tunneling [Yos19, Mü20] (**b**). At the delay time of maximum (τ = 8.8. ps, red circle in **a**) and minimum (τ = 10.2 ps, yellow circle in **a**) lightwave-driven current on WSe_2, the measured pump pulse waveform does not exhibit any trailing fields (red and yellow dashed line).

dependent oscillation of the probe-driven current I_{LW}^{pr} (Fig. 6.14a). A maximum and a minimum are located at the pump-probe delay times τ = 8.8 ps and τ = 10.2 ps (red and yellow circles), respectively. The oscillation is unequivocally linked to the WSe_2 monolayer, since it is not visible on bare Au(111) with the same STM tip. The contrasting signal on WSe_2 and Au(111) indicates that potential trailing fields of the pump pulse do not induce the oscillatory signal on WSe_2 due to interference with the probe pulse. To certainly exclude such artifacts, we conduct a photo-assisted measurement of the terahertz pump transient, which confirms the absence of interfering trailing fields (Fig. 6.14b). In particular, delay times of extremal lightwave-driven tunneling current (Fig. 6.14a, circles) do not exhibit any features in the pump waveform (Fig. 6.14b, dashed lines). The probe-driven current on WSe_2

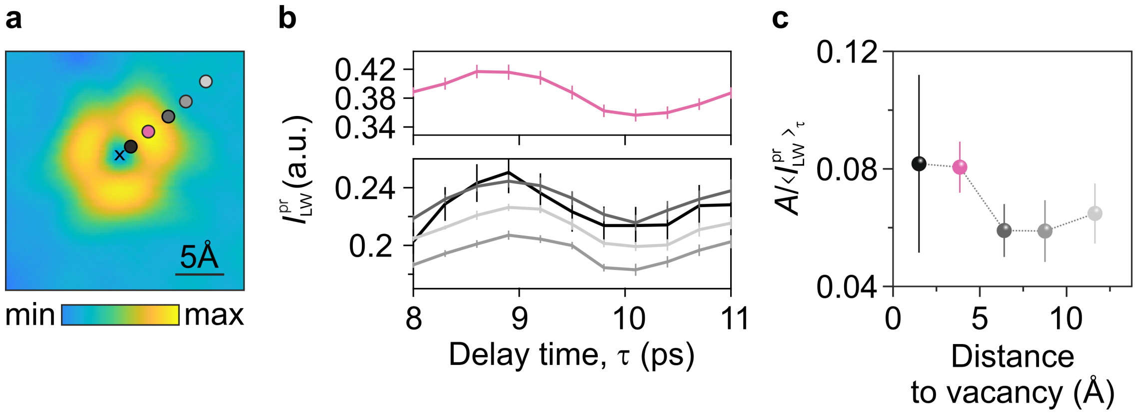

Figure 6.15 | Position-dependent amplitude of structural motion. At several tip positions marked in **a** relative to a Se vacancy (cross), the lightwave-driven probe current $I^{\mathrm{pr}}_{\mathrm{LW}}$ is measured as a function of delay time τ between pump and probe pulse (**b**). On all positions, ultrafast dynamics are captured with the same phase and frequency. From the $I^{\mathrm{pr}}_{\mathrm{LW}}$ traces, the relative oscillation amplitude $A/\langle I^{\mathrm{pr}}_{\mathrm{LW}}\rangle_\tau$ can be extracted (**c**), which peaks around the Se vacancy and decreases by about 25% on the surrounding pristine monolayer.

oscillates at slightly below 1 THz. Elementary dynamics we can induce and observe in LW-STM at such frequencies are phonons, in particular vertical oscillations. The high sensitivity of LW-STM to vertical motion is caused by the exponential dependence of the tunneling current to tip-sample distances (chapter 2). To better understand the nature of the observed dynamics, we examine their local occurrence.

Position-dependent oscillation amplitude. To find out whether the oscillations are localized, we conduct the same pump-probe experiment at different tip positions relative to a Se vacancy (Fig. 6.15a). Interestingly, at all positions $I^{\mathrm{pr}}_{\mathrm{LW}}$ exhibits the oscillatory behavior with similar phase (Fig. 6.15b). From the individual curves, we can extract the oscillation amplitude A by fitting sinusoidal functions. Here, the spatial dependence of $I^{\mathrm{pr}}_{\mathrm{LW}}$ itself could have an impact on the apparent oscillation amplitudes. To account for this, we normalize A by the respective delay-time-averaged current $\langle I^{\mathrm{pr}}_{\mathrm{LW}}\rangle_\tau$. The relative oscillation amplitude $A/\langle I^{\mathrm{pr}}_{\mathrm{LW}}\rangle_\tau$ (Fig. 6.15c) is maximized around the Se vacancy and drops by 25% on pristine monolayer. Remarkably, the motion pattern is present on all investigated positions on WSe$_2$.

From delay-time dependent tunnel current traces, it is not clear to which extent structural motion or modulations in the energy landscape influence the lightwave-driven current. Mechanical motion changes the tip-sample distance leading to a change of the tunnel barrier and hence the measured current. Conversely, structural motion could also influence the LDOS by shifting select energy levels. In contrast to lightwave-driven current traces, ultrafast tunneling spectroscopy can disentangle contributions from structural motion and shifts of select energy levels.

6.6 Non-equilibrium local density of states of a chalcogen vacancy

In the previous sections, we have established LW-STS yielding spectra which are calibrated in units of volts and have a temporal precision of about 300 fs around D_1. Moreover, we have seen in pump-probe experiments that we can induce ultrafast dynamics on WSe_2 which is reflected in an oscillatory behaviour of the lightwave-driven tunneling current driven by the probe pulse. However, contributions from structural motion and energy shifts cannot be disentangled from these current traces. To watch select energy levels evolving in time, we need to take snapshots of the transient LDOS after excitation of ultrafast dynamics. To this end, we combine a pump-probe experiment with ultrafast tunneling spectroscopy.

Transient local density of states. To resolve dynamics of individual energy levels, we excite ultrafast dynamics with a terahertz pump pulse on an orbital lobe of a Se vacancy and record a whole lightwave-driven tunneling spectrum with a probe pulse for specific delay times (Fig. 6.16a). Clearly, ultrafast tunneling spectra recorded at delay times of maximum (τ = 8.8 ps) and minimum (τ = 10.2 ps) lightwave-driven current (Fig. 6.14a, red and yellow circles) exhibit stark differences. Specifically, we see two effects: the entire spectra are scaled vertically as a whole and additionally, the transient LDOS yields variations of its lineshape with τ.

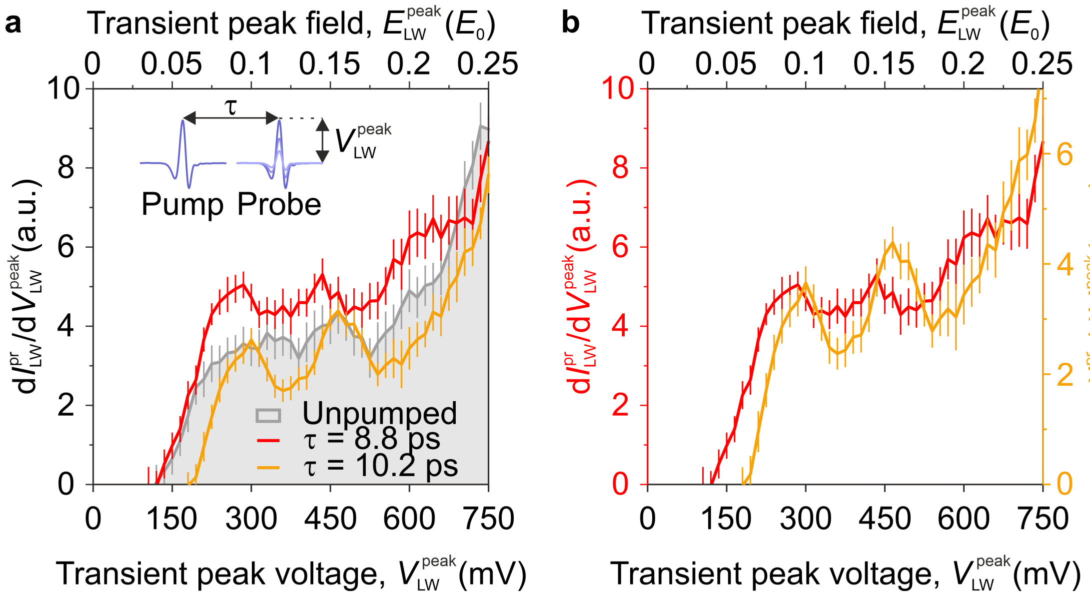

Figure 6.16 | Ultrafast snapshots of the LDOS. a, Ultrafast spectra recorded at delay times of extrema of ultrafast dynamics induced by a terahertz pump pulse (Fig. 6.14a) reveal an overall vertical rescaling as well as a horizontal shift around 150 mV. This shift becomes even more obvious, when the transient spectra are rescaled (**b**). The horizontal shift can be related to a transient shift of the tunneling onset into D_1 towards higher energies at $\tau = 10.2$ ps as compared to $\tau = 8.8$ ps.

Transient shift of first defect level in energy. An overall vertical scaling of tunneling spectra (Fig. 6.16a) can result from a change in the tunnel overlap of tip and sample wavefunctions. We assign the observed delay-time-dependent scaling of the spectra to a vertical structural motion of the whole monolayer, since the oscillations seen in delay-time-dependent lightwave-driven current traces are not confined to the vacancy position (Fig. 6.15). In contrast to an overall vertical scaling, horizontal shifts in tunneling spectra correspond to shifts of energy levels. In particular, the rising edge of D_1, around 150 mV shifts towards higher energies for $\tau = 10.2$ ps. The dynamics of the rising edge of D_1 could also be affected by changes in width of the D_1 energy level. However, the comparable shape of the transient spectra after excitation around D_1 indicates that a transient shift of the defect level in energy dominates the horizontal shift seen in transient tunneling spectra. Since the width of the defect level seems to be comparable only for the transient spectra, we compare time-resolved ultrafast tunneling spectra only. To account for the vertical scaling

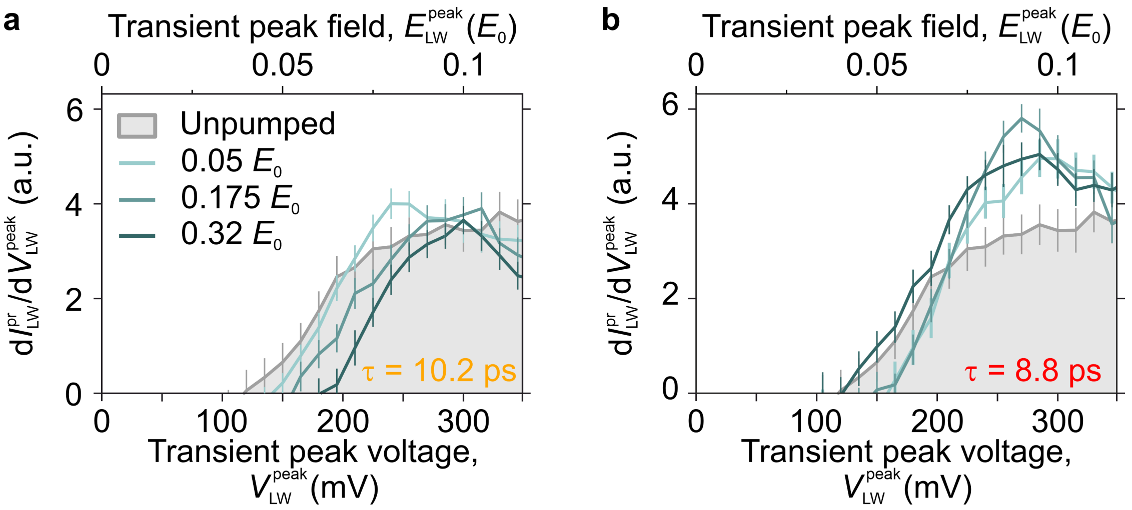

Figure 6.17 | Pump-field dependent shift of D$_1$. a, Ultrafast tunneling spectra at $\tau = 10.2$ ps reveal a monotonic shift of the rising edge of D$_1$ with increasing pump field strength. Meanwhile, at $\tau = 8.8$ ps (**b**), the tunneling onset into D$_1$ seems to shift in a non-monotonic fashion.

of the tunneling spectra related to a change in the tunnel barrier, we can scale the spectra such that they overlap for a large range of peak voltages (Fig. 6.16b). When doing so, a clear horizontal shift of the spectra remains at the tunneling onset into D$_1$. Also around D$_2$ distinguishable features seem to arise, however for the reasons explained in section 6.4 we concentrate on the interpretation of data around D$_1$. For peak fields below 0.05 E_0, a negative differential conductance can be seen in the lightwave-driven spectra, which stems from a reflection artifact in the setup. The attenuating wire-grid polarizer rescaling E_{LW}^{peak} of the probe field caused a reflection that induced a measurable current at low peak fields, rapidly vanishing for higher field amplitudes. This creates a negative differential conductance in the lightwave-driven spectra for peak fields below 0.05 E_0. Most importantly, the reflected field does not depend on the pump–probe delay time and hence does not affect the comparison of transient tunneling spectra. All time-resolved tunneling spectra were taken under exactly the same experimental conditions in one measurement cycle, ensuring their comparability.

Pump-field dependent energy shifts. To examine the origin of the D$_1$ energy shift, we investigate the shift behavior at $\tau = 10.2$ ps (Fig. 6.17a) and

τ = 8.8 ps (Fig. 6.17b) for different field strengths of the pump pulse. For this, the pump amplitude is tuned to three field strengths below the first defect level (0.05 E_0 corresponding to 150 mV), above the defect levels (0.175 E_0, 525 mV) and to the tunneling onset into the conduction band (0.32 E_0, 960 mV)). At τ = 10.2 ps, increasing pump fields promote the rising edge of D_1 to higher energies in a monotonic way. In contrast, at τ = 8.8 ps, moderate pump fields shift the tunneling onset to higher energies, whereas for the largest pump field the rising edge of D_1 seems to overlap with the unpumped tunneling onset. This non-monotonic behavior is indicative of competing mechanisms being responsible for the transient shift of the tunneling onset into D_1. So far, we interpret the data by directly looking at the spectra. Considering the error bars, the shift is clearly visible in the transient spectra. In this way, however, only a qualitative picture can be drawn calling for a quantitative analysis.

Quantifying the transient shift of the D_1 rising edge. To quantify transient shifts of the tunneling onset into D_1, we approximate the shape of every single transient spectrum with an error function (Fig. 6.18a,b). Every spectrum is fitted individually for positive-valued data up to a probe field of 0.1 E_0 including the error bars. Three free parameters are fitted: width, amplitude and inflection point. The latter can be used as a measure of the tunneling onset into D_1 for τ = 8.8 ps and τ = 10.2 ps. Since the vertical scaling of the spectra is accounted for by the amplitude fit, gap-size modulations do not contribute to the extracted inflection point. Plotting the latter as a function of pump field strength for the two delay times discloses the time-resolved tunneling onset into D_1 (Fig. 6.18c). It behaves as expected from the former qualitative interpretation of the spectra: the rising edge of D_1 shifts monotonically, roughly linearly with pump field strength for τ = 10.2 ps. Conversely, for τ = 8.8 ps, the tunneling onset shifts in a non-monotonic fashion. The difference between the tunneling onsets for the two delay times (Fig. 6.18d) yields the transient level shift of D_1. For the largest pump field (0.32 E_0, 960 mV), the transient level shift amounts to a field equivalent of 0.014 E_0, which can be translated to about 40 mV using our field calibration (section 6.3). The considerable shift of 40 mV exceeds thermal broadening that would occur at room temperature ($\sim$25 mV).

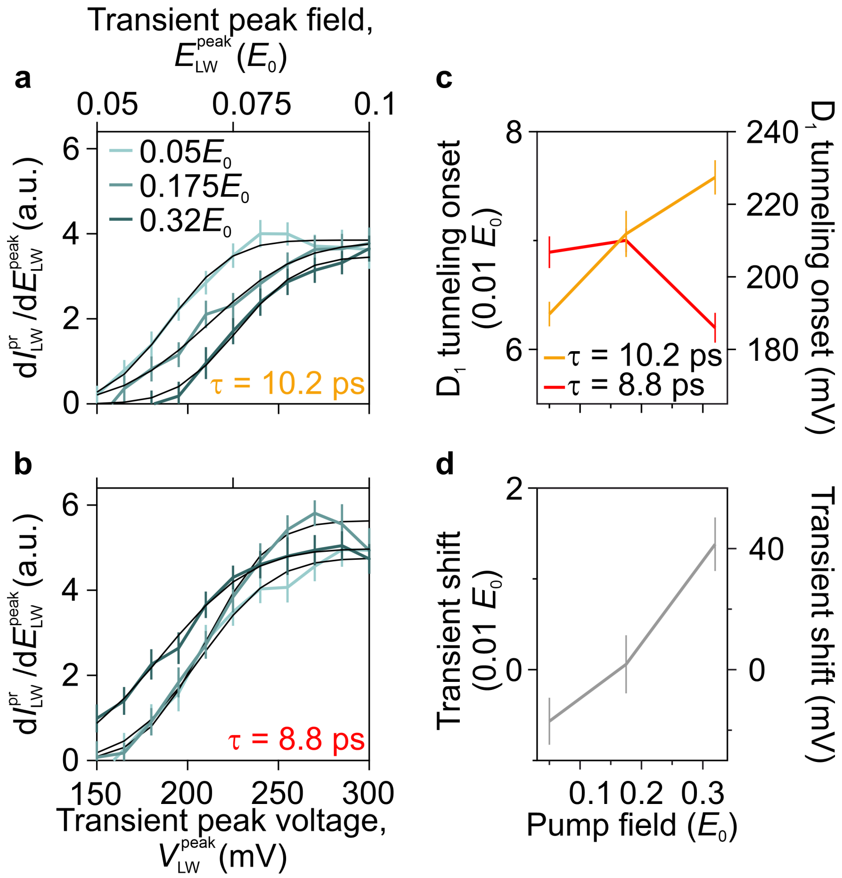

Figure 6.18 | Extracting the tunneling onset into D$_1$. The shape of transient tunneling spectra at $\tau = 8.8$ ps (**a**) and $\tau = 10.2$ ps (**b**) is approximated by an error function for each spectrum individually. Inflection point, width and amplitude are fitted as free parameters. **c**, The inflection point is used as a measure of the transient tunneling onset into D$_1$. As a function of pump field strength, it shifts roughly linearly for $\tau = 10.2$ ps and non-monotonously for $\tau = 8.8$ ps. **d**, The difference of the two curves shown in **c** yields the transient shift of D$_1$ amounting to about 40 mV for the highest pump field.

Our data demonstrate that we are not only able to state-selectively take snapshots in space and energy, but we can directly watch the ultrafast motion of the WSe_2 monolayer as well as the evolution of select energy levels in time. We found that D_1 shifts by considerable 40 mV upon excitation of structural motion. In the following, I will connect the fingerprints of structural motion and energy shifts.

6.7 Observing electron-phonon interaction

Utilizing time-resolved ultrafast tunneling spectroscopy (section 6.6), we have measured a transient shift of D_1 by up to 40 mV with simultaneous occurrence of structural motion (see also section 6.5). In this section, the exact motion pattern of the monolayer will be investigated based on experiment and DFT calculations. We find that a specific phonon mode influences the delay-time dependent shift of D_1, which we directly observe in the instantaneous LDOS constituting direct mapping of electron-phonon coupling on atomic scales.

Mechanical oscillation amplitude. To connect the fingerprints of structural motion and energy shifts, we estimate the magnitude of the vertical structural motion directly from oscillating current traces at large probe fields. There, the oscillation amplitude in the tunneling current can directly be translated to an excursion in real space as explained in the following. In Fig. 6.14a, a change in tunneling current of ∼10% occurs upon terahertz excitation with a probe field tuned to 1.8 V. At such large probe fields, the tunneling current is dominated by tunneling through the conduction band and the contribution from shifts in the tunneling onset in the first defect level to $I_{\mathrm{LW}}^{\mathrm{pr}}$ becomes negligible. At a peak voltage of 1.4 V, a simplistic instantaneous tunneling simulation yields a 1.5% change in $I_{\mathrm{LW}}^{\mathrm{pr}}$ for a 40 mV shift of D_1. Hence, for large probe fields, the oscillating tunneling current is expected to be dominated by structural motion. This conjecture is further supported by the occurrence of oscillation dynamics at all investigated positions and the qualitative similarities of the delay-time dependent oscillations on and off the defect (Fig. 6.15b). Since the lightwave-driven pump-probe currents are dominated by structural oscillations at high probe fields, we can try to extract two things. First, we can estimate the magnitude of structural motion in picometers. Second, we can try to

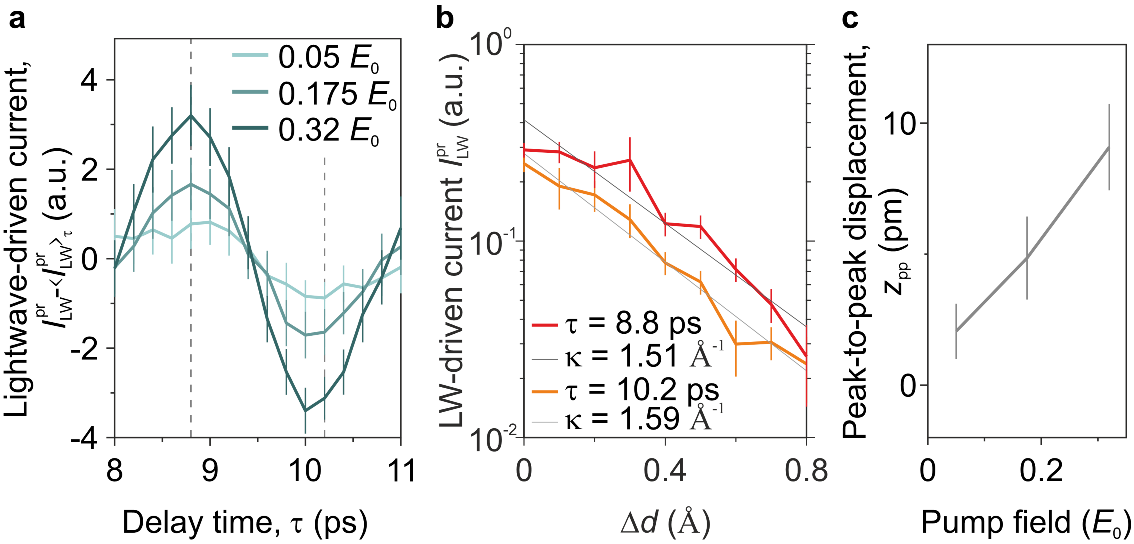

Figure 6.19 | Pump-field dependent structural motion. a, Oscillations in the probe current $I^{\mathrm{pr}}_{\mathrm{LW}} - \langle I^{\mathrm{pr}}_{\mathrm{LW}}\rangle_\tau$ can be seen for three pump fields: below D_1 (0.05 E_0), above the defect levels (0.175 E_0) and in the conduction band (0.32 E_0). The probe field is tuned to the conduction band onset such that structural changes dominate current oscillations rather than a shift of D_1. **b**, At $\tau = 8.8$ ps and $\tau = 10.2$ ps, the lightwave-driven current scales exponentially with change in tip-sample distance Δd, such that it can be written as $I^{\mathrm{pr}}_{\mathrm{LW}} \propto \exp(-2\kappa\Delta d)$. Fitting the logarithm of $I^{\mathrm{pr}}_{\mathrm{LW}}(\Delta d)$ linearly yields the decay constants $\kappa = 1.5$ Å^{-1} and $\kappa = 1.6$ Å^{-1}. Here, $\Delta d = 0$ corresponds to the height setpoint of $V = 30$ mV, $I = 49$ pA and 1.8 Å approach. Using the mean decay constant $\kappa = 1.55$ Å^{-1}, the structural peak-to-peak displacement can be extracted directly from delay-time-dependent current traces (**a**) as a function of the pump field and amounts to 10 pm for the maximum pump field.

find out which driving mechanism dominates the excitation of the monolayer: for instance, tunneling [Coc16] or the electric field of the pump terahertz pulse [Pel20] could drive mechanical motion. The latter two driving mechanisms scale differently with the pump field. Hence, we investigate experimental oscillating current traces at three different pump field strengths like done for transient tunneling spectra (Figs. 6.17 and 6.18). The probe pulse is tuned to the peak field 0.32 E_0 corresponding to 960 mV such that $V^{\mathrm{peak}}_{\mathrm{LW}}$ reaches the conduction band edge. For all three pump fields, $I^{\mathrm{pr}}_{\mathrm{LW}}$ is temporally modulated by the structural motion (Fig. 6.19a).

Figure 6.20 | D_1 onset projected onto structural displacements. From transient pump-field dependent shifts of the tunneling onset into D_1 (Fig. 6.18c) and pump-dependent mechanical oscillation amplitudes (Fig. 6.19c), the dynamics in space and energy can be related experimentally for the two delay times τ = 10.2 ps (left) and τ = 8.8 ps (right).

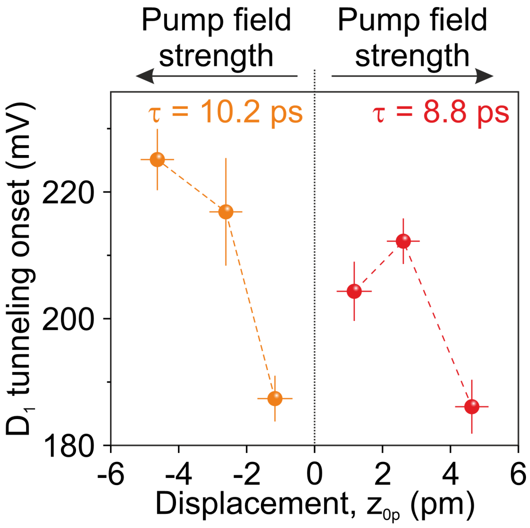

To translate the tunneling current to an excursion in real space, we use its exponential sensitivity to the tip-sample distance (Fig. 6.19b). Generally, the tunneling current in an STM junction can be described as $I(d) = a \cdot e^{-2\kappa d}$ (chapter 3). We extract κ as the slope of a linear fit to the logarithm of two $I_{\mathrm{LW}}^{\mathrm{pr}}$ curves for delay times τ = 8.8 ps and τ =10.2 ps individually yielding the mean decay constant $\kappa = 1.55$ Å^{-1}. Assigning the current oscillations of $I_{\mathrm{LW}}^{\mathrm{pr}}$ as a function of delay time to mechanical modulations of the tunnel barrier only, we can estimate the apparent oscillation amplitude seen in every individual $I_{\mathrm{LW}}^{\mathrm{pr}}$ trace (Fig. 6.19a) in picometers using $\kappa = 1.55$ Å^{-1}. We extract the peak-to-peak displacement of the monolayer from the ratio of maximum and minimum lightwave-driven tunneling current in the delay-time dependent traces as $z_{\mathrm{pp}} = d_{\mathrm{min}} - d_{\mathrm{max}} = -\log(I_{\mathrm{LW,min}}^{\mathrm{pr}}/I_{\mathrm{LW,max}}^{\mathrm{pr}})/2\kappa$. The structural peak-to-peak displacement rises linearly with the pump field (Fig. 6.19c) pointing towards a field-driven excitation mechanism rather than tunneling. At the highest pump field, the measured peak-to-peak amplitude in the lightwave-driven current corresponds to an out-of-plane motion of about 10 pm, which is slightly larger than the apparent height of moiré-induced modulations in topography scans (Fig. 6.5c).

Structural motion governing select energy levels. Knowing both pump-field-dependent shifts of the transient tunneling onset into D_1 (Fig. 6.18c,d) and the pump-field-dependent mechanical out-of-plane motion in picometers (Fig. 6.19c), we can connect the fingerprints of structural motion and energy shifts. For a sinusoidal oscillation of the tunneling current from an equilibrium position (Fig. 6.19a), the extracted pump-field-dependent peak-to-peak displacement z_{pp} (Fig. 6.19c) yields the symmetric excursion amplitude $z_{0\mathrm{p}} = \pm z_{\mathrm{pp}}/2$, where a positive (negative) excursion corresponds to the delay time $\tau = 8.8$ ps ($\tau = 10.2$ ps). Thereby, we retrieve a specific displacement $z_{0\mathrm{p}}$ for each delay time and pump field. Knowing the tunneling onset into D_1 for each delay time and pump field (Fig. 6.18c), we can directly connect the structural displacement and the shift of the tunneling onset into the electronic energy level D_1 for $\tau = 8.8$ ps and $\tau = 10.2$ ps (Fig. 6.20). The data shown in Fig. 6.20 constitute the direct observation of the temporal evolution of a locally confined state in energy upon structural motion. Due to the peculiar, partly non-monotonic shift of D_1 with rising pump field (Fig. 6.18c), the shift of D_1 as a function of the monolayer displacement also exhibits a non-monotonic and non-linear behavior (Fig. 6.20) indicating competing mechanisms driving the level shift.

At this point, we are able to map out the tunneling onset into D_1 as a function of vertical displacement of the WSe_2 monolayer. Meanwhile, the exact motion pattern evoking transient energy shifts is unknown. To find out what is happening on the atomic level, we combine knowledge from experimental measurements and DFT calculations.

Long-lived oscillation dynamics. To understand the transient shift of D_1, we need to investigate the atomic displacements of the WSe_2 monolayer. From experimental observations, we know that the oscillations are uniquely linked to the WSe_2 monolayer (Fig. 6.14). Moreover, the whole monolayer rather than just an orbital lobe of the vacancy is moving vertically, since $I_{\mathrm{LW}}^{\mathrm{pr}}$ oscillates at all measured positions and the traces captured at different tip positions yield the same qualitative behavior (Fig. 6.15). Measurements performed at large delay times evidence oscillations observable up to a 100-ps range (Fig. 6.21a). At a maximum around $\tau = 88.5$ ps and a minimum at approximately $\tau = 90$ ps, also the transient spectra (Fig. 6.21b) exhibit the same phase dependence as for earlier delay times. Most importantly, the long-lived vibrations indicate a select standing-wave mode rather than a traveling wave packet. To identify the approximate oscillation frequency, we record lightwave-driven currents over a ~90 ps delay time interval and investigate their Fourier amplitude. Due to reflections in a silicon beam splitter in the setup, the

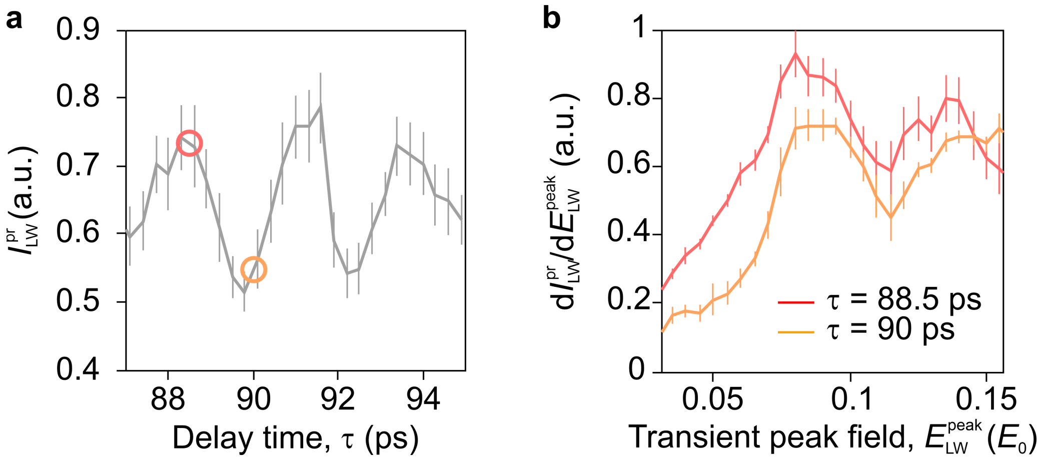

Figure 6.21 | Long-lived defect dynamics. a, On a Se vacancy, the lightwave-driven current features oscillations up to large delay times around $\tau = 90$ ps suggesting a standing-wave mode rather than a traveling wave packet. The current trace has a maximum at $\tau = 88.5$ ps (pink circle) and a minimum at about $\tau = 90$ ps (orange circle). **b**, The corresponding transient spectra exhibit a shift of the D_1 tunneling onset towards higher energy for $\tau = 90$ ps (orange curve) as compared to $\tau = 88.5$ ps (pink curve).

overlap of the probe pulse with trailing replica of the pump pulse result in a tunneling current enhanced at certain delay time windows. The temporally recurring features in the lightwave-driven current cause multiple peaks in the Fourier spectrum of the current trace (Fig. 6.22, green). To get rid of artifacts from pump pulse reflections, we compare the Fourier spectrum of the lightwave-driven current with the one of the pump waveform measured over the same delay time interval (Fig. 6.22, gray). In fact, the Fourier transforms of the measured near-field pump pulse including reflections and the lightwave-driven probe current overlap at almost all peaks but one located at 0.34 THz. Here, the Fourier amplitude of the tunneling current is almost twice as large. We attribute this frequency to the mode responsible for the shift of the tunneling onset into D_1. To clarify, which specific modes can occur in the WSe_2/Au(111) heterostructure and how they can impact the D_1 energy level, Maximilian Graml and Jan Wilhelm performed first-principles DFT calculations.

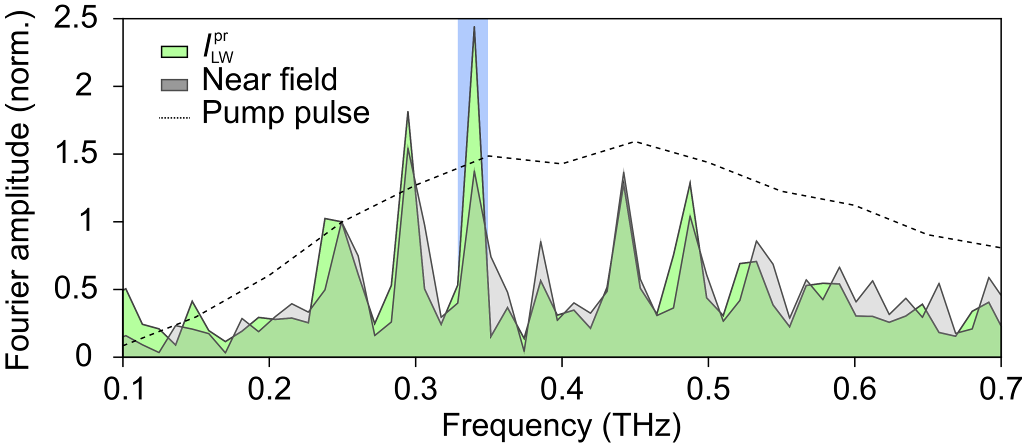

Figure 6.22 | Oscillation frequency. For the delay time window 7 ps $< \tau <$ 95 ps, the Fourier transforms of lightwave-driven current (green) and near-field waveform containing reflections of the pump pulse (gray) follow roughly the same envelope as the pump pulse itself (dashed line). Trailing replica of the pump pulse result in a multi-peak spectrum present in both traces. At 0.34 THz, however, the peak is strongly enhanced in the pump-probe current (blue shaded area), which we can attribute to the long-lived mode seen in oscillation traces. The Fourier spectra are normalized to their respective amplitudes at 0.25 THz. The near-field waveform and pump pulse are measured via photo-assisted tunneling [Yos19, Mü20].

Identify phonon mode and atomic motion pattern. To identify the phonon mode, which we observe in experiments, a phonon spectrum of the heterostructure is calculated. For the phonon spectrum, the geometry shown in Fig. 6.23 was employed. The pristine WSe_2 monolayer on Au(111) is included by a $(\sqrt{3} \times \sqrt{3})R30^\circ$ superstructure [Sar21] and tip and substrate are modeled as two atomic gold layers in Au(111) configuration. With this geometry, we want to identify the phonon mode and calculate the atomic motion pattern. In the calculation, the gold atoms are kept fixed. First-principles DFT calculations of the low-energy part of the phonon spectrum reveal the longitudinal (LA*) and transverse (TA* and ZA) acoustic modes of the WSe_2 monolayer on top of gold (Fig. 6.24a). Interestingly however, for the heterostructure, one of the degenerate out-of-plane transverse acoustic modes in the low-energy spectrum splits off the ZA mode and becomes gapped at the Γ point of the unfolded Brioullin zone of WSe_2 (red curve). Its motion pattern corresponds to a drum-like vertical oscillation of WSe_2 relative to gold. At the Γ point, the predominant motion is a vertical vibration of the whole monolayer (Fig. 6.24b,

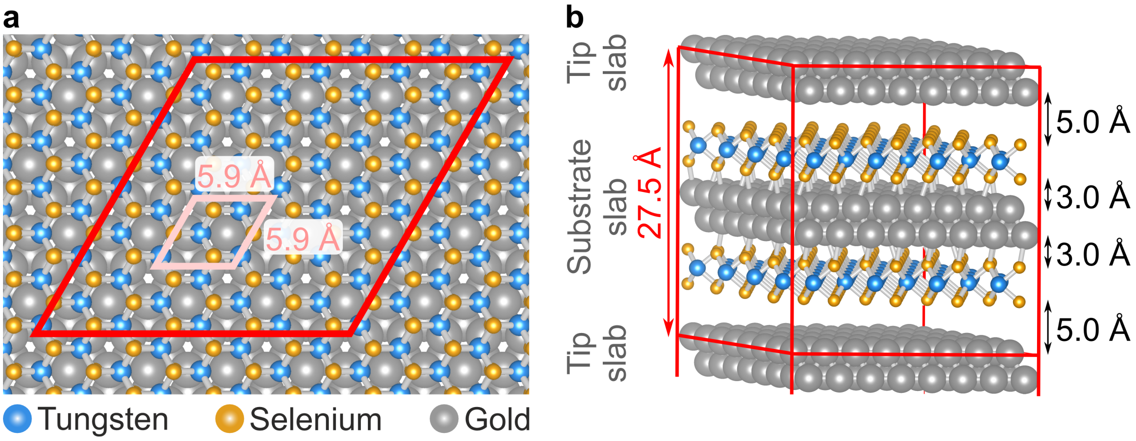

Figure 6.23 | Geometry for calculation of phonon band structure. a, Top view: in the calculation, the pristine WSe_2 monolayer on Au(111) is included in the DFT calculation by a 4×4 supercell (red) of a $(\sqrt{3} \times \sqrt{3})R30^\circ$ structure (rose) [Sar21]. The moiré lattice period in this configuration is 5.9 Å. **b**, Side view: tip and substrate are modeled as two atomic gold layers in Au(111) configuration. In total, 544 atoms are used for the calculation (visualization via Vesta [Mom11]).

gray arrows). Additionally, the monolayer itself is distorted internally, because the Se atoms move with respect to the center-of-mass motion (orange arrows) resulting in an oscillation amplitude of the W atoms that is ∼150% of the amplitude of Se atoms. It is expected that the atomically strong, predominantly out-of-plane terahertz electric near field of the pump pulse can efficiently couple to this drum mode (DM) by Coulomb interaction with charges in the heterostructure and by its field-induced polarization [She22]. The linear dependence of the structural oscillation amplitude on the applied electric field (Fig. 6.19c) points towards the former mechanism as the dominating contribution. Apart from the DM, less prevalent in- and out-of-plane components might also occur without being observed because of their dispersing frequencies causing a quick decoherence. Knowing the mode that is driven by the terahertz pump pulse, we can try to find out which energy shifts of D_1 are expected theoretically upon excitation of the DM.

Theoretically expected energy shifts. Considering the discussed DM motion, we estimate expected shifts of D_1 for different monolayer displacements. To do so, we assume that the defected WSe_2 monolayer is following the same DM motion

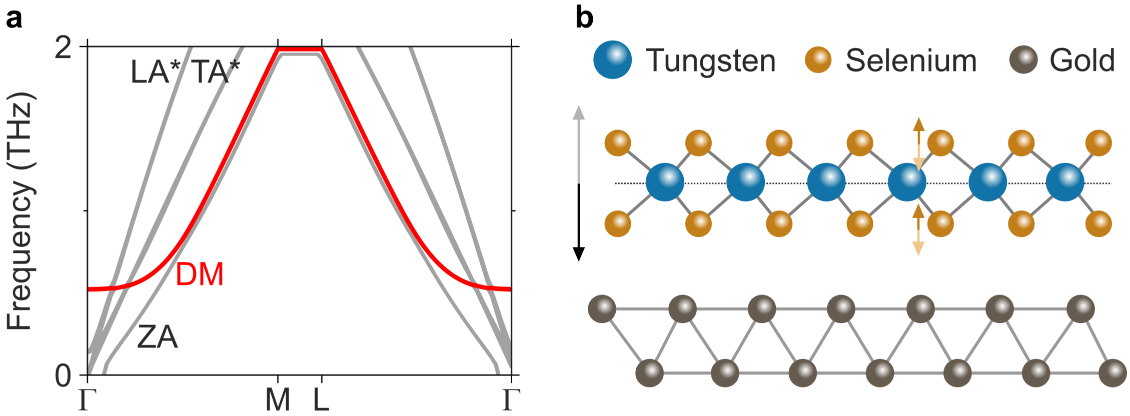

Figure 6.24 | Phonon spectrum and atomic motion pattern. **a**, A first-principles DFT calculation of the phonon spectrum yield longitudinal (LA*) and transverse (TA* and ZA) phonon branches. One mode (DM, red) splits off the ZA branch and is gapped at the Γ point with a frequency of 0.5 THz. **b**, At the Γ point, DM corresponds to a center-of-mass (dashed line) motion of the WSe_2 monolayer (gray arrows) together with smaller intracell distortions (orange arrows). Gold atoms are fixed in the the DFT calculations.

pattern as the pristine monolayer (Fig. 6.24b). Starting from the coarse motion, the overall vibration of the WSe_2 monolayer affects the Coulomb interaction of the D_1 state with its image charge distribution [Nea06] in the gold substrate and the tip. Additionally, the distortions within the unit cell can also modify the hybridization of the atomic orbitals. The contribution of these two effects are calculated individually and summed up to a total energy shift (Fig. 6.25, left panel).

To calculate the Coulomb-shifted energy levels, we include two image charges in tip and substrate (Fig. 6.25, right panel, purple dots). At the same time, we approximate the unoccupied defect state as infinitely localized (red dot). In this scenario, the image charge renormalization can be calculated analytically. During an out-of-plane displacement Δz_{Se} of the upper Se layer, D_1 shifts by $\Delta E_{\mathrm{IC}}(\Delta z_{\mathrm{Se}}) = -\frac{e^2}{16\pi\epsilon_0}\left((z_1 - \Delta z_{\mathrm{Se}})^{-1} - z_1^{-1} + (z_2 + \Delta z_{\mathrm{Se}})^{-1} - z_2^{-1}\right)$. Here, z_1 and z_2 describe the equilibrium distance of the defect to the image plane of the metal tip and metal substrate, respectively. For tip and substrate, the image plane is assumed to be located 1.4 Å outside of the outermost atomic layer as reported in [Kha16]. Usually, absolute tip-sample distances are unknown in STM experiments. This is why we estimate the tip-sample distance and hence z_1 from a point-contact consideration. In point contact, the resistance amounts to $R_0 = \frac{h}{2e^2}$. Knowing that $\kappa \approx 1.15$ Å^{-1} for steady-state STM at the usual height setpoint ($V = 30$ mV, $I = 50$ pA, $R = V/I = 600$ MΩ), we can extract a lower boundary of the absolute distance at the height setpoint of $\Delta d = 4.7$ Å by extrapolating the junction resistance $R(d) \propto V \cdot \exp(2\kappa d)$. Since we approach by another ∼1.7 Å for our measurements, the lower boundary of distance between upper Se layer and tip in our experiments amounts to approximately 3 Å. Based on this approach, we estimate the distance between the upper Se layer of WSe_2 and the tip in contact mode to be 3.5 Å. With the image plane at 1.4 Å outside the outermost atomic layer, we get $z_1 = 2.1$ Å. The value $z_2 = 5.5$ Å results from the equilibrium distance of the monolayer to the gold substrate. Based on these numbers, the shift of D_1 as a response to the displacement of the monolayer can be calculated for different excursions Δz_{Se} (Fig. 6.25, purple). Generally, the image charge effect is sensitive to the atomic geometry of the tip at such small distances.

The impact of intralayer distortions on the D_1 energy level is estimated using DFT calculations on a 12×12 supercell of monolayer WSe_2 with an individual Se vacancy. The atoms in the monolayer are displaced according to the DM: Se atoms are displaced by Δz_{Se}, tungsten atoms additionally by $\Delta z_{\mathrm{W\text{-}Se}}$. After that, the expected D_1 level energy $D_1^{\mathrm{PBE}}(\Delta z_{\mathrm{Se}})$ is extracted from the DFT calculations relative to the conduction band minimum $E_{\mathrm{CBM}}^{\mathrm{PBE}}(\Delta z_{\mathrm{Se}})$ (Fig. 6.25, left panel, blue curve).

Both effects, image charge renormalization and intracell distortions scale approximately linearly with the monolayer displacement and compete with each other. Meanwhile, the image charge effect seems to dominate the D_1 shift. While we are estimating the level shifts based on several assumptions, our simplified approach provides an estimate in the right order of magnitude (Fig. 6.25, black curve).

To compare the theoretical results with our experiments, we assume that the measured displacement amplitude (Fig. 6.19, Fig. 6.20) reflects the oscillation amplitude of the top Se layer such that z_{0p} equals Δz_{Se}. While the theoretically expected position of D_1 shifts linearly with the displacement amplitude (Fig. 6.25, black curve), this is not observed in experiments (Fig. 6.20). For large pump fields and hence large excursions of the monolayer, we see a monotonic behavior qualitatively similar to the theoretically predicted total shift of D_1. For smaller excursions, however, there appear to be smaller higher-order corrections on top leading to a non-monotonic asymmetric

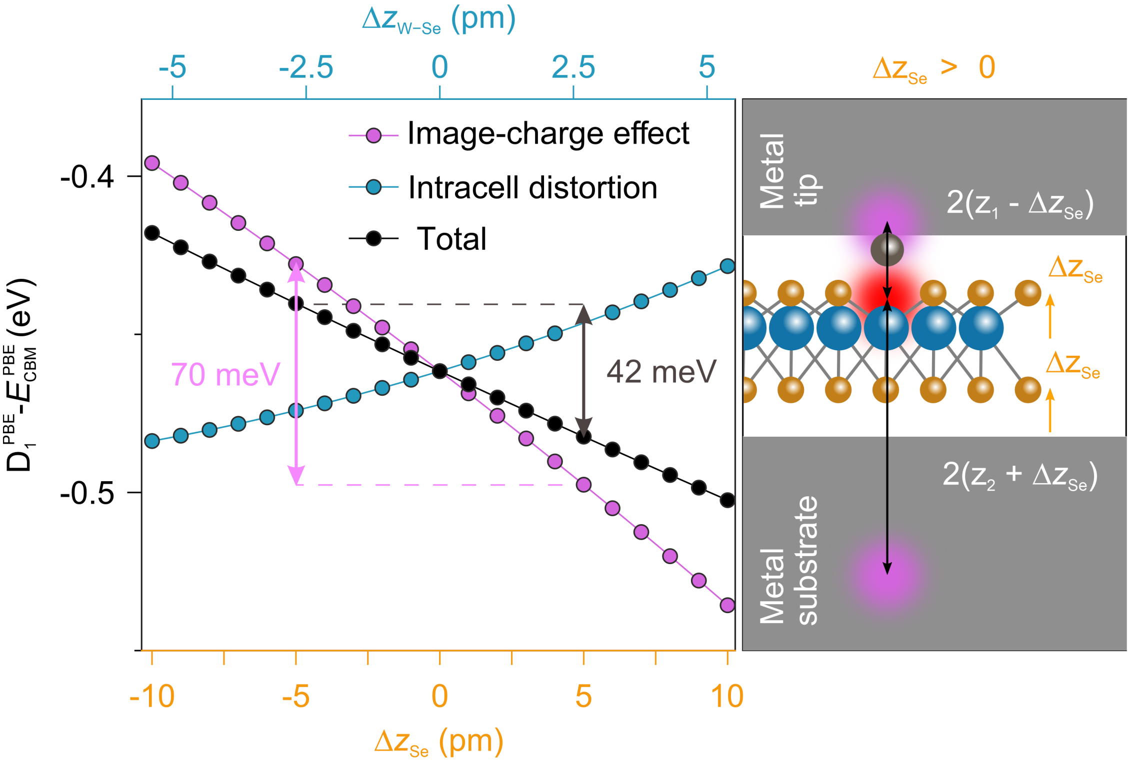

Figure 6.25 | Theoretically expected energy shifts. Left panel: the D_1 level shift relative to the conduction band minimum is calculated based on two effects: the image-charge effect (purple) and intracell distortion (blue). For the calculation, a defected monolayer is displaced by Δz_{Se} according to the DM (Fig. 6.24b) with the respective intracell motion of tungsten atoms relative to the Se atoms $\Delta z_{\mathrm{W\text{-}Se}}$. For a peak-to-peak displacement of 10 pm, the total calculated D_1 shift (black) amounts to about 40 meV. Right panel: schematic visualization of the simulation geometry. A positive Δz_{Se} corresponds to a monolayer displaced towards the tip; z_1 (z_2) denote the equilibrium distance between defect and tip (substrate) image plane. Atomic displacements are exaggerated by a factor of 100 for illustration purposes (red dot: defect, purple dots: image charges in tip and substrate).

shift. This behavior is not fully reproduced by theory, which is relying on model assumptions. At the moment, a full time-dependent atom-scale DFT calculation covering the different length scales including the moiré periodicity is computationally out of reach. The kinetic and chemical stability of the crystal around the vacancy further challenge DFT calculations. We hope that our study triggers future theory developments improving the current state-of-the-art approach.

We started with the goal to develop a technique to observe the interplay between structural motion and select energy levels in real space and in the time domain. To this end, we have developed defected monolayer TMDC samples suitable for STM (section 6.1) and we have established ultrafast LW-STS (sections 6.2-6.4) combining atomic, sub-picosecond and 10 meV-scale resolution. This allowed us to directly observe the impact of ultrafast structural motion on the transient local density of states (sections 6.5-6.7). We see how an acoustic DM transiently shifts the first defect level by up to 40 meV on timescales shorter than one oscillation period. The non-monotonic behavior of the shift with increasing excitation strength points towards a complex interplay of lattice distortions. With our simultaneous access to ultrafast spectroscopy on atomic length scales and to atomic vibrations on their intrinsic length and timescales, we pave the way for in-depth studies of local electron-phonon coupling. By adapting wavelength and shape of the pump pulse, our technique opens new pathways to excite specific atomically localized structural motion. Thereby, one should be able to transiently shift energy levels by a desired value to locally control many-body electronic states. Moreover, the direct real-space observation of moiré exciton trapping [RA18] might come true. Concluding, with time-resolved ultrafast LW-STS, we have established a technique which complements momentum-resolving ultrafast spectroscopy techniques with its atom-scale access allowing to investigate the building blocks of matter directly in space, time and energy at once.

Since the atom-scale world is governed by quantum mechanics, yet another degree of freedom can impact local ultrafast dynamics, namely the electronic spin. By tunneling spin-polarized electrons, a range of novel experiments would be feasible impacting different fields of fundamental science as well as the investigation of future quantum technologies. The development of a spin-polarized LW-STM will be discussed in the next chapter.

Chapter 7

Towards spin-resolved atomic-scale videography

The development of the spin-resolved LW-STM has been a venture driven by many people. The conception, its technical implementation and build-up of the STM has been put forward especially by Christoph Rohrer, Andreas Pöllmann, Andreas Rank, Victoria Ruckerbauer and Jascha Repp. The terahertz source has been developed and built by Christian Meineke, Peter Menden and Rupert Huber. I contributed to the conception of the STM, its build-up and the conception of STM-optics in- and out-coupling.

With the aid of LW-STM and LW-STS, it has been possible to directly observe structural motion in space and ultrafast shifts of localized electronic energy levels. To access the spin degree of freedom, spin-resolved STM can be employed [Wie09], which is constrained in time resolution as for conventional STM. With sophisticated measurement schemes in an atomic force microscope [Pat19b], microsecond lifetimes of triplet states can be measured locally [Pen21, Sel23]. Employing STM, electronics can be pushed to get nanosecond temporal precision such that spin dynamics could be investigated [Lot10]. Meanwhile, spin selectivity together with LW-STM would allow for a whole new class of experiments to unravel dynamical processes of spin-polarized materials directly in space. Spin resolution in spin-polarized STM (SP-STM) is facilitated by a magnetic field applied to the STM junction. Besides spin resolution, employing a magnetic field, for instance, also the Zeeman effect can be exploited to tune energy levels as a set screw to induce and control electronic wave packets. In the following, I will present exciting prospects of possible future experiments, which drive us to build a LW-STM including the option to apply a magnetic field.

Inducing wave packet dynamics. In principle, not only dynamics of electronic energy levels can be looked at in LW-STM (chapter 6), but also the motion of electronic wave packets. The latter can be initialized in different manners, depending on the exact material system and respective energy levels. In the following, I will discuss several ways to trigger wave packets in individual molecules. One option is to exploit spin-orbit coupling (SOC), e.g. in a molecule from the family of metalized phthalocyanine molecules, which represents a prototypical molecular spin system. Here, the center atom (Mg, Cu, Mn etc.) can be chosen to adjust molecular properties. Without taking SOC into account, the LUMO orbitals in phthalocyanine molecules are two-fold degenerate. They can be represented in a basis set, in which each of the two states is mainly localized on two of the four equivalent isoindole moieties of the molecule (sketch in Fig. 7.1a). Equivalently, in another basis set (L+ and L−), the orbitals possess an angular momentum of plus or minus one (Fig. 7.1b). When taking SOC into account, these two states couple to the spin degree of freedom, which can lift the degeneracy of the two orbitals. In a copper phthalocyanine (CuPc) molecule, this leads to an energy splitting in the millielectronvolt range [Sie15]. In conventional STM and STS, this splitting is obscured due to broadening of the energy levels. However, by charging the molecule and thereby accessing both energies at the same time, a wave-packet may be formed (Fig. 7.1c). The latter will show spatial oscillations of its density in time, with a frequency that is given by the splitting. In the case of CuPc, the splitting corresponds to oscillation periods on the picosecond timescale. Since in LW-STM the current can be injected and probed locally (e.g. at the red crosses in Fig. 7.1b,c), an oscillatory response in a pump-probe experiment is expected [Fra21], providing direct access to local wave packet dynamics in individual molecules. Employing a magnetic field, the energy levels could be tuned sensitively to control the local dynamics.

Even without considering SOC, electronic wave packets can be launched in individual molecules by applying a magnetic field. For instance, triangulene ($C_{22}H_{12}$) [Pav17],

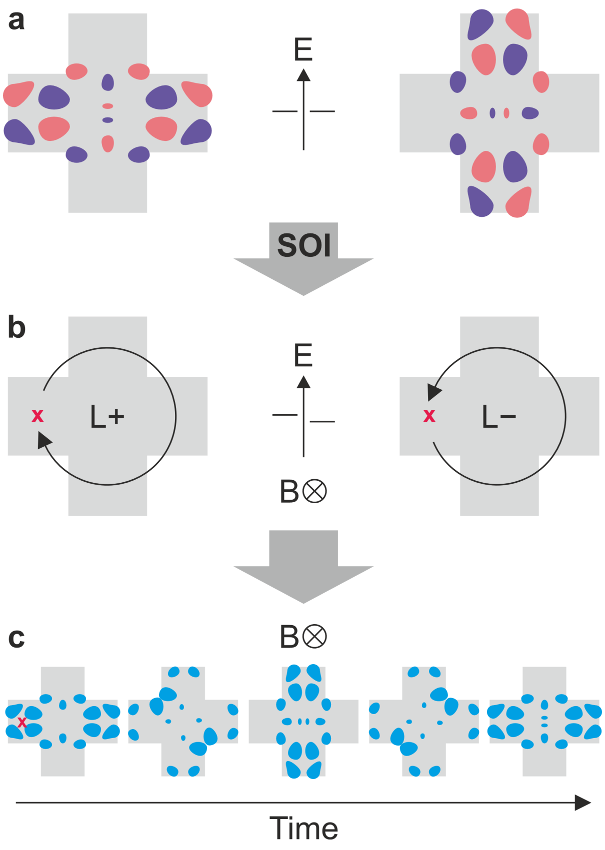

Figure 7.1 | Electronic wave-packets in a phthalocyanine molecule. The phthalocyanine molecule is schematically represented by a gray cross. **a**, The degenerate LUMO orbitals are localized on two of the four equivalent isoindole units of the molecule. **b**, Spin-orbit interaction can lift the degeneracy yielding orbitals of non-vanishing, opposing angular momentum. **c**, Local charge injection with an STM tip (red cross) into both energy levels can form an electronic wave packet with spatial oscillations of its density in time, which can be probed by LW-STM.

Figure 7.2 | Unpaired electrons triangulene. A schematic triangulene molecule ($C_{22}H_{12}$) exhibits a sublattice imbalance with the number of atoms in sublattice A (red dots), $N_A = 10$, being smaller than the one in sublattice B (blue dots), $N_B = 12$, yielding two unpaired electrons (black dots). The total spin quantum number is S = 1. The schematic shown is adapted from [Pav17].

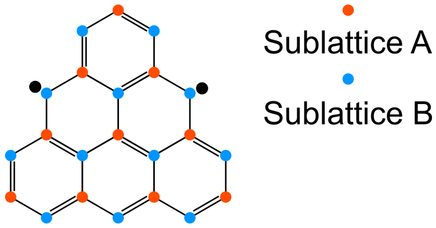

nanographenes [Mis20] and open-shell molecules [Mis22] offer a playground to study single molecules with unpaired electrons and in particular, their spin-dependent dynamics. The open-shell molecule triangulene (Fig. 7.2) is unstable in the solution phase, but can be synthesized and characterized in low-temperature ultrahigh-vacuum STM/AFM [Pav17]. Triangulene is a cutout from the bipartite graphene honeycomb lattice with an imbalance between the number of atoms located in the two sublattices ($N_A \neq N_B$, Fig. 7.2). This imbalance is the reason why it is not possible to pair up all p_z electrons of the carbon atoms into bonds leading to the generation of radicals [Ovc78]. The nanographene has a three-fold degenerate ground state [Ino01]. These energy levels may be split by a magnetic field inducing a detuning of $g\mu_B B$ with g being the gyromagnetic factor, μ_B the Bohr magneton and B the magnetic field applied. Corresponding wave packet dynamics should be resolvable in a LW-STM employing terahertz radiation if the energy difference of the energy levels lies in the millielectronvolt regime corresponding to picosecond dynamics. For an energy detuning of 1 meV one can roughly estimate the required magnetic field. If we assume the same gyromagnetic factor as for graphene [Lyo17], the detuning of electronic energy levels amounts to $\sim 2\mu_B B$. A magnetic field of about 7.5 tesla (T) is necessary to detune electronic energy levels by $2\mu_B B = 1$ meV. This energy difference corresponds to an oscillation period of 4 ps detectable in LW-STM.

As a consequence, with the magnetic field as an essential turning knob, wave packets can be induced in single molecules and potentially resolved via LW-STM. Employing spin-sensitive STM, also the local observation of ultrafast switching of magnetic domains is an exciting perspective.

Magnetic domain dynamics. In optical measurements, demagnetization dynamics of ferromagnets and their recovery have been investigated in the time domain [Bea96, Hoh97, Sch97, Gü99]. With visible light, ferromagnetic cobalt and nickel films on copper surfaces can be transiently demagnetized by changing the electron temperature [Gü99]. For three monolayers of cobalt on copper, this process has been shown to evolve on timescales below 50 fs. Subsequently, the formerly ferromagnetic films recover on picosecond timescales. However, purely optical measurements average over larger areas in space. To locally probe the magnetization dynamics, SP-STM together with optical-pump–terahertz-probe measurements would allow one to reveal dynamics driven by local properties. Indeed, cobalt islands on copper have been characterized in SP-STM in a time-averaged fashion [Rus05, Pie06]. Combining SP-STM with lightwaves, local magnetization-recovery dynamics could be watched directly in space. For instance, cobalt islands of different sizes would allow us to investigate edge effects. For such experiments, a prerequisite is a spin-resolving STM as well as optical access for pump and probe pulses.

Skyrmion dynamics. Magnetic skyrmions are topological states, where the spins in a material form a vortex-like structure. They are candidates as bits for data storage and logic devices. Magnetic skyrmions have been observed, for instance in iron layers on Ir(111), via SP-STM [Hei11, Hsu17] and they can even be written and read out with SP-STM employing electric fields [Rom13, Hsu17]. Meanwhile, their dynamical behavior is not fully investigated [Nag13]. Employing spin-resolved LW-STM, we could write skyrmions in iron layers on Ir(111) or delete them with a terahertz pump pulse tuned to high peak fields of about ±3 V [Hsu17]. Employing another terahertz waveform as a probe pulse at a much lower peak voltage, their build-up could possibly be watched directly in space. For magnetic skyrmions [Fer13, Oga15] and skyrmions based on surface-plasmon polaritons [Dav20], build-up [Oga15] and motion in space [Fer13, Dav20] have been observed with dynamics ranging from femtosecond [Dav20] to nanosecond [Fer13, Oga15] timescales. Coupling suitable pump and probe pulses to an STM for spin-resolved measurements, also internal dynamics could be investigated in detail, on atomic scales. Dynamically stabilized skyrmions [Zho15] might further open up exciting perspectives for locally probing skyrmion dynamics.

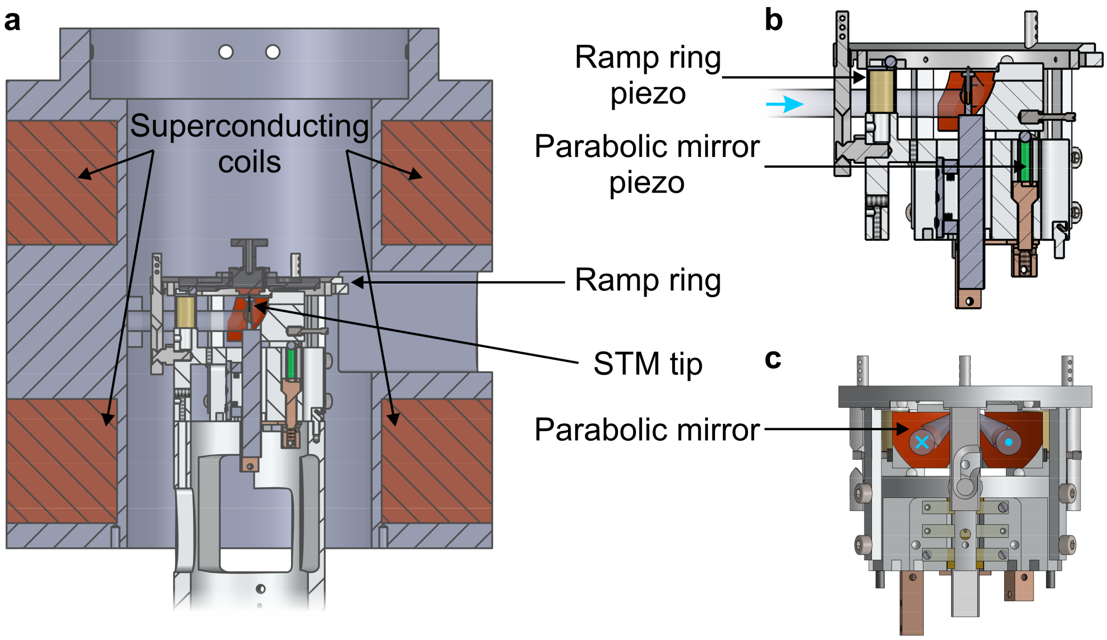

Figure 7.3 | Scan head of spin-resolved LW-STM. a, A cut through the STM scan head visualizes the position of the scan head in an area of homogeneous magnetic field generated by a superconducting split coil. The sample is mounted to a ramp ring, which is moved by three piezo actuators. One of these (golden) is visible in the cut (**a**) and its zoom version without a ramp ring (**b**). Another set of piezo actuators (green) allows for the in-situ alignment of a parabolic mirror (dark red), which focuses radiation (blue) onto the tip. Also coupling out scattered or emitted radiation from the tunnel junction is possible (**c**). CAD drawings by courtesy of Christoph Rohrer.

LW-STM with B field: requirements and challenges. To be able to conduct the introduced experiments, we aim to couple an optical setup generating intense phase-locked terahertz pulses to a low-temperature ultrahigh-vacuum STM with built-in magnetic field. The challenges met in the terahertz setup have been solved in the course of Christian Meineke's PhD thesis [Mei22, Mei24]. Based on the home-built STM [Coc16] used for the experiments explained in chapters 4–6, several parts of the STM – in particular, the scan head (Fig. 7.3) – were redesigned following the experience gathered in scanning near-field optical microscopy (SNOM) [Eis14, Hub16, Pla21, Sid24], similarly as described in Thomas Buchner's PhD thesis [Buc24]. For instance, the scan head is designed such that tip stays stationary and the sample moves when recording STM scans as customary in SNOM. To do so, the sample is mounted to a ramp ring, which is steered by three piezo elements (Fig. 7.3a,b). This procedure ensures that the alignment of an optical focus to the tip does not change during measurements – in particular, also for more tightly focused higher-frequency radiation. Moreover, a parabolic mirror with maximized numerical aperture on the STM body (Fig. 7.3a-c, dark red area) focusing ultrashort pulses onto the tip is movable by another set of piezo actuators (Fig. 7.3b). These changes have been implemented to facilitate optics-to-tip alignment and to minimize the need for frequent alignment increasing available measurement time. Moreover, the design of the parabolic mirror allows for coupling out scattered or emitted radiation from the tunnel junction (Fig. 7.3c) opening the doors for multi-messenger nanoscopy: By installing a cantilever or Q-plus sensor in the setup, LW-STM can be combined with SNOM [Eis14, Hub16, Pla21] or NOTE [Sid24] measurements.

To incorporate a magnetic field in a LW-STM, technical challenges are exceptionally demanding. We aim for a tunable magnetic field in ultrahigh vacuum, which can reach at least up to several tesla. Wave packet dynamics upon Zeeman splitting should take place on picosecond time scales. For a magnetic field of 3 T, the energy splitting for an electronic energy level amounts to $\mu_\mathrm{B} \cdot B \approx 0.2$ meV, which corresponds to a periodicity of 20 ps. Such time scales are detectable in a LW-STM.

Apart from the physical requirements posed on the magnetic field, also technical aspects need to be considered. To reach a magnetic field of several tesla, a superconducting coil can be employed, which resides in a helium bath or is cooled by a cryostat. Due to the need for optical access at the same time as constant cooling of the coil and permanent shielding from thermal radiation, only the latter option is practicable. Both solenoid and split-coil design are able to deliver homogeneous magnetic fields. Importantly, LW-STM measurements require optical access for coupling terahertz pulses into the STM junction. Moreover, a view port and mechanical access to the scan head for procedures such as sample transfer are mandatory. This is why a split-coil design is chosen. Still, the gaps for mechanical and optical access should be small enough to ensure a homogeneous magnetic field in the STM tunnel junction as well as mechanical stability.

To meet all the discussed physical and technical challenges, a cryostat including the magnetic coil has been designed by CryoVac fulfilling our demands (Fig. 7.4).

Figure 7.4 | Optical and mechanical access. a, From outside, one can see the scan head through a view port (center). A movable nitrogen shield (green) enables optical and mechanical procedures when necessary and prevents heating during STM operation. Inside the rotatable shield, a fixed nitrogen shield (purple) is installed. The helium-temperature shield (blue) visible in a cut (**b**) covers the superconducting coil. CAD drawings by courtesy of Christoph Rohrer.

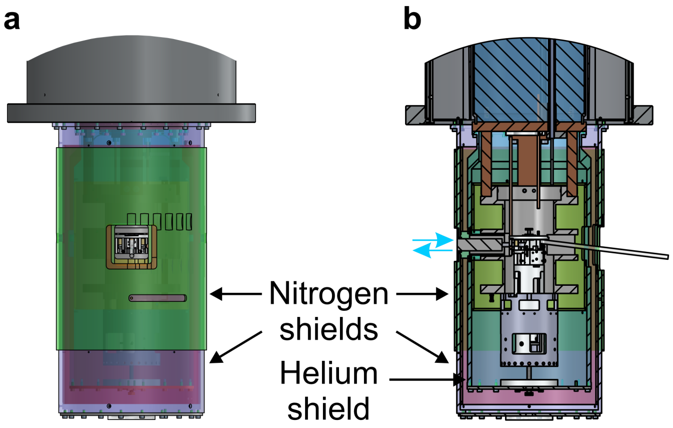

Shielding the superconducting coil from thermal radiation is achieved by placing it between a bulk body and a shield, which are both cooled by a helium cryostat. The same cryostat also cools the STM body (Fig. 7.4b). To further block thermal radiation from the helium shield, two shields, a rigid one and a rotatable one, cooled by a liquid-nitrogen cryostat are installed outside the helium shield separated by ultrahigh vacuum. The rotatable shield allows us to move windows for mechanical and optical access to enable measurement preparation or LW-STM measurements.

Current state and outlook. At present, the STM is built up and fully operational. The STM chamber reaches ultrahigh vacuum pressures of below 10^{-10} mbar. First samples have been prepared and first images have been taken on atomically flat Au(110) at cryogenic temperatures featuring a missing row reconstruction (Fig. 7.5). So far, the maximum field reached with the superconducting split coil has been 2.6 T. In a next step, spin-resolving measurements will be taken.

For the LW-STM including a magnetic field, a terahertz source designated for the existing machine has been developed, which can be operated at a repetition rate of 4 MHz [Mei22, Mei24]. The generated sub-half-cycle terahertz pulses (Fig. 7.6a) span a frequency range from 0.68 THz to 4.3 THz with a center frequency of 2.47 THz (Fig. 7.6b). They will be coupled to the STM junction via a sapphire window. For the option to couple higher-frequency radiation into and out of the junction, 1 mm

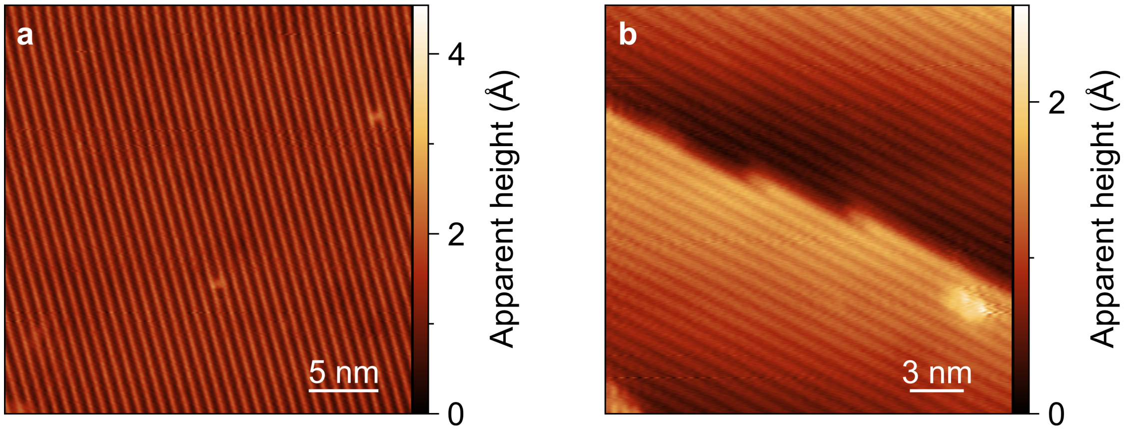

Figure 7.5 | STM scans of Au(110). Constant current scans of a Au(110) surface reveal a missing-row reconstruction of the Au(110) surface (**a**, $V = 0.3$ V, $I = 2.6 \times 10^{-10}$ A) as well as an atomic step of gold (**b**, $V = 2$V, $I = 2.6 \times 10^{-10}$ A). Measurement data by courtesy of Victoria Ruckerbauer and Andreas Rank.

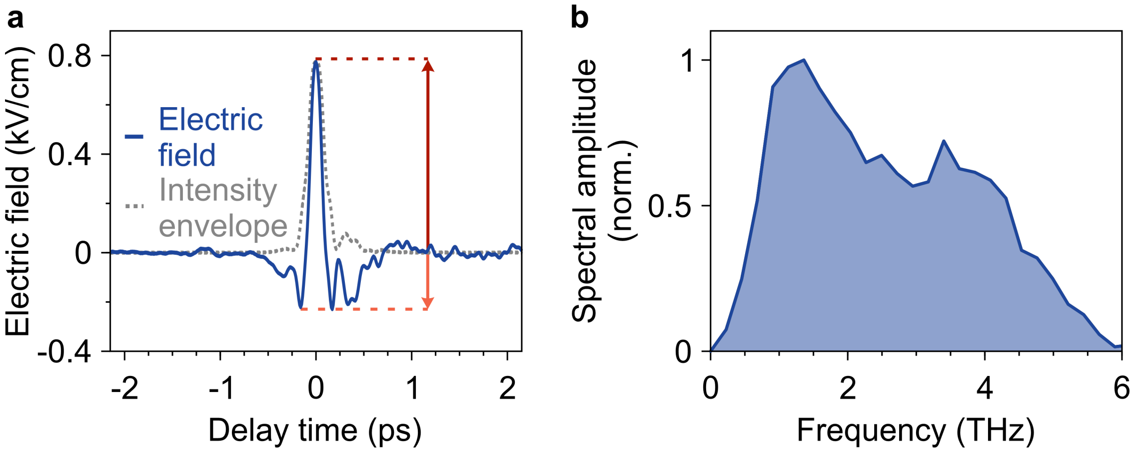

Figure 7.6 | Terahertz source developed for the magnetic-field LW-STM. **a**, The electric-field waveform detected by electro-optic sampling, corrected for the detector response, features a strongly asymmetric (red arrows) terahertz waveform. **b**, The spectral amplitude of the transient spans from 0.68 THz to 4.3 THz at its FWHM. This figure was adapted from [Mei24] with permission.

thick diamond windows are available and can be installed in the STM chamber.
In conclusion, both the STM and the terahertz setup are finalized such that in a next step we will couple the two home-built setups, optically accessible B-field STM and custom-tailored strongly sub-cycle terahertz pulses, to perform the envisioned experiments – to unravel dynamics driven by yet another degree of freedom, the electronic spin.

Chapter 8

Conclusion

> *Is life a journey?*
> *Whereto?*
> *Wherefrom?*
> *From the light*
> *– into the light.*
>
> — Alissa Rossius Dausgaard [RD21]

In this thesis, I have shown, how lightwave-driven scanning tunneling microscopy (LW-STM) and spectroscopy (LW-STS) are able to resolve ultrafast structural dynamics and their interplay with electronic energy levels, simultaneously in space, time and energy.

Based on scanning tunneling microscopy and spectroscopy (chapter 2), I introduced LW-STM and ultrafast action spectroscopy (chapter 3) as cornerstones of this thesis to trigger and observe intrinsic dynamics of the nanocosmos.
On the atomic scale, the motion of a single-molecule switch can be steered coherently by ultrafast atomic forces mediated by the electric field of a terahertz near-field waveform (chapter 4). The induced motion pattern efficiently modifies the switching probability of the molecular switch. We found that the amplitude of the excited motion critically depends on the exact position, where an electric field is applied. The electric field acts locally on specific hotspots of local polar interaction – key atoms

which are responsible for the adsorption energetics of the single-molecule switch. When locally applied to these hotspots, the motion pattern can be triggered and hence the switching probability can be modulated efficiently. In summary, with the terahertz electric near field, we are able to directly induce atomic motion and watch its impact in atomic-scale movies.

In chapter 5, the switching behavior of the molecule was exploited to quantitatively measure the atomically confined near-field waveform inside the junction of the STM. Making use of an interference scheme of a test and a gate terahertz pulse, we can resolve salient features of the test waveform. By comparing the measured near-field and far-field waveforms and their spectra, a frequency-dependent transfer function from far to near field was extracted. For 1 THz, we observe an enhancement of the field amplitude by $\sim 2 \times 10^5$ when coupled to the ångström-sized tip-sample junction. Our measurements together with a classical simulation open the door for a predictive design of nano-optics in the near-field regime.

Finally, the development of ultrafast time-resolved LW-STS allowed us to follow the temporal evolution of a select electronic energy level of a selenium vacancy in a monolayer WSe_2 (chapter 6). To this end, we have established a model-free ultrafast version of steady-state tunneling spectroscopy with atomic spatial, ~300 fs temporal and ~10 meV energy resolution. Upon excitation of a drum-like phonon mode in the monolayer, we record the transient local density of states for different phases of the oscillation. By extracting the energy level position of the defect state from the ultrafast spectra, we can observe how the vacancy state is transiently shifted by up to 40 meV. When we do this for different amplitudes of the structural motion, we can even link picometer-scale atomic displacements in space to a specific shift in energy. With the results showcasing the observation of evolving localized energy levels on ultrafast time scales directly on atomic length scales, we establish a new area of research, which complements spatially averaging techniques able to map out the band structure of materials. Lightwave-driven STM and STS give us direct access to the nanoscopic world driven by quantum mechanics.

Thanks to instrument development with an additional magnetic field in a LW-STM (chapter 7), we even envision ultrafast videography accessing yet another degree of freedom: the electronic spin. Moreover, by tuning energy levels with the magnetic field, we also plan to observe electronic wavepacket dynamics.

With our experimental results, the novel techniques developed as well as future experiments, we hope to trigger innovative exciting science – to understand, how the fundamental building blocks govern our world on the atomic level, to bring light into the dark.

Scientific record

Publications in peer-reviewed jounals

- Dominik Peller, Lukas Z. Kastner, Thomas Buchner, Carmen Roelcke, Florian Albrecht, Nikolaj Moll, Rupert Huber & Jascha Repp
  Sub-cycle atomic-scale forces coherently control a single-molecule switch
  Nature **585**, 58 (2020)| doi: 10.1038/s41586-020-2620-2

- Dominik Peller, Carmen Roelcke, Lukas Z. Kastner, Thomas Buchner, Alexander Neef, Johannes Hayes, Franco Bonafé, Dominik Sidler, Michael Ruggenthaler, Angel Rubio, Rupert Huber & Jascha Repp
  Quantitative sampling of atomic-scale electromagnetic waveforms
  Nature Photonics **15**, 143 (2021)| doi: 10.1038/s41566-020-00720-8

  ▶ Featured in a News and Views Article by Jun Takeda & Ikufumi Katayama
  Waveform sampling on an atomic scale
  Nature Photonics **15**, 70 (2021) | doi: 10.1038/s41566-020-00753-z

- Carmen Roelcke*, Lukas Z. Kastner*, Maximilian Graml, Andreas Biereder, Jan Wilhelm, Jascha Repp, Rupert Huber & Yaroslav A. Gerasimenko
  * equal contribution
  Ultrafast atomic-scale scanning tunnelling spectroscopy of a single vacancy in a monolayer crystal
  Nature Photonics **18**, 595 (2024)| doi: 10.1038/s41566-024-01390-6

  ▶ Coverstory

Publications in international conference proceedings

- Carmen Roelcke, Dominik Peller, Lukas Z. Kastner, Thomas Buchner, Alexander Neef, Johannes Hayes, Franco Bonafé, Dominik Sidler, Michael Ruggenthaler, Angel Rubio, Jascha Repp & Rupert Huber
  Quantitative Waveform Sampling on Atomic Scales
  Conference on Lasers and Electro-Optics, OSA Technical Digest (Optica Publishing Group, 2021), paper FTh1K.6 | doi: 10.1364/CLEO_QELS.2021.FTh1K.6

- Carmen Roelcke, Lukas Z. Kastner, Dominik Peller, Yaroslav A. Gerasimenko, Jascha Repp & Rupert Huber
  Controlling and videotaping single-molecule dynamics with atomically confined terahertz transients
  SPIE Optics + Photonics meeting 2023, 12683-30 (2023) | doi: 10.1117/12.2679989

Contributions at international conferences and seminars as presenting author

- **SPIE: Photonics West 2020**
  01-06 February 2020 | San Francisco, USA
  Invited talk

  Carmen Roelcke, Dominik Peller, Lukas Kastner, Thomas Buchner, Jascha Repp & Rupert Huber
  Femtosecond atomic forces coherently control a single-molecule switch

- **Conference on Lasers and Electro-Optics (CLEO) 2021**
  09-14 May 2021 | online
  Contributed talk

  Carmen Roelcke, Dominik Peller, Lukas Z. Kastner, Thomas Buchner, Alexander Neef, Johannes Hayes, Franco Bonafé, Dominik Sidler, Michael Ruggenthaler, Angel Rubio, Jascha Repp & Rupert Huber
  Quantitative Waveform Sampling on Atomic Scales

- **International Ultrafast Knowledge Coffee House**
  24 May 2021 | online
  Invited talk

  Carmen Roelcke, Dominik Peller, Lukas Z. Kastner, Thomas Buchner, Alexander Neef, Johannes Hayes, Franco Bonafé, Dominik Sidler, Michael Ruggenthaler, Angel Rubio, Jascha Repp & Rupert Huber
  Quantitative sampling of atom-scale near-field waveforms

- **CRC 1277: International Workshop 2021**
  22-24 September 2021 | Regensburg, Germany
  Contributed talk

  Carmen Roelcke, Dominik Peller, Lukas Z. Kastner, Thomas Buchner, Florian Albrecht, Nikolaj Moll, Alexander Neef, Johannes Hayes, Franco Bonafé, Dominik Sidler, Michael Ruggenthaler, Angel Rubio, Jascha Repp & Rupert Huber
  Atom-scale near-field transients steering single-molecule dynamics

- **PIPT7: Photoinduced Phase Transitions and Cooperative Phenomena 2021**
  8-17 November 2021 | online
  Poster

  Carmen Roelcke, Dominik Peller, Lukas Z. Kastner, Thomas Buchner, Florian Albrecht, Nikolaj Moll, Jascha Repp & Rupert Huber
  Femtosecond atomic forces coherently control a single-molecule switch

- **9th International Conference on Optical Terahertz Science and Technology (OTST 2022)**
  19-24 June 2022 | Budapest, Hungary
  Contributed talk

  Carmen Roelcke, Dominik Peller, Lukas Z. Kastner, Thomas Buchner, Alexander Neef, Johannes Hayes, Franco Bonafé, Dominik Sidler, Michael Ruggenthaler, Angel Rubio, Jascha Repp & Rupert Huber
  Quantitative Sampling of Terahertz waveforms on Atomic Scales

- **47th International Conference on Infrared, Millimeter and Terahertz Waves (IRMMW-THz 2022)**
  28 August - 02 September | Delft, Netherlands
  Contributed talk

  Carmen Roelcke, Dominik Peller, Lukas Z. Kastner, Thomas Buchner, Alexander Neef, Johannes Hayes, Franco Bonafé, Dominik Sidler, Michael Ruggenthaler, Angel Rubio, Jascha Repp & Rupert Huber
  Quantitative Sampling of Atom-Scale Terahertz Waveforms

- **CRC 1083 Workshop: Oragnic Interfaces and Orbital Tomography**
  06-07 March 2023 | Marburg, Germany
  Contributed talk

  Carmen Roelcke, Dominik Peller, Lukas Z. Kastner, Thomas Buchner, Alexander Neef, Nikolaj Moll, Franco Bonafé, Dominik Sidler, Angel Rubio, Jascha Repp & Rupert Huber
  Orbital videography and control of a dancing molecule on a surface

- **SPIE Optics + Photonics meeting 2023**
  20-24 August 2023 | San Diego, USA
  Invited talk

  Carmen Roelcke, Lukas Z. Kastner, Dominik Peller, Yaroslav A. Gerasimenko, Jascha Repp & Rupert Huber
  Controlling and videotaping single-molecule dynamics with atomically confined terahertz transients

- **10th International Conference on Optical Terahertz Science and Technology (OTST 2024)**
  08-12 April 2024 | Marburg, Germany
  Keynote talk

  Carmen Roelcke, Lukas Z. Kastner, Maximilian Graml, Andreas Biereder, Jan Wilhelm, Jascha Repp, Rupert Huber & Yaroslav A. Gerasimenko
  Ultrafast scanning tunnelling spectroscopy of an atomic vacancy in monolayer WSe_2

- **Inaugural Symposium of the Regensburg Center for Ultrafast Nanoscopy (2024)**
  06-08 May 2024 | Regensburg, Germany
  Poster

  Carmen Roelcke, Lukas Z. Kastner, Maximilian Graml, Andreas Biereder, Jan Wilhelm, Jascha Repp, Rupert Huber & Yaroslav A. Gerasimenko
  Ultrafast atomic-scale scanning tunnelling spectroscopy of a single vacancy in monolayer crystal

- **49th International Conference on Infrared, Millimeter and Terahertz Waves (IRMMW-THz 2024)**
  01-06 September 2024 | Perth, Australia
  Contributed talk

  Carmen Roelcke, Lukas Z. Kastner, Maximilian Graml, Andreas Biereder, Jan Wilhelm, Jascha Repp, Rupert Huber & Yaroslav A. Gerasimenko
  Ultrafast scanning tunnelling spectroscopy of an atomic vacancy in a monolayer crystal

Bibliography

[Abd21] M. Abdo, S. Sheng, S. Rolf-Pissarczyk, L. Arnhold, J. A. J. Burgess, M. Isobe, L. Malavolti, and S. Loth, *Variable Repetition Rate THz Source for Ultrafast Scanning Tunneling Microscopy*, ACS Photonics **8**, 702–708 (2021).

[Alb22] F. Albrecht, S. Fatayer, I. Pozo, I. Tavernelli, J. Repp, D. Peña, and L. Gross, *Selectivity in single-molecule reactions by tip-induced redox chemistry*, Science **377**, 298–301 (2022).

[Amm21] S. E. Ammerman, V. Jelic, Y. Wei, V. N. Breslin, M. Hassan, N. Everett, S. Lee, Q. Sun, C. A. Pignedoli, P. Ruffieux, R. Fasel, and T. L. Cocker, *Lightwave-driven scanning tunnelling spectroscopy of atomically precise graphene nanoribbons*, Nature Communications **12** (2021).

[Amm22] S. E. Ammerman, Y. Wei, N. Everett, V. Jelic, and T. L. Cocker, *Algorithm for subcycle terahertz scanning tunneling spectroscopy*, Physical Review B **105**, 115427 (2022).

[And21] E. Y. Andrei, D. K. Efetov, P. Jarillo-Herrero, A. H. MacDonald, K. F. Mak, T. Senthil, E. Tutuc, A. Yazdani, and A. F. Young, *The marvels of moiré materials*, Nature Reviews Materials **6**, 201–206 (2021).

[Ank08] J. N. Anker, W. P. Hall, O. Lyandres, N. C. Shah, J. Zhao, and R. P. Van Duyne, *Biosensing with plasmonic nanosensors*, Nature Materials **7**, 442–453 (2008).

[Ata18] M. Atatüre, D. Englund, N. Vamivakas, S.-Y. Lee, and J. Wrachtrup, *Material platforms for spin-based photonic quantum technologies*, Nature Reviews Materials **3**, 38–51 (2018).

[Atw10] H. A. Atwater and A. Polman, *Plasmonics for improved photovoltaic devices*, Nature Materials **9**, 205–213 (2010).

[Bal23] E. Baldini, A. Zong, D. Choi, C. Lee, M. H. Michael, L. Windgaetter, I. I. Mazin, S. Latini, D. Azoury, B. Lv, A. Kogar, Y. Su, Y. Wang, Y. Lu, T. Takayama, H. Takagi, A. J. Millis, A. Rubio, E. Demler, and N. Gedik, *The spontaneous symmetry breaking in* Ta_2NiSe_5 *is structural in nature*, Proceedings of the National Academy of Sciences **120** (2023).

[Bar61] J. Bardeen, *Tunnelling from a Many-Particle Point of View*, Physical Review Letters **6**, 57–59 (1961).

[Bar03] W. L. Barnes, A. Dereux, and T. W. Ebbesen, *Surface plasmon subwavelength optics*, Nature **424**, 824–830 (2003).

[Bar15] M. Barbry, P. Koval, F. Marchesin, R. Esteban, A. G. Borisov, J. Aizpurua, and D. Sánchez-Portal, *Atomistic Near-Field Nanoplasmonics: Reaching Atomic-Scale Resolution in Nanooptics*, Nano Letters **15**, 3410–3419 (2015).

[Bea96] E. Beaurepaire, J.-C. Merle, A. Daunois, and J.-Y. Bigot, *Ultrafast Spin Dynamics in Ferromagnetic Nickel*, Physical Review Letters **76**, 4250–4253 (1996).

[Bec15] A. Bechtold, D. Rauch, F. Li, T. Simmet, P.-L. Ardelt, A. Regler, K. Müller, N. A. Sinitsyn, and J. J. Finley, *Three-stage decoherence dynamics of an electron spin qubit in an optically active quantum dot*, Nature Physics **11**, 1005–1008 (2015).

[Ben16] F. Benz, M. K. Schmidt, A. Dreismann, R. Chikkaraddy, Y. Zhang, A. Demetriadou, C. Carnegie, H. Ohadi, B. de Nijs, R. Esteban, J. Aizpurua, and J. J. Baumberg, *Single-molecule optomechanics in "picocavities"*, Science **354**, 726–729 (2016).

[Bin82] G. Binnig, H. Rohrer, C. Gerber, and E. Weibel, *Surface Studies by Scanning Tunneling Microscopy*, Physical Review Letters **49**, 57–61 (1982).

[Bin83] G. Binnig and H. Rohrer, *Scanning tunneling microscopy*, Surface Science **126**, 236–244 (1983).

[Bin87] G. Binnig and H. Rohrer, *Scanning tunneling microscopy—from birth to adolescence*, Reviews of Modern Physics **59**, 615–625 (1987).

[Bob24a] L. Bobzien, J. Allerbeck, S. E. Ammerman, R. Torsi, J. A. Robinson, and B. Schuler, *Ultrafast state-selective tunneling in two-dimensional semiconductors with a phase- and amplitude-controlled THz-scanning tunneling microscope*, APL Materials **12** (2024).

[Bob24b] L. Bobzien, J. Allerbeck, N. Krane, A. Ortega-Guerrero, Z. Wang, D. E. C. Figueroa, C. Dong, C. A. Pignedoli, J. A. Robinson, and B. Schuler, *Layer-Dependent Charge State Lifetime of Single Se Vacancies in* WSe_2.

[Bor10] R. Bormann, M. Gulde, A. Weismann, S. V. Yalunin, and C. Ropers, *Tip-Enhanced Strong-Field Photoemission*, Physical Review Letters **105**, 147601 (2010).

[Bor23] M. Borsch, M. Meierhofer, R. Huber, and M. Kira, *Lightwave electronics in condensed matter*, Nature Reviews Materials **8**, 668–687 (2023).

[Bra00] T. Brabec and F. Krausz, *Intense few-cycle laser fields: Frontiers of nonlinear optics*, Reviews of Modern Physics **72**, 545–591 (2000).

[Buc24] T. Buchner, *Atomic scale light-matter interaction: From ultrafast physics to photoexcitation phenomena*, PhD thesis (2024).

[Bö19] H. Böckmann, M. Müller, A. Hammud, M.-G. Willinger, M. Pszona, J. Waluk, M. Wolf, and T. Kumagai, *Near-Field Spectral Response of Optically Excited Scanning Tunneling Microscope Junctions Probed by Single-Molecule Action Spectroscopy*, The Journal of Physical Chemistry Letters **10**, 2068–2074 (2019).

[CG14] A. Castellanos-Gomez, M. Buscema, R. Molenaar, V. Singh, L. Janssen, H. S. J. van der Zant, and G. A. Steele, *Deterministic transfer of two-dimensional materials by all-dry viscoelastic stamping*, 2D Materials **1**, 011002 (2014).

[Cha15] C. Chakraborty, L. Kinnischtzke, K. M. Goodfellow, R. Beams, and A. N. Vamivakas, *Voltage-controlled quantum light from an atomically thin semiconductor*, Nature Nanotechnology **10**, 507–511 (2015).

[Che07] C. J. Chen, *Introduction to Scanning Tunneling Microscopy*, Oxford University PressOxford (2007).

[Chr12] P. Christopher, H. Xin, A. Marimuthu, and S. Linic, *Singular characteristics and unique chemical bond activation mechanisms of photocatalytic reactions on plasmonic nanostructures*, Nature Materials **11**, 1044–1050 (2012).

[Cia17] M. F. Ciappina, J. A. Pérez-Hernández, A. S. Landsman, W. A. Okell, S. Zherebtsov, B. Förg, J. Schötz, L. Seiffert, T. Fennel, T. Shaaran, T. Zimmermann, A. Chacón, R. Guichard, A. Zaïr, J. W. G. Tisch, J. P. Marangos, T. Witting, A. Braun, S. A. Maier, L. Roso, M. Krüger, P. Hommelhoff, M. F. Kling, F. Krausz, and M. Lewenstein, *Attosecond physics at the nanoscale*, Reports on Progress in Physics **80**, 054401 (2017).

[Coc13] T. L. Cocker, V. Jelic, M. Gupta, S. J. Molesky, J. A. J. Burgess, G. D. L. Reyes, L. V. Titova, Y. Y. Tsui, M. R. Freeman, and F. A. Hegmann, *An ultrafast terahertz scanning tunnelling microscope*, Nature Photonics **7**, 620–625 (2013).

[Coc16] T. L. Cocker, D. Peller, P. Yu, J. Repp, and R. Huber, *Tracking the ultrafast motion of a single molecule by femtosecond orbital imaging*, Nature **539**, 263–267 (2016).

[Coc21] K. A. Cochrane, J.-H. Lee, C. Kastl, J. B. Haber, T. Zhang, A. Kozhakhmetov, J. A. Robinson, M. Terrones, J. Repp, J. B. Neaton, A. Weber-

Bargioni, and B. Schuler, *Spin-dependent vibronic response of a carbon radical ion in two-dimensional WS_2*, Nature Communications **12** (2021).

[Col11] J. N. Coleman, M. Lotya, A. O'Neill, S. D. Bergin, P. J. King, U. Khan, K. Young, A. Gaucher, S. De, R. J. Smith, I. V. Shvets, S. K. Arora, G. Stanton, H.-Y. Kim, K. Lee, G. T. Kim, G. S. Duesberg, T. Hallam, J. J. Boland, J. J. Wang, J. F. Donegan, J. C. Grunlan, G. Moriarty, A. Shmeliov, R. J. Nicholls, J. M. Perkins, E. M. Grieveson, K. Theuwissen, D. W. McComb, P. D. Nellist, and V. Nicolosi, *Two-Dimensional Nanosheets Produced by Liquid Exfoliation of Layered Materials*, Science **331**, 568–571 (2011).

[Dav20] T. J. Davis, D. Janoschka, P. Dreher, B. Frank, F.-J. Meyer zu Heringdorf, and H. Giessen, *Ultrafast vector imaging of plasmonic skyrmion dynamics with deep subwavelength resolution*, Science **368** (2020).

[Del98] N. B. Delone and V. P. Krainov, *REVIEWS OF TOPICAL PROBLEMS: Tunneling and barrier-suppression ionization of atoms and ions in a laser radiation field*, Physics Uspekhi **41**, 469-485 (1998).

[DeR91] J. DeRose, T. Thundat, L. Nagahara, and S. Lindsay, *Gold grown epitaxially on mica: conditions for large area flat faces*, Surface Science **256**, 102–108 (1991).

[Dhi17] S. S. Dhillon, M. S. Vitiello, E. H. Linfield, A. G. Davies, M. C. Hoffmann, J. Booske, C. Paoloni, M. Gensch, P. Weightman, G. P. Williams, E. Castro-Camus, D. R. S. Cumming, F. Simoens, I. Escorcia-Carranza, J. Grant, S. Lucyszyn, M. Kuwata-Gonokami, K. Konishi, M. Koch, C. A. Schmuttenmaer, T. L. Cocker, R. Huber, A. G. Markelz, Z. D. Taylor, V. P. Wallace, J. Axel Zeitler, J. Sibik, T. M. Korter, B. Ellison, S. Rea, P. Goldsmith, K. B. Cooper, R. Appleby, D. Pardo, P. G. Huggard, V. Krozer, H. Shams, M. Fice, C. Renaud, A. Seeds, A. Stöhr, M. Naftaly, N. Ridler, R. Clarke, J. E. Cunningham, and M. B. Johnston, *The 2017 terahertz science and technology roadmap*, Journal of Physics D: Applied Physics **50**, 043001 (2017).

[Dol11] A. Dolocan, D. P. Acharya, P. Zahl, P. Sutter, and N. Camillone, *Two-Color Ultrafast Photoexcited Scanning Tunneling Microscopy*, The Journal of Physical Chemistry C **115**, 10033–10043 (2011).

[Dop18] B. Doppagne, M. C. Chong, H. Bulou, A. Boeglin, F. Scheurer, and G. Schull, *Electrofluorochromism at the single-molecule level*, Science **361**, 251–255 (2018).

[Efr82] B. Efron, *The Jacknife, the Bootstrap and Other Resampling Plans*, Society for Industrial and Applied Mathematics.

[Eis14] M. Eisele, T. L. Cocker, M. A. Huber, M. Plankl, L. Viti, D. Ercolani, L. Sorba, M. S. Vitiello, and R. Huber, *Ultrafast multi-terahertz nano-spectroscopy with sub-cycle temporal resolution*, Nature Photonics **8**, 841–845 (2014).

[Esa18] T. Esat, N. Friedrich, F. S. Tautz, and R. Temirov, *A standing molecule as a single-electron field emitter*, Nature **558**, 573–576 (2018).

[Fee20] R. M. Feenstra, G. R. Frazier, Y. Pan, S. Fölsch, Y.-C. Lin, B. Jariwala, K. Zhang, and J. A. Robinson, *Acquisition and analysis of scanning tunneling spectroscopy data—*WSe_2 *monolayer*, Journal of Vacuum Science & Technology A: Vacuum, Surfaces, and Films **39** (2020).

[Fei17] A. Feist, N. Bach, N. Rubiano da Silva, T. Danz, M. Möller, K. E. Priebe, T. Domröse, J. G. Gatzmann, S. Rost, J. Schauss, S. Strauch, R. Bormann, M. Sivis, S. Schäfer, and C. Ropers, *Ultrafast transmission electron microscopy using a laser-driven field emitter: Femtosecond resolution with a high coherence electron beam*, Ultramicroscopy **176**, 63–73 (2017).

[Fer88] M. Ferray, A. L'Huillier, X. F. Li, L. A. Lompre, G. Mainfray, and C. Manus, *Multiple-harmonic conversion of 1064 nm radiation in rare gases*, Journal of Physics B: Atomic, Molecular and Optical Physics **21**, L31–L35 (1988).

[Fer13] A. Fert, V. Cros, and J. Sampaio, *Skyrmions on the track*, Nature Nanotechnology **8**, 152–156 (2013).

[Fra21] M. Frankerl and A. Donarini, *Spin-orbit interaction induces charge beatings in a lightwave-STM – single molecule junction*, Physical Review B **103**, 085420 (2021).

[Fre22] J. Freudenstein, M. Borsch, M. Meierhofer, D. Afanasiev, C. P. Schmid, F. Sandner, M. Liebich, A. Girnghuber, M. Knorr, M. Kira, and R. Huber, *Attosecond clocking of correlations between Bloch electrons*, Nature **610**, 290–295 (2022).

[Gal99] G. Gallot and D. Grischkowsky, *Electro-optic detection of terahertz radiation*, Journal of the Optical Society of America B **16**, 1204 (1999).

[Gei13] A. K. Geim and I. V. Grigorieva, *Van der Waals heterostructures*, Nature **499**, 419–425 (2013).

[Geo18] R. S. Geonmonond, A. G. M. da Silva, T. S. Rodrigues, I. C. de Freitas, R. A. Ando, T. V. Alves, and P. H. C. Camargo, *Addressing the Effects of Size-dependent Absorption, Scattering, and Near-field Enhancements in Plasmonic Catalysis*, ChemCatChem **10**, 3447–3452 (2018).

[Goe98] J. W. Goethe, *The Poems of Goethe, Translated in the Original Metres*, Translation: E. A. Bowring, Urbana, Illinois: Project Gutenberg (1998), Retrieved October 20, 2024 from https://www.gutenberg.org/ebooks/1287.

[Gou07] E. Goulielmakis, V. S. Yakovlev, A. L. Cavalieri, M. Uiberacker, V. Pervak, A. Apolonski, R. Kienberger, U. Kleineberg, and F. Krausz, *Attosecond Control and Measurement: Lightwave Electronics*, Science **317**, 769–775 (2007).

[Gri06] M. S. Grinolds, V. A. Lobastov, J. Weissenrieder, and A. H. Zewail, *Four-dimensional ultrafast electron microscopy of phase transitions*, Proceedings of the National Academy of Sciences **103**, 18427–18431 (2006).

[Gro96] R. H. M. Groeneveld and H. van Kempen, *The capacitive origin of the picosecond electrical transients detected by a photoconductively gated* *scanning tunneling microscope*, Applied Physics Letters **69**, 2294–2296 (1996).

[Guo21] H. Guo, X. Zhang, and G. Lu, *Moiré excitons in defective van der Waals heterostructures*, Proceedings of the National Academy of Sciences **118** (2021).

[Gü99] J. Güdde, U. Conrad, V. Jähnke, J. Hohlfeld, and E. Matthias, *Magnetization dynamics of Ni and Co films on Cu(001) and of bulk nickel surfaces*, Physical Review B **59**, R6608–R6611 (1999).

[Ham86] R. J. Hamers, R. M. Tromp, and J. E. Demuth, *Surface Electronic Structure of Si(111)-(7×7) Resolved in Real Space*, Physical Review Letters **56**, 1972–1975 (1986).

[Ham87] R. Hamers, R. Tromp, and J. Demuth, *Electronic and geometric structure of Si(111)-(7 × 7) and Si(001) surfaces*, Surface Science **181**, 346–355 (1987).

[Ham90] R. J. Hamers and D. G. Cahill, *Ultrafast time resolution in scanned probe microscopies*, Applied Physics Letters **57**, 2031–2033 (1990).

[Han87] P. K. Hansma and J. Tersoff, *Scanning tunneling microscopy*, Journal of Applied Physics **61**, R1–R24 (1987).

[He15] Y.-M. He, G. Clark, J. R. Schaibley, Y. He, M.-C. Chen, Y.-J. Wei, X. Ding, Q. Zhang, W. Yao, X. Xu, C.-Y. Lu, and J.-W. Pan, *Single quantum emitters in monolayer semiconductors*, Nature Nanotechnology **10**, 497–502 (2015).

[Hei11] S. Heinze, K. von Bergmann, M. Menzel, J. Brede, A. Kubetzka, R. Wiesendanger, G. Bihlmayer, and S. Blügel, *Spontaneous atomic-scale magnetic skyrmion lattice in two dimensions*, Nature Physics **7**, 713–718 (2011).

[Hen01] M. Hentschel, R. Kienberger, C. Spielmann, G. A. Reider, N. Milosevic, T. Brabec, P. Corkum, U. Heinzmann, M. Drescher, and F. Krausz, *Attosecond metrology*, Nature **414**, 509–513 (2001).

[Her12] G. Herink, D. R. Solli, M. Gulde, and C. Ropers, *Field-driven photoemission from nanostructures quenches the quiver motion*, Nature **483**, 190–193 (2012).

[Her14] G. Herink, L. Wimmer, and C. Ropers, *Field emission at terahertz frequencies: AC-tunneling and ultrafast carrier dynamics*, New Journal of Physics **16**, 123005 (2014).

[Hes16] H. Hesse, *Siddhartha*, 67 ed., Suhrkamp Taschenbuch, no. 182, Suhrkamp (2016).

[Hla00] S.-W. Hla, L. Bartels, G. Meyer, and K.-H. Rieder, *Inducing All Steps of a Chemical Reaction with the Scanning Tunneling Microscope Tip: Towards Single Molecule Engineering*, Physical Review Letters **85**, 2777–2780 (2000).

[Hoh97] J. Hohlfeld, E. Matthias, R. Knorren, and K. H. Bennemann, *Nonequilibrium Magnetization Dynamics of Nickel*, Physical Review Letters **78**, 4861–4864 (1997).

[Hom06a] P. Hommelhoff, C. Kealhofer, and M. A. Kasevich, *Ultrafast Electron Pulses from a Tungsten Tip Triggered by Low-Power Femtosecond Laser Pulses*, Physical Review Letters **97**, 247402 (2006).

[Hom06b] P. Hommelhoff, Y. Sortais, A. Aghajani-Talesh, and M. A. Kasevich, *Field Emission Tip as a Nanometer Source of Free Electron Femtosecond Pulses*, Physical Review Letters **96**, 077401 (2006).

[Hon15] J. Hong, Z. Hu, M. Probert, K. Li, D. Lv, X. Yang, L. Gu, N. Mao, Q. Feng, L. Xie, J. Zhang, D. Wu, Z. Zhang, C. Jin, W. Ji, X. Zhang, J. Yuan, and Z. Zhang, *Exploring atomic defects in molybdenum disulphide monolayers*, Nature Communications **6** (2015).

[Hsu17] P.-J. Hsu, A. Kubetzka, A. Finco, N. Romming, K. von Bergmann, and R. Wiesendanger, *Electric-field-driven switching of individual magnetic skyrmions*, Nature Nanotechnology **12**, 123–126 (2017).

[Hub98] R. Huber, M. Koch, and J. Feldmann, *Laser-induced thermal expansion of a scanning tunneling microscope tip measured with an atomic force microscope cantilever*, Applied Physics Letters **73**, 2521–2523 (1998).

[Hub00] R. Huber, A. Brodschelm, F. Tauser, and A. Leitenstorfer, *Generation and field-resolved detection of femtosecond electromagnetic pulses tunable up to 41 THz*, Applied Physics Letters **76**, 3191–3193 (2000).

[Hub16] M. A. Huber, F. Mooshammer, M. Plankl, L. Viti, F. Sandner, L. Z. Kastner, T. Frank, J. Fabian, M. S. Vitiello, T. L. Cocker, and R. Huber, *Femtosecond photo-switching of interface polaritons in black phosphorus heterostructures*, Nature Nanotechnology **12**, 207–211 (2016).

[Ima16] H. Imada, K. Miwa, M. Imai-Imada, S. Kawahara, K. Kimura, and Y. Kim, *Real-space investigation of energy transfer in heterogeneous molecular dimers*, Nature **538**, 364–367 (2016).

[Ino01] J. Inoue, K. Fukui, T. Kubo, S. Nakazawa, K. Sato, D. Shiomi, Y. Morita, K. Yamamoto, T. Takui, and K. Nakasuji, *The First Detection of a Clar's Hydrocarbon, 2,6,10-Tri-tert-Butyltriangulene: A Ground-State Triplet of Non-Kekulé Polynuclear Benzenoid Hydrocarbon*, Journal of the American Chemical Society **123**, 12702–12703 (2001).

[Ito23] S. Ito, M. Schüler, M. Meierhofer, S. Schlauderer, J. Freudenstein, J. Reimann, D. Afanasiev, K. A. Kokh, O. E. Tereshchenko, J. Güdde, M. A. Sentef, U. Höfer, and R. Huber, *Build-up and dephasing of Floquet–Bloch bands on subcycle timescales*, Nature **616**, 696–701 (2023).

[Jah15] J. Jahng, J. Brocious, D. A. Fishman, S. Yampolsky, D. Nowak, F. Huang, V. A. Apkarian, H. K. Wickramasinghe, and E. O. Potma, *Ultrafast pump-probe force microscopy with nanoscale resolution*, Applied Physics Letters **106** (2015).

[Jel17] V. Jelic, K. Iwaszczuk, P. H. Nguyen, C. Rathje, G. J. Hornig, H. M. Sharum, J. R. Hoffman, M. R. Freeman, and F. A. Hegmann, *Ultrafast terahertz control of extreme tunnel currents through single atoms on a silicon surface*, Nature Physics **13**, 591–598 (2017).

[Jel24] V. Jelic, S. Adams, M. Hassan, K. Cleland-Host, S. E. Ammerman, and T. L. Cocker, *Atomic-scale terahertz time-domain spectroscopy*, Nature Photonics **18**, 898–904 (2024).

[Jes19] R. Jestädt, M. Ruggenthaler, M. J. T. Oliveira, A. Rubio, and H. Appel, *Light-matter interactions within the Ehrenfest–Maxwell–Pauli–Kohn–Sham framework: fundamentals, implementation, and nano-optical applications*, Advances in Physics **68**, 225–333 (2019).

[Kan09] J. H. Kang, D. S. Kim, and Q.-H. Park, *Local Capacitor Model for Plasmonic Electric Field Enhancement*, Physical Review Letters **102**, 093906 (2009).

[Kar22] O. Karni, E. Barré, V. Pareek, J. D. Georgaras, M. K. L. Man, C. Sahoo, D. R. Bacon, X. Zhu, H. B. Ribeiro, A. L. O'Beirne, J. Hu, A. Al-Mahboob, M. M. M. Abdelrasoul, N. S. Chan, A. Karmakar, A. J. Winchester, B. Kim, K. Watanabe, T. Taniguchi, K. Barmak, J. Madéo, F. H. da Jornada, T. F. Heinz, and K. M. Dani, *Structure of the moiré exciton captured by imaging its electron and hole*, Nature **603**, 247–252 (2022).

[Kei90] S. R. Keiding and D. Grischkowsky, *Measurements of the phase shift and reshaping of terahertz pulses due to total internal reflection*, Optics Letters **15**, 48 (1990).

[Kel64] L. V. Keldysh, *Ionization in the field of a strong electromagnetic wave*, Zh. Eksperim. i Teor. Fiz. **47** (1964).

[Kem07] U. Kemiktarak, T. Ndukum, K. C. Schwab, and K. L. Ekinci, *Radio-frequency scanning tunnelling microscopy*, Nature **450**, 85–88 (2007).

[Ken21] D. M. Kennes, M. Claassen, L. Xian, A. Georges, A. J. Millis, J. Hone, C. R. Dean, D. N. Basov, A. N. Pasupathy, and A. Rubio, *Moiré heterostructures as a condensed-matter quantum simulator*, Nature Physics **17**, 155–163 (2021).

[Kha16] N. Kharche and V. Meunier, *Width and Crystal Orientation Dependent Band Gap Renormalization in Substrate-Supported Graphene Nanoribbons*, The Journal of Physical Chemistry Letters **7**, 1526–1533 (2016).

[Kle19] J. Klein, M. Lorke, M. Florian, F. Sigger, L. Sigl, S. Rey, J. Wierzbowski, J. Cerne, K. Müller, E. Mitterreiter, P. Zimmermann, T. Taniguchi, K. Watanabe, U. Wurstbauer, M. Kaniber, M. Knap, R. Schmidt, J. J. Finley, and A. W. Holleitner, *Site-selectively generated photon emitters in monolayer* MoS_2 *via local helium ion irradiation*, Nature Communications **10** (2019).

[Klu05] A. Klug, *Interview on Rosalind Franklin*, CSHL (2005), Retrieved October 20, 2024 from https://library.cshl.edu/oralhistory/interview/scientific-experience/women-science/aaron-rosalind-franklin/.

[Krü11] M. Krüger, M. Schenk, and P. Hommelhoff, *Attosecond control of electrons emitted from a nanoscale metal tip*, Nature **475**, 78–81 (2011).

[Lan16] F. Langer, M. Hohenleutner, C. P. Schmid, C. Poellmann, P. Nagler, T. Korn, C. Schüller, M. S. Sherwin, U. Huttner, J. T. Steiner, S. W. Koch, M. Kira, and R. Huber, *Lightwave-driven quasiparticle collisions on a subcycle timescale*, Nature **533**, 225–229 (2016).

[Lee19] J. Lee, K. T. Crampton, N. Tallarida, and V. A. Apkarian, *Visualizing vibrational normal modes of a single molecule with atomically confined light*, Nature **568**, 78–82 (2019).

[Lei23] A. Leitenstorfer, A. S. Moskalenko, T. Kampfrath, J. Kono, E. Castro-Camus, K. Peng, N. Qureshi, D. Turchinovich, K. Tanaka, A. G. Markelz, M. Havenith, C. Hough, H. J. Joyce, W. J. Padilla, B. Zhou, K.-Y. Kim, X.-C. Zhang, P. U. Jepsen, S. Dhillon, M. Vitiello, E. Linfield, A. G. Davies, M. C. Hoffmann, R. Lewis, M. Tonouchi, P. Klarskov, T. S. Seifert, Y. A. Gerasimenko, D. Mihailovic, R. Huber, J. L. Boland, O. Mitrofanov, P. Dean, B. N. Ellison, P. G. Huggard, S. P. Rea, C. Walker, D. T. Leisawitz, J. R. Gao, C. Li, Q. Chen, G. Valušis, V. P. Wallace, E. Pickwell-MacPherson, X. Shang, J. Hesler, N. Ridler, C. C. Renaud,

I. Kallfass, T. Nagatsuma, J. A. Zeitler, D. Arnone, M. B. Johnston, and J. Cunningham, *The 2023 terahertz science and technology roadmap*, Journal of Physics D: Applied Physics **56**, 223001 (2023).

[LH21] J. Lloyd-Hughes, P. M. Oppeneer, T. Pereira dos Santos, A. Schleife, S. Meng, M. A. Sentef, M. Ruggenthaler, A. Rubio, I. Radu, M. Murnane, X. Shi, H. Kapteyn, B. Stadtmüller, K. M. Dani, F. H. da Jornada, E. Prinz, M. Aeschlimann, R. L. Milot, M. Burdanova, J. Boland, T. Cocker, and F. Hegmann, *The 2021 ultrafast spectroscopic probes of condensed matter roadmap*, Journal of Physics: Condensed Matter **33**, 353001 (2021).

[Li11] G. Li, A. Luican, and E. Y. Andrei, *Self-navigation of a scanning tunneling microscope tip toward a micron-sized graphene sample*, Review of Scientific Instruments **82** (2011).

[Li15] H. Li, C. Tsai, A. L. Koh, L. Cai, A. W. Contryman, A. H. Fragapane, J. Zhao, H. S. Han, H. C. Manoharan, F. Abild-Pedersen, J. K. Nørskov, and X. Zheng, *Activating and optimizing MoS_2 basal planes for hydrogen evolution through the formation of strained sulphur vacancies*, Nature Materials **15**, 48–53 (2015).

[Li17] S. Li, S. Chen, J. Li, R. Wu, and W. Ho, *Joint Space-Time Coherent Vibration Driven Conformational Transitions in a Single Molecule*, Physical Review Letters **119**, 176002 (2017).

[Li24] H. Li, Z. Xiang, E. Regan, W. Zhao, R. Sailus, R. Banerjee, T. Taniguchi, K. Watanabe, S. Tongay, A. Zettl, M. F. Crommie, and F. Wang, *Mapping charge excitations in generalized Wigner crystals*, Nature Nanotechnology (2024).

[Lil07] P. Liljeroth, J. Repp, and G. Meyer, *Current-Induced Hydrogen Tautomerization and Conductance Switching of Naphthalocyanine Molecules*, Science **317**, 1203–1206 (2007).

[Liu22] S. Liu, A. Hammud, I. Hamada, M. Wolf, M. Müller, and T. Kumagai, *Nanoscale coherent phonon spectroscopy*, Science Advances **8** (2022).

[Lot10] S. Loth, M. Etzkorn, C. P. Lutz, D. M. Eigler, and A. J. Heinrich, *Measurement of Fast Electron Spin Relaxation Times with Atomic Resolution*, Science **329**, 1628–1630 (2010).

[Lyo17] T. Lyon, J. Sichau, A. Dorn, A. Centeno, A. Pesquera, A. Zurutuza, and R. Blick, *Probing Electron Spin Resonance in Monolayer Graphene*, Physical Review Letters **119**, 066802 (2017).

[Mak22] K. F. Mak and J. Shan, *Semiconductor moiré materials*, Nature Nanotechnology **17**, 686–695 (2022).

[Man15] A. Manchon, H. C. Koo, J. Nitta, S. M. Frolov, and R. A. Duine, *New perspectives for Rashba spin–orbit coupling*, Nature Materials **14**, 871–882 (2015).

[McP87] A. McPherson, G. Gibson, H. Jara, U. Johann, T. S. Luk, I. A. McIntyre, K. Boyer, and C. K. Rhodes, *Studies of multiphoton production of vacuum-ultraviolet radiation in the rare gases*, Journal of the Optical Society of America B **4**, 595 (1987).

[Mei22] C. Meineke, M. Prager, J. Hayes, Q. Wen, L. Z. Kastner, D. Schuh, K. Fritsch, O. Pronin, M. Stein, F. Schäfer, S. Chatterjee, M. Kira, R. Huber, and D. Bougeard, *Scalable high-repetition-rate sub-half-cycle terahertz pulses from spatially indirect interband transitions*, Light: Science & Applications **11** (2022).

[Mei24] C. H. Meineke, *From ultrafast electronic dynamics in 2D materials towards spin-resolved atom-scale videography*, PhD thesis (2024).

[Mer19] P. Merkl, F. Mooshammer, P. Steinleitner, A. Girnghuber, K.-Q. Lin, P. Nagler, J. Holler, C. Schüller, J. M. Lupton, T. Korn, S. Ovesen, S. Brem, E. Malic, and R. Huber, *Ultrafast transition between exciton phases in van der Waals heterostructures*, Nature Materials **18**, 691–696 (2019).

[Mid11] K. Midorikawa, *High-Order Harmonic Generation and Attosecond Science*, Japanese Journal of Applied Physics **50**, 090001 (2011).

[Mis20] S. Mishra, D. Beyer, K. Eimre, S. Kezilebieke, R. Berger, O. Gröning, C. A. Pignedoli, K. Müllen, P. Liljeroth, P. Ruffieux, X. Feng, and R. Fasel, *Topological frustration induces unconventional magnetism in a nanographene*, Nature Nanotechnology **15**, 22–28 (2020).

[Mis22] S. Mishra, S. Fatayer, S. Fernández, K. Kaiser, D. Peña, and L. Gross, *Nonbenzenoid High-Spin Polycyclic Hydrocarbons Generated by Atom Manipulation*, ACS Nano **16**, 3264–3271 (2022).

[Miw16] K. Miwa, H. Imada, S. Kawahara, and Y. Kim, *Effects of molecule-insulator interaction on geometric property of a single phthalocyanine molecule adsorbed on an ultrathin NaCl film*, Physical Review B **93**, 165419 (2016).

[Mom11] K. Momma and F. Izumi, *VESTA 3for three-dimensional visualization of crystal, volumetric and morphology data*, Journal of Applied Crystallography **44**, 1272–1276 (2011).

[Mou11] I. Moult, M. Herve, and Y. Pennec, *Ultrafast spectroscopy with a scanning tunneling microscope*, Applied Physics Letters **98** (2011).

[MS22] N. Martín Sabanés, F. Krecinic, T. Kumagai, F. Schulz, M. Wolf, and M. Müller, *Femtosecond Thermal and Nonthermal Hot Electron Tunneling Inside a Photoexcited Tunnel Junction*, ACS Nano **16**, 14479–14489 (2022).

[Mü20] M. Müller, N. Martín Sabanés, T. Kampfrath, and M. Wolf, *Phase-Resolved Detection of Ultrabroadband THz Pulses inside a Scanning Tunneling Microscope Junction*, ACS Photonics **7**, 2046–2055 (2020).

[Nag13] N. Nagaosa and Y. Tokura, *Topological properties and dynamics of magnetic skyrmions*, Nature Nanotechnology **8**, 899–911 (2013).

[Nai22] M. H. Naik, E. C. Regan, Z. Zhang, Y.-H. Chan, Z. Li, D. Wang, Y. Yoon, C. S. Ong, W. Zhao, S. Zhao, M. I. B. Utama, B. Gao, X. Wei, M. Sayyad, K. Yumigeta, K. Watanabe, T. Taniguchi, S. Tongay, F. H. da Jornada, F. Wang, and S. G. Louie, *Intralayer charge-transfer moiré excitons in van der Waals superlattices*, Nature **609**, 52–57 (2022).

[Nea06] J. B. Neaton, M. S. Hybertsen, and S. G. Louie, *Renormalization of Molecular Electronic Levels at Metal-Molecule Interfaces*, Physical Review Letters **97**, 216405 (2006).

[Nee18] A. Neef, *Master thesis: Simulating ultrashort light pulses in STM tunnel junctions*, University of Regensburg (2018).

[Nun93] G. Nunes and M. R. Freeman, *Picosecond Resolution in Scanning Tunneling Microscopy*, Science **262**, 1029–1032 (1993).

[O'B09] J. L. O'Brien, A. Furusawa, and J. Vučković, *Photonic quantum technologies*, Nature Photonics **3**, 687–695 (2009).

[Oga15] N. Ogawa, S. Seki, and Y. Tokura, *Ultrafast optical excitation of magnetic skyrmions*, Scientific Reports **5** (2015).

[Ovc78] A. A. Ovchinnikov, *Multiplicity of the ground state of large alternant organic molecules with conjugated bonds (Do Organic Ferromagnetics Exist?)*, Theoretica Chimica Acta **47**, 297–304 (1978).

[Par24] V. Pareek, D. R. Bacon, X. Zhu, Y.-H. Chan, F. Bussolotti, N. S. Chan, J. P. Urquizo, K. Watanabe, T. Taniguchi, M. K. L. Man, J. Madéo, D. Y. Qiu, K. E. J. Goh, F. H. da Jornada, and K. M. Dani, *Driving non-trivial quantum phases in conventional semiconductors with intense excitonic fields*.

[Pat19a] L. L. Patera, F. Queck, P. Scheuerer, N. Moll, and J. Repp, *Accessing a Charged Intermediate State Involved in the Excitation of Single Molecules*, Physical Review Letters **123**, 016001 (2019).

[Pat19b] L. L. Patera, F. Queck, P. Scheuerer, and J. Repp, *Mapping orbital changes upon electron transfer with tunnelling microscopy on insulators*, Nature **566**, 245–248 (2019).

[Pau01] P. M. Paul, E. S. Toma, P. Breger, G. Mullot, F. Augé, P. Balcou, H. G. Muller, and P. Agostini, *Observation of a Train of Attosecond Pulses from High Harmonic Generation*, Science **292**, 1689–1692 (2001).

[Pav17] N. Pavliček, A. Mistry, Z. Majzik, N. Moll, G. Meyer, D. J. Fox, and L. Gross, *Synthesis and characterization of triangulene*, Nature Nanotechnology **12**, 308–311 (2017).

[Pel20] D. Peller, L. Z. Kastner, T. Buchner, C. Roelcke, F. Albrecht, N. Moll, R. Huber, and J. Repp, *Sub-cycle atomic-scale forces coherently control a single-molecule switch*, Nature **585**, 58–62 (2020).

[Pel21] D. Peller, C. Roelcke, L. Z. Kastner, T. Buchner, A. Neef, J. Hayes, F. Bonafé, D. Sidler, M. Ruggenthaler, A. Rubio, R. Huber, and J. Repp, *Quantitative sampling of atomic-scale electromagnetic waveforms*, Nature Photonics **15**, 143–147 (2021).

[Pen21] J. Peng, S. Sokolov, D. Hernangómez-Pérez, F. Evers, L. Gross, J. M. Lupton, and J. Repp, *Atomically resolved single-molecule triplet quenching*, Science **373**, 452–456 (2021).

[Pie06] O. Pietzsch, S. Okatov, A. Kubetzka, M. Bode, S. Heinze, A. Lichtenstein, and R. Wiesendanger, *Spin-Resolved Electronic Structure of Nanoscale Cobalt Islands on Cu(111)*, Physical Review Letters **96**, 237203 (2006).

[Pig13] B. Piglosiewicz, S. Schmidt, D. J. Park, J. Vogelsang, P. Groß, C. Manzoni, P. Farinello, G. Cerullo, and C. Lienau, *Carrier-envelope phase effects on the strong-field photoemission of electrons from metallic nanostructures*, Nature Photonics **8**, 37–42 (2013).

[Pla21] M. Plankl, P. E. Faria Junior, F. Mooshammer, T. Siday, M. Zizlsperger, F. Sandner, F. Schiegl, S. Maier, M. A. Huber, M. Gmitra, J. Fabian, J. L. Boland, T. L. Cocker, and R. Huber, *Subcycle contact-free nanoscopy of ultrafast interlayer transport in atomically thin heterostructures*, Nature Photonics **15**, 594–600 (2021).

[Poe15] C. Poellmann, P. Steinleitner, U. Leierseder, P. Nagler, G. Plechinger, M. Porer, R. Bratschitsch, C. Schüller, T. Korn, and R. Huber, *Resonant internal quantum transitions and femtosecond radiative decay of excitons in monolayer* WSe_2, Nature Materials **14**, 889–893 (2015).

[Qiu04] X. H. Qiu, G. V. Nazin, and W. Ho, *Mechanisms of Reversible Conformational Transitions in a Single Molecule*, Physical Review Letters **93**, 196806 (2004).

[Qiu12] H. Qiu, L. Pan, Z. Yao, J. Li, Y. Shi, and X. Wang, *Electrical characterization of back-gated bi-layer MoS_2 field-effect transistors and the effect of ambient on their performances*, Applied Physics Letters **100** (2012).

[RA18] S. Refaely-Abramson, D. Y. Qiu, S. G. Louie, and J. B. Neaton, *Defect-Induced Modification of Low-Lying Excitons and Valley Selectivity in Monolayer Transition Metal Dichalcogenides*, Physical Review Letters **121**, 167402 (2018).

[RD21] A. Rossius-Dausgaard, *The inner light*, Retrieved October 20, 2024 from https://linguaanimarum.com/2021/10/05/the-inner-light/.

[Rei18] J. Reimann, S. Schlauderer, C. P. Schmid, F. Langer, S. Baierl, K. A. Kokh, O. E. Tereshchenko, A. Kimura, C. Lange, J. Güdde, U. Höfer, and R. Huber, *Subcycle observation of lightwave-driven Dirac currents in a topological surface band*, Nature **562**, 396–400 (2018).

[Rep05a] J. Repp, G. Meyer, S. Paavilainen, F. E. Olsson, and M. Persson, *Scanning Tunneling Spectroscopy of Cl Vacancies in NaCl Films: Strong Electron-Phonon Coupling in Double-Barrier Tunneling Junctions*, Physical Review Letters **95**, 225503 (2005).

[Rep05b] J. Repp, G. Meyer, S. M. Stojković, A. Gourdon, and C. Joachim, *Molecules on Insulating Films: Scanning-Tunneling Microscopy Imaging of Individual Molecular Orbitals*, Physical Review Letters **94**, 026803 (2005).

[Rep10] J. Repp and G. Meyer, *Scanning Tunneling Spectroscopy of Molecules on Insulating Films*, CHIMIA **64**, 370 (2010).

[Roe24] C. Roelcke, L. Z. Kastner, M. Graml, A. Biereder, J. Wilhelm, J. Repp, R. Huber, and Y. A. Gerasimenko, *Ultrafast atomic-scale scanning tun-*

nelling spectroscopy of a single vacancy in a monolayer crystal, Nature Photonics (2024).

[Rom13] N. Romming, C. Hanneken, M. Menzel, J. E. Bickel, B. Wolter, K. von Bergmann, A. Kubetzka, and R. Wiesendanger, *Writing and Deleting Single Magnetic Skyrmions*, Science **341**, 636–639 (2013).

[Rop07] C. Ropers, D. R. Solli, C. P. Schulz, C. Lienau, and T. Elsaesser, *Localized Multiphoton Emission of Femtosecond Electron Pulses from Metal Nanotips*, Physical Review Letters **98**, 043907 (2007).

[Rus05] S. Rusponi, N. Weiss, T. Cren, M. Epple, and H. Brune, *High tunnel magnetoresistance in spin-polarized scanning tunneling microscopy of Co nanoparticles on Pt(111)*, Applied Physics Letters **87** (2005).

[Sai05] Y. Sainoo, Y. Kim, T. Okawa, T. Komeda, H. Shigekawa, and M. Kawai, *Excitation of Molecular Vibrational Modes with Inelastic Scanning Tunneling Microscopy Processes: Examination through Action Spectra ofcis-2-Butene on Pd(110)*, Physical Review Letters **95**, 246102 (2005).

[Sar21] S. Sarkar and P. Kratzer, *Signatures of the Dichalcogenide–Gold Interaction in the Vibrational Spectra of MoS_2 and $MoSe_2$ on Au(111)*, The Journal of Physical Chemistry C **125**, 26645–26651 (2021).

[Sch91] R. W. Schoenlein, L. A. Peteanu, R. A. Mathies, and C. V. Shank, *The First Step in Vision: Femtosecond Isomerization of Rhodopsin*, Science **254**, 412–415 (1991).

[Sch97] A. Scholl, L. Baumgarten, R. Jacquemin, and W. Eberhardt, *Ultrafast Spin Dynamics of Ferromagnetic Thin Films Observed by fs Spin-Resolved Two-Photon Photoemission*, Physical Review Letters **79**, 5146–5149 (1997).

[Sch10a] M. Schenk, M. Krüger, and P. Hommelhoff, *Strong-Field Above-Threshold Photoemission from Sharp Metal Tips*, Physical Review Letters **105**, 257601 (2010).

[Sch10b] J. A. Schuller, E. S. Barnard, W. Cai, Y. C. Jun, J. S. White, and M. L. Brongersma, *Plasmonics for extreme light concentration and manipulation*, Nature Materials **9**, 193–204 (2010).

[Sch13] J. Schaffert, M. C. Cottin, A. Sonntag, H. Karacuban, D. Utzat, C. A. Bobisch, and R. Möller, *Scanning noise microscopy*, Review of Scientific Instruments **84** (2013).

[Sch19] B. Schuler, D. Y. Qiu, S. Refaely-Abramson, C. Kastl, C. T. Chen, S. Barja, R. J. Koch, D. F. Ogletree, S. Aloni, A. M. Schwartzberg, J. B. Neaton, S. G. Louie, and A. Weber-Bargioni, *Large Spin-Orbit Splitting of Deep In-Gap Defect States of Engineered Sulfur Vacancies in Monolayer WS_2*, Physical Review Letters **123**, 076801 (2019).

[Sch22] D. Schmitt, J. P. Bange, W. Bennecke, A. AlMutairi, G. Meneghini, K. Watanabe, T. Taniguchi, D. Steil, D. R. Luke, R. T. Weitz, S. Steil, G. S. M. Jansen, S. Brem, E. Malic, S. Hofmann, M. Reutzel, and S. Mathias, *Formation of moiré interlayer excitons in space and time*, Nature **608**, 499–503 (2022).

[Sel23] L. Sellies, R. Spachtholz, S. Bleher, J. Eckrich, P. Scheuerer, and J. Repp, *Single-molecule electron spin resonance by means of atomic force microscopy*, Nature **624**, 64–68 (2023).

[She22] S. Sheng, A.-C. Oeter, M. Abdo, K. Lichtenberg, M. Hentschel, and S. Loth, *Launching Coherent Acoustic Phonon Wave Packets with Local Femtosecond Coulomb Forces*, Physical Review Letters **129**, 043001 (2022).

[She24] S. Sheng, M. Abdo, S. Rolf-Pissarczyk, K. Lichtenberg, S. Baumann, J. A. J. Burgess, L. Malavolti, and S. Loth, *Terahertz spectroscopy of collective charge density wave dynamics at the atomic scale*, Nature Physics (2024).

[Sid24] T. Siday, J. Hayes, F. Schiegl, F. Sandner, P. Menden, V. Bergbauer, M. Zizlsperger, S. Nerreter, S. Lingl, J. Repp, J. Wilhelm, M. A. Huber, Y. A. Gerasimenko, and R. Huber, *All-optical subcycle microscopy on atomic length scales*, Nature **629**, 329–334 (2024).

[Sie15] B. Siegert, A. Donarini, and M. Grifoni, *Effects of spin–orbit coupling and many-body correlations in STM transport through copper phthalocyanine*, Beilstein Journal of Nanotechnology **6**, 2452–2462 (2015).

[Sri15] A. Srivastava, M. Sidler, A. V. Allain, D. S. Lembke, A. Kis, and A. Imamoğlu, *Optically active quantum dots in monolayer WSe_2*, Nature Nanotechnology **10**, 491–496 (2015).

[Sti98] B. C. Stipe, M. A. Rezaei, and W. Ho, *Coupling of Vibrational Excitation to the Rotational Motion of a Single Adsorbed Molecule*, Physical Review Letters **81**, 1263–1266 (1998).

[Sto16] R. Stockill, C. Le Gall, C. Matthiesen, L. Huthmacher, E. Clarke, M. Hugues, and M. Atatüre, *Quantum dot spin coherence governed by a strained nuclear environment*, Nature Communications **7** (2016).

[Str86] J. A. Stroscio, R. M. Feenstra, and A. P. Fein, *Electronic Structure of the Si(111)2 $\times$ 1 Surface by Scanning-Tunneling Microscopy*, Physical Review Letters **57**, 2579–2582 (1986).

[Str87] J. A. Stroscio, R. M. Feenstra, and A. P. Fein, *Imaging electronic surface states in real space on the Si(111)2$\times$1 surface*, Journal of Vacuum Science & Technology A: Vacuum, Surfaces, and Films **5**, 838–841 (1987).

[Sø14] S. G. Sørensen, H. G. Füchtbauer, A. K. Tuxen, A. S. Walton, and J. V. Lauritsen, *Structure and Electronic Properties of In Situ Synthesized Single-Layer MoS_2 on a Gold Surface*, ACS Nano **8**, 6788–6796 (2014).

[Ter83] J. Tersoff and D. R. Hamann, *Theory and Application for the Scanning Tunneling Microscope*, Physical Review Letters **50**, 1998–2001 (1983).

[Ter85] J. Tersoff and D. R. Hamann, *Theory of the scanning tunneling microscope*, Physical Review B **31**, 805–813 (1985).

[Ter10] Y. Terada, S. Yoshida, O. Takeuchi, and H. Shigekawa, *Real-space imaging of transient carrier dynamics by nanoscale pump–probe microscopy*, Nature Photonics **4**, 869–874 (2010).

[Ton13] S. Tongay, J. Suh, C. Ataca, W. Fan, A. Luce, J. S. Kang, J. Liu, C. Ko, R. Raghunathanan, J. Zhou, F. Ogletree, J. Li, J. C. Grossman, and J. Wu, *Defects activated photoluminescence in two-dimensional semiconductors: interplay between bound, charged and free excitons*, Scientific Reports **3** (2013).

[Ton15] P. Tonndorf, R. Schmidt, R. Schneider, J. Kern, M. Buscema, G. A. Steele, A. Castellanos-Gomez, H. S. J. van der Zant, S. Michaelis de Vasconcellos, and R. Bratschitsch, *Single-photon emission from localized excitons in an atomically thin semiconductor*, Optica **2**, 347 (2015).

[Vel18] M. Velický, G. E. Donnelly, W. R. Hendren, S. McFarland, D. Scullion, W. J. I. DeBenedetti, G. C. Correa, Y. Han, A. J. Wain, M. A. Hines, D. A. Muller, K. S. Novoselov, H. D. Abruña, R. M. Bowman, E. J. G. Santos, and F. Huang, *Mechanism of Gold-Assisted Exfoliation of Centimeter-Sized Transition-Metal Dichalcogenide Monolayers*, ACS Nano **12**, 10463–10472 (2018).

[Wal21a] R. Wallauer, M. Raths, K. Stallberg, L. Münster, D. Brandstetter, X. Yang, J. Güdde, P. Puschnig, S. Soubatch, C. Kumpf, F. C. Bocquet, F. S. Tautz, and U. Höfer, *Tracing orbital images on ultrafast time scales*, Science **371**, 1056–1059 (2021).

[Wal21b] R. Wallauer, R. Perea-Causin, L. Münster, S. Zajusch, S. Brem, J. Güdde, K. Tanimura, K.-Q. Lin, R. Huber, E. Malic, and U. Höfer, *Momentum-Resolved Observation of Exciton Formation Dynamics in Monolayer* WS_2, Nano Letters **21**, 5867–5873 (2021).

[Wan18] G. Wang, A. Chernikov, M. M. Glazov, T. F. Heinz, X. Marie, T. Amand, and B. Urbaszek, *Colloquium: Excitons in atomically thin transition metal dichalcogenides*, Reviews of Modern Physics **90**, 021001 (2018).

[Wan22] L. Wang, Y. Xia, and W. Ho, *Atomic-scale quantum sensing based on the ultrafast coherence of an* H_2 *molecule in an STM cavity*, Science **376**, 401–405 (2022).

[Wei93] S. Weiss, D. F. Ogletree, D. Botkin, M. Salmeron, and D. S. Chemla, *Ultrafast scanning probe microscopy*, Applied Physics Letters **63**, 2567–2569 (1993).

[Wie09] R. Wiesendanger, *Spin mapping at the nanoscale and atomic scale*, Reviews of Modern Physics **81**, 1495–1550 (2009).

[Wim14] L. Wimmer, G. Herink, D. R. Solli, S. V. Yalunin, K. E. Echternkamp, and C. Ropers, *Terahertz control of nanotip photoemission*, Nature Physics **10**, 432–436 (2014).

[Wol21] G. Wolfowicz, F. J. Heremans, C. P. Anderson, S. Kanai, H. Seo, A. Gali, G. Galli, and D. D. Awschalom, *Quantum guidelines for solid-state spin defects*, Nature Reviews Materials **6**, 906–925 (2021).

[Xu14] X. Xu, W. Yao, D. Xiao, and T. F. Heinz, *Spin and pseudospins in layered transition metal dichalcogenides*, Nature Physics **10**, 343–350 (2014).

[Xu20] Y. Xu, S. Liu, D. A. Rhodes, K. Watanabe, T. Taniguchi, J. Hone, V. Elser, K. F. Mak, and J. Shan, *Correlated insulating states at fractional fillings of moiré superlattices*, Nature **587**, 214–218 (2020).

[Xu21] J. Xu, X. Zhu, S. Tan, Y. Zhang, B. Li, Y. Tian, H. Shan, X. Cui, A. Zhao, Z. Dong, J. Yang, Y. Luo, B. Wang, and J. G. Hou, *Determining structural and chemical heterogeneities of surface species at the single-bond limit*, Science **371**, 818–822 (2021).

[Yan20] B. Yang, G. Chen, A. Ghafoor, Y. Zhang, Y. Zhang, Y. Zhang, Y. Luo, J. Yang, V. Sandoghdar, J. Aizpurua, Z. Dong, and J. G. Hou, *Subnanometre resolution in single-molecule photoluminescence imaging*, Nature Photonics **14**, 693–699 (2020).

[Yos19] S. Yoshida, H. Hirori, T. Tachizaki, K. Yoshioka, Y. Arashida, Z.-H. Wang, Y. Sanari, O. Takeuchi, Y. Kanemitsu, and H. Shigekawa, *Subcycle Transient Scanning Tunneling Spectroscopy with Visualization of Enhanced Terahertz Near Field*, ACS Photonics **6**, 1356–1364 (2019).

[Yos21] S. Yoshida, Y. Arashida, H. Hirori, T. Tachizaki, A. Taninaka, H. Ueno, O. Takeuchi, and H. Shigekawa, *Terahertz Scanning Tunneling Microscopy for Visualizing Ultrafast Electron Motion in Nanoscale Potential Variations*, ACS Photonics **8**, 315–323 (2021).

[Zak12] B. Zaks, R. B. Liu, and M. S. Sherwin, *Experimental observation of electron–hole recollisions*, Nature **483**, 580–583 (2012).

[Zha15] C. Zhang, Y. Chen, A. Johnson, M.-Y. Li, L.-J. Li, P. C. Mende, R. M. Feenstra, and C.-K. Shih, *Probing Critical Point Energies of Transition Metal Dichalcogenides: Surprising Indirect Gap of Single Layer* WSe_2, Nano Letters **15**, 6494–6500 (2015).

[Zha16] Y. Zhang, H. Kersell, R. Stefak, J. Echeverria, V. Iancu, U. G. E. Perera, Y. Li, A. Deshpande, K.-F. Braun, C. Joachim, G. Rapenne, and S.-W. Hla, *Simultaneous and coordinated rotational switching of all molecular rotors in a network*, Nature Nanotechnology **11**, 706–712 (2016).

[Zho15] Y. Zhou, E. Iacocca, A. A. Awad, R. K. Dumas, F. C. Zhang, H. B. Braun, and J. Åkerman, *Dynamically stabilized magnetic skyrmions*, Nature Communications **6** (2015).

[Zho21] Y. Zhou, J. Sung, E. Brutschea, I. Esterlis, Y. Wang, G. Scuri, R. J. Gelly, H. Heo, T. Taniguchi, K. Watanabe, G. Zaránd, M. D. Lukin, P. Kim, E. Demler, and H. Park, *Bilayer Wigner crystals in a transition metal dichalcogenide heterostructure*, Nature **595**, 48–52 (2021).

Acknowledgments

I would like to thank several people without whom my dissertation, this chapter of my life, would not have been nearly as enjoyable or even possible. Thanks to many amazing personalities, these last years were inspiring, instructive and simply fun. The next few pages are not enough to capture all the wonderful moments I was fortunate enough to experience.

One cannot wish for a better dream team of mentors than **Rupert Huber** and **Jascha Repp**. I would like to express my deep gratitude for their constant support both in ultrafast optics and scanning tunneling microscopy, for spontaneous office discussions and comprehensive explanations of complex physics as well as an open ear for personal concerns. It is pure luxury to be supervised by these two profound experts in different fields. The fruitful collaboration and peaceful exchange they share on a daily basis is exceptional and I have profited a lot from that. Not only scientifically, but also personally, I was able to grow within these years – due to the team work enabled by the two of you, but also numerous inspiring experiences like conference trips, which I benefit from way beyond science. Thank you for your trust in me and your unwavering support!

Moreover, I would like to cordially thank the board of examiners formed by **Prof. Dr. Jaroslav Fabian**, **Prof. Dr. Rupert Huber**, **Prof. Dr. Jascha Repp** and **Prof. Dr. Jörg Wunderlich**. Many thanks for taking the time to assess my work and to conduct my oral examination.

I could not have imagined a better lab companion than **Lukas Kastner**. Most of the work presented is our common achievement and I highly appreciate our wonderful teamwork. Of course, I am very grateful for sharing the work load like night shifts, but in particular, I highly value the mutual trust and honesty we have been enjoying over all these common years.

Yaroslav Gerasimenko has been a driving force behind sample fabrication with tireless dedication. Moreover, his physics explanations as well as numerous stories, in the office and during coffee breaks, have been highly inspiring. Last but not least, he has been a contact point for lab issues and data discussions on a daily basis, which has been truly indispensable.

Dominik Peller was able to form a wonderful spirit in the lab for truly enjoyable team efforts for the common achievements presented in this thesis. Besides sharing our needs for coffee, we often spent hours philosophizing. I would like to thank him for this beautiful time together and for occasional confidence boosts to pursue my goals.

I would like to thank both **Maximilian Graml** and **Jan Wilhelm**, whom it was a pleasure to work with on a personal and scientific level.
Moreover, I would like to thank **Florian Albrecht** for all the STM-related guidance and for many fun hours in the lab.
Also, I would like to express my gratitude towards **Thomas Buchner** and **Alexander Neef**, both former fellow students, which I was lucky enough to meet again in the lab. I would like to thank them for the fruitful work and the enjoyable moments we have been sharing.
Johannes Hayes has not only been fun to work with, but I have been enjoying a lot the mutual support and common experiences inside and outside the university shaping a healthy environment and simply beautiful memories.
Moreover, I would like to express my gratitude to **Andreas Biereder** for the pleasant work together.

Besides all the colleagues, whom I shared the presented publications with, I would like to thank everyone, who joined for smaller projects. I was lucky enough to work with **Sarah Philips**, **Marc Aichner**, **Carolyn Echter** and **Jennifer Lehner** on different aspects concerning sample preparation, steady-state STM measurements and early stages of experiments. I am grateful to every single one of them for the common learning experience.
Moreover, I recently started working with **Niklas Friedrich** as well as **Tzu-Chao Hung**, whom I would like to thank cordially for the very enjoyable working atmosphere and for their valuable insights.

Probably not one PhD student would get through this phase of life nearly as smoothly without **Ulla Franzke**. I would like to thank her for her continuous support. Whatever lands on her table or in her room, she takes care of in an act of balancing all the different interests every day – because she cares about the people around her.

In addition, the support by the permanent technical staff in the two groups has been priceless, eliminating every possible technical challenge. **Imke Gronwald**, **Martin Furthmeier**, **Christoph Rohrer**, **Ignaz Laepple**, **Andreas Pöllmann** and **Matthias Heinl** have played an essential role in enabling the research presented. Thank you all for your permanent support!
Imke Gronwald's input was invaluable concerning gold evaporation on mica and sample preparation in the chemistry lab. Whenever there is a challenge, she's on fire – no matter whether for sample fabrication, finding out more about PDMS residues or spending time on SEM measurements of tips, her positive attitude and professional input has been extremely helpful and inspiring.
Martin Furthmeier always finds a solution for a problem. He has designed countless components, housings, flippable mounts – whatever your brain can fantasize – without none of the experiments in this thesis would have been possible.
Besides providing technical input concerning the lightwave-driven SP-STM and CAD drawings for this thesis, **Christoph Rohrer** also managed all sorts of technical issues in the lab essential for everyday work. Also, **Andreas Pöllmann** contributed a lot in the early stages of the spin-polarized LW-STM. Moreover, he strongly supported me during machine repairs back in the years.

Moreover, I would like to thank **Lukas Kastner**, **Yaroslav Gerasimenko**, **Tzu-Chao Hung**, **Niklas Friedrich** and **Simon Maier** for their valuable feedback on my thesis.

On a personal note, I would like to thank the **Spätsünder** crew for the daily fun experience, relaxing atmosphere, walks and good conversations.
Christian Meineke has been a wonderful colleague, lab mate and office companion. But besides that, we spent so many soothing and cheerful hours in conversations and various leisure activities. Thank you for sharing these fun times!
Markus Plankl and **Markus Huber** made me an addict to Beate's classes, thank you for taking me along to these hours of suffering and the subsequent gluttony. Also, I would like to thank Markus Huber for his beautiful renders finished within a single blink!
Besides the comforting exchange every day and numerous adventures outside the lab, I would like to thank **Josef Freudenstein** and **Martin Zizlsperger** for the beautiful days we spent together on the last meters of my PhD, I had a truly wonderful time with you forming lasting memories.
Also, I would like to thank **Sonja Lingl** for being the good soul of the office making sure the amount of sugar in everyone's blood stays at a high level.
Moreover, I will not forget all the fun hours I spent with **Svenja Nerreter**, **Marlene Liebich**, **Manuel Meierhofer**, **Niloufar Nilforoushan**, **Katharina Glöckl**, **Raffael Spachtholz**, **Simon Anglhuber**, **Tom Siday**, **Dima Afasaniev** and all the other former and recent members of the two working groups, many of whom have become close friends of mine – what a bunch of caring, brilliant people, thank you!

I simply don't know where to start when thanking **Simon Maier**. Of course, much more connects us than the common PhD time. However, all the beautiful moments together have made this time so precious and also, some periods throughout these years would not have been possible without his constant support, sympathy and counterbalancing. He has my deepest gratitude.
Finally, I would like to express my gratitude to **my siblings**, **my parents** and **my friends** for their unshakable support.